
VNIVERSITAT DE VALÈNCIA

# Identification of Loss Factors in Co-Evaporated Perovskite Solar Cells

– PhD Thesis –

**Chris Lennart Dreessen**

PhD program in Nanoscience and Nanotechnology

**Directors:**

Prof. Dr. Hendrik Jan Bolink

Dr. Cristina Roldan Carmona

**January 2025**

VNIVERSITAT DE VALÈNCIA

**Prof. Dr. Hendrik Jan Bolink** y **Dr. Cristina Roldan Carmona**, catedrático e investigadora Ramón y Cajal de la Universitat de Valéncia en el Instituto de Ciencia Molecular (ICMol), certifican que la memoria presentada por el estudiante de doctorado Chris Lennart Dreessen, con el titulo "*Identification of Loss Factors in Co-Evaporated Perovskite Solar Cells*", corresponde a su Tesis Doctoral y ha sido realizada bajo su dirección y tutoría, autorizando mediante este escrito la presentación de la misma.

A Paterna (València), a 13 de Enero de 2025.

Prof. Dr. Hendrik Jan Bolink

(director y tutor)

Dr. Cristina Roldan Carmona

(directora)

# Abstract

Perovskite solar cells have emerged as a promising photovoltaic technology with high power conversion efficiencies, yet most research focuses on lab-scale solutions-processed fabrication techniques. Co-evaporation offers a high control over film thicknesses and stoichiometry as well as the potential of up-scaling. However, co-evaporated perovskite solar cells remain comparatively underexplored, particularly with respect to fundamental loss mechanisms. This thesis aims to address this gap by systematically identifying and analyzing the factors that constrain the performance of co-evaporated perovskite solar cells.

A detailed evaluation of efficiency losses in various co-evaporated solar cells reveals that short-circuit current density, open-circuit voltage, and fill factor contribute equally to overall performance limitations, indicating the need for a thorough analysis of each. Through sensitive photovoltaic quantum efficiency measurements, the optically active states in the bandgap are shown to cause negligible radiative voltage losses with the consequence that the voltage behavior is dominated by non-radiative recombination, which results independent of structural disorder as indicated by the Urbach energy. Additionally, the observed correlation between current density and fill factor points to electrical losses beyond the classical models of constant resistances.

To probe recombination during charge extraction, voltage-dependent photoluminescence is discussed as a diagnostic tool. A high quasi-Fermi level splitting under all bias conditions reveals incomplete charge extraction as a key bottleneck and points to the necessity of optimizing device configurations to reduce recombination and transport losses. The calculated idealized current-voltage curves assuming perfect transport inside the solar cell show significant short-circuit current and fill factor improvements of 5-9% and 9-18% relative to their Shockley-Queisser limit, respectively. Moreover, the photoluminescence quantum yield under varying biases suggests the presence of complex recombination pathways extending past simple deep or shallow defects.

Furthermore, the source of non-radiative recombination inside the solar cell is investigated. The bulk limit of the open-circuit voltage is determined using photoluminescence measurements of freestanding films, where the influence of surface recombination in the freestanding film sample is excluded through passivation strategies and the analysis of transient photoluminescence of films with varying thicknesses. The resulting bulk limit is only marginally higher than the measured open-circuit voltage of the device. A drift-diffusion model, established via light-intensity-dependent photoluminescence measurements and current-voltage curves, reveals that bulk and interface recombination impose comparable constraints on the open-circuit voltage. This dual limitation complicates optimization efforts, as isolated bulk or interface improvements result in only minor performance gains. The findings emphasize the critical need for a characterization approach combining photoluminescence and electrical measurements to uncover and address hidden loss mechanisms systematically. This is exemplified experimentally by the introduction of small amounts of methylammonium chloride during the evaporation process, which significantly increases the photoluminescence quantum yield for freestanding films yet show only modest improvements in the open-circuit voltage of devices.

In conclusion, co-evaporated perovskite solar cells face a challenge in optimization strategy due to the absence of a single dominant loss mechanism. Instead, the performance is constrained by a complex interplay of optical, transport, and recombination losses. This multifaceted nature limits the impact of isolated improvements, necessitating a holistic and systematic approach to device optimization. The methodologies and insights presented in this thesis provide a framework for addressing these challenges and advancing the efficiency of co-evaporated perovskite solar cells toward their theoretical potential.

# Resumen

Las células solares de perovskita han surgido como una tecnología fotovoltaica prometedora con altas eficiencias de conversión de energía, aunque la mayoría de las investigaciones se centran en técnicas de fabricación a escala de laboratorio mediante procesos en solución. La co-evaporación ofrece un alto control sobre el grosor de las películas y la estequiometría, así como el potencial para su escalado. Sin embargo, las células solares de perovskita co-evaporadas siguen estando relativamente poco exploradas, especialmente en lo que respecta a los mecanismos fundamentales de pérdida. Esta tesis tiene como objetivo abordar esta brecha identificando y analizando sistemáticamente los factores que limitan el rendimiento de las células solares de perovskita co-evaporadas.

La evaluación detallada de las pérdidas de eficiencia en diversas células solares co-evaporadas revela que la densidad de corriente de cortocircuito, el voltaje de circuito abierto y el factor de llenado contribuyen en igual medida a las limitaciones de rendimiento general, lo que lleva a la necesidad de realizar un análisis exhaustivo de cada parámetro. A través de mediciones sensibles de eficiencia cuántica fotovoltaica, se demuestra que los estados ópticamente activos en la banda prohibida causan insignificantes pérdidas radiativas de voltaje, lo que implica que el comportamiento de este parámetro está dominado por la recombinación no radiativa, independiente del desorden estructural, como lo indica la energía de Urbach. Además, la correlación observada entre la densidad de corriente y el factor de llenado apunta a pérdidas eléctricas más allá de los modelos clásicos de resistencias constantes.

Para investigar la recombinación durante la extracción de carga, se discute la fotoluminiscencia dependiente del voltaje como una herramienta de diagnóstico. La alta separación de niveles quasi-Fermi bajo todas las condiciones de polarización revela que la extracción de carga incompleta es un factor limitante clave, y destaca la necesidad de optimizar las configuraciones de los dispositivos para reducir las pérdidas de recombinación y transporte. Las curvas corriente-voltaje idealizadas, calculadas asumiendo un transporte

perfecto dentro de la célula solar, muestran mejoras significativas en la corriente de cortocircuito y el factor de llenado, del 5-9% y del 9-18% en relación con su límite de Shockley-Queisser, respectivamente. Además, el rendimiento cuántico de fotoluminiscencia bajo diferentes polarizaciones sugiere la presencia de vías de recombinación complejas que van más allá de los defectos simples profundos o superficiales.

Asimismo, se investiga la fuente de recombinación no radiativa dentro de la célula solar. El límite de voltaje de circuito abierto en el material se determina mediante mediciones de fotoluminiscencia de películas independientes, donde la influencia de la recombinación superficial en las muestras se excluye recurriendo a estrategias de pasivación, y al análisis de fotoluminiscencia transitoria de películas con diferentes grosores. El límite del material resultante es solo marginalmente más alto que el voltaje de circuito abierto medido en el dispositivo. Un modelo de deriva-difusión, establecido mediante mediciones de fotoluminiscencia dependiente de la intensidad lumínica y curvas corriente-voltaje, revela que la recombinación en el material y en las interfaces imponen restricciones comparables sobre el voltaje de circuito abierto. Esta limitación dual complica los esfuerzos de optimización, ya que mejoras aisladas en el material o en las interfaces resultan en ganancias de rendimiento menores. Los hallazgos subrayan la necesidad crítica de un enfoque de caracterización que combine mediciones de fotoluminiscencia y eléctricas, que permita descubrir y abordar sistemáticamente los mecanismos de pérdida ocultos. Esto se ejemplifica experimentalmente mediante la introducción de pequeñas cantidades de cloruro de metilamonio durante el proceso de evaporación, lo que aumenta significativamente el rendimiento cuántico de fotoluminiscencia para películas independientes, manteniendo mejoras muy modestas en el voltaje de circuito abierto de los dispositivos.

En conclusión, las células solares de perovskita co-evaporadas enfrentan un desafío en la estrategia de optimización debido a la ausencia de un único mecanismo de pérdida dominante. En su lugar, el rendimiento está limitado por una interacción compleja de pérdidas ópticas, de transporte y de recombinación. Esta naturaleza multifacética limita el impacto de las mejoras aisladas, requiriendo un enfoque holístico y sistemático para la optimización de dispositivos. Las metodologías e ideas presentadas en esta tesis proporcionan un marco para abordar estos desafíos y avanzar en la eficiencia de las células solares de perovskita co-evaporadas hacia su potencial teórico.

# Resum

Les cèl·lules solars de perovskita han sorgit com una tecnologia fotovoltaica prometedora amb altes eficiències de conversió energètica, encara que la major part de les investigacions es concentren en tècniques de fabricació a escala de laboratori mitjançant processos en solució. La co-evaporació ofereix un alt control sobre el gruix de les capes i l'estequiometria, així com el potencial per a la seua escalabilitat. No obstant això, les cèl·lules solars de perovskita co-evaporades continuen estant relativament poc explorades, especialment en allò referit als mecanismes fonamentals de pèrdua. Aquesta tesi pretén abordar aquesta bretxa identificant i analitzant sistemàticament els factors que limiten el rendiment de les cèl·lules solars de perovskita co-evaporades.

Una avaluació detallada de les pèrdues d'eficiència en diverses cèl·lules solars co-evaporades revela que la densitat de corrent de curtcircuit, el voltatge de circuit obert i el factor d'ompliment contribueixen per igual a les limitacions generals de rendiment, cosa que indica la necessitat d'una anàlisi exhaustiva de cadascun d'ells. Mitjançant mesures sensibles d'eficiència quàntica fotovoltaica, es demostra que els estats òpticament actius en la banda prohibida provoquen pèrdues radiatives de voltatge insignificants, cosa que implica que el comportament del voltatge està dominat per la recombinació no radiativa, independent del desordre estructural, tal com indica l'energia d'Urbach. A més, la correlació observada entre la densitat de corrent i el factor d'ompliment apunta a pèrdues elèctriques que van més enllà dels models clàssics de resistències constants.

Per a investigar la recombinació durant l'extracció de càrrega, es discuteix la fotoluminescència dependent del voltatge com a eina de diagnòstic. Una alta separació de nivells quasi-Fermi sota totes les condicions de polarització revela que l'extracció incompleta de càrrega és un coll d'ampolla clau i posa de manifest la necessitat d'optimitzar les configuracions dels dispositius per a reduir les pèrdues de recombinació i transport. Les corbes corrent-voltatge idealitzades calculades, assumint un transport perfecte dins de la cèl·lula solar, mostren millores significatives en el corrent de curtcircuit i el factor

d'ompliment del 5-9% i del 9-18% en relació amb el seu límit de Shockley-Queisser, respectivament. A més, el rendiment quàntic de fotoluminescència sota diferents polaritzacions suggereix la presència de vies complexes de recombinació que van més enllà dels defectes simples profunds o superficials.

A més, s'investiga l'origen de la recombinació no radiativa dins de la cèl·lula solar. El límit de voltatge de circuit obert en el material es determina mitjançant mesures de fotoluminescència de capes independents, on la influència de la recombinació superficial en les mostres es descarta mitjançant estratègies de passivació i l'anàlisi de la fotoluminescència transitòria de capes amb diferents grossors. El límit del material resultant és només marginalment més alt que el voltatge de circuit obert mesurat al dispositiu. Un model de deriva-difusió, establit mitjançant mesures de fotoluminescència dependent de la intensitat de la llum i corbes corrent-volt, revela que la recombinació al material i a les interfícies imposen restriccions comparables sobre el voltatge de circuit obert. Aquesta limitació dual complica els esforços d'optimització, ja que millores aïllades al material o a les interfícies resulten en guanys de rendiment menors. Els resultats subratllen la necessitat crítica d'un enfocament de caracterització que combine mesures de fotoluminescència i elèctriques per a descobrir i abordar sistemàticament els mecanismes de pèrdua ocults. Això s'exemplifica experimentalment mitjançant la introducció de petites quantitats de clorur de metilamoni durant el procés d'evaporació, cosa que augmenta significativament el rendiment quàntic de fotoluminescència per a capes independents, però mostra només millores modestes en el voltatge de circuit obert dels dispositius.

En conclusió, les cèl·lules solars de perovskita co-evaporades s'enfronten a un desafiament en l'estratègia d'optimització a causa de l'absència d'un únic mecanisme de pèrdua dominant. En lloc d'això, el rendiment està limitat per una interacció complexa de pèrdues òptiques, de transport i de recombinació. Aquesta naturalesa multifacètica limita l'impacte de les millores aïllades, requerint un enfocament holístic i sistemàtic per a l'optimització dels dispositius. Les metodologies i idees presentades en aquesta tesi proporcionen un marc per a abordar aquests desafiaments i avançar en l'eficiència de les cèl·lules solars de perovskita co-evaporades cap al seu potencial teòric.

# Contents

# 1 Introduction

In this chapter, the motivation for the choice of the topics of this thesis is given. Simple concepts are introduced that are necessary to understand the presented work. There are many great textbooks to which the interested reader is referred to for a more detailed description of the physics of solar cells.[1–4]

## 1.1 Need for photovoltaic technologies and perovskite solar cells

Climate change, a phenomenon largely caused by elevated levels of carbon dioxide emissions, has been a topic of concern for humanity for several decades. Despite early warnings and detailed knowledge of players who could have made a change, the necessary actions to mitigate the impact of climate change have been missing or even impeded by said players for a long time.[5,6] The main obstacle to significant progress in this area has been the lack of financial motivation for individuals and corporations to transition to more sustainable energy sources. At the same time the global energy needs are still rising and this mostly leads to an accompanying increase in $CO_2$ emissions (Figure 1.1a and b).[7] Only in recent years with the rise of renewable energies, the emissions decoupled slightly from the energy production.

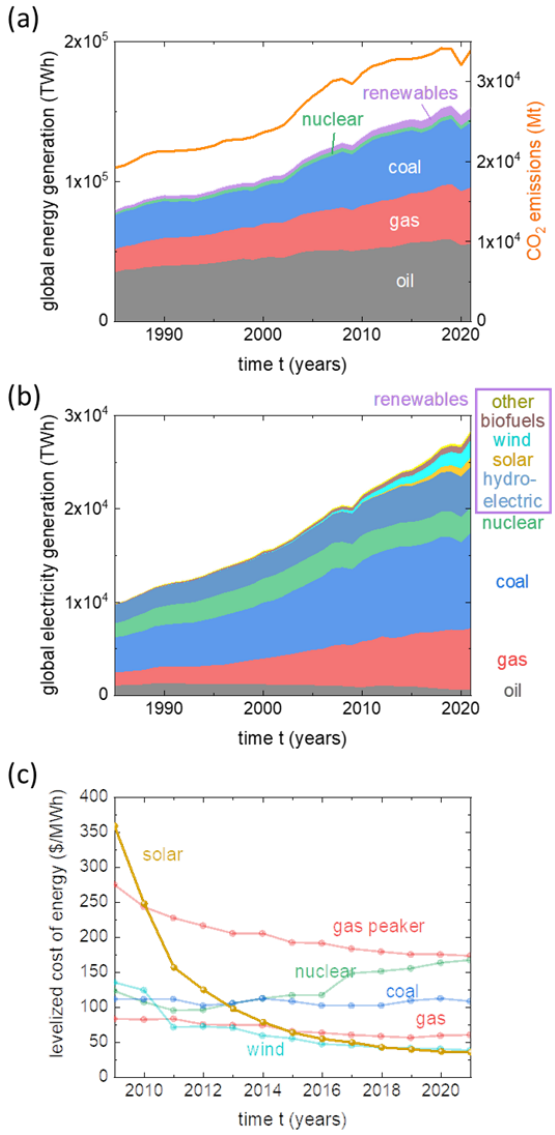


Figure 1.1 (a) Global energy generation by source from 1985 till 2021. The energy generation consists of electricity, heat, and transport. On the left axis, global $CO_2$ emissions from 1985 till 2021. Data from [7]. (b) Global electricity generation by source from 1985 till 2021. Data from [7]. (c) Levelized cost of energy in the U.S. by source from 2009 till 2021. Gas peaker are power plants that ramp up when the electricity demand is high. Data from [8].

Renewable energy technologies, such as solar and wind power, offer promising solutions to the problem of climate change. These technologies harness the power of naturally replenishing resources to generate electricity without emitting greenhouse gases, thus reducing the dependence on finite and polluting fossil fuels. Because of the low operating cost and the increasing mass production, the electricity obtained from renewable sources is already more economical than from fossil production plants (Figure 1.1c) which accelerates the expansion of solar and wind energy.[8] However, while renewable energy offers many advantages, there are also potential risks that must be considered, such as the disruption of wildlife habitats, the degradation of water quality, the usage of toxic materials and the availability of raw materials that are essential for the production of renewable energy.[9–11] Additionally, the increased use of renewable energy sources may result in new challenges related to energy storage and grid integration. Nonetheless, renewable technologies are the best currently available option to cover the high energy demands of the world in the future.[12]

Among the renewables, photovoltaic is the fasted-growing technology today and the sun is the biggest energy resource available on earth.[7,12] In 2021, crystalline silicon (Si) had with 180 GWp annual production 95% of the market share of solar cells where the remaining 5% are shared between copper indium gallium selenide (CIGS), cadmium telluride (CdTe) and hydrogenated amorphous silicon (Si:H) as absorber materials.[13] The reasons for this predominance are mainly the mature technology and the high efficiency of these solar cells. Silicon is the second most abundant material on earth and due to decades of development in electronics it has a proven track record of performance and reliability.[14,15] However, the production process is energy-intensive and therefore expensive and Si by itself is not an ideal absorber material. The low bandgap energy and the high Auger recombination limit the efficiency, and the indirect bandgap requires thick layers (typically above 100 µm) which leads to high material consumption and rigid and heavy solar cells.[16] An alternative that was developed in solar cells around the same time as Si (first generation) is gallium arsenide (GaAs). GaAs is close to be the perfect absorber material with a direct bandgap well matched to the solar spectrum and very low non-radiative energy loss, and GaAs solar cells have reached the so-far highest efficiency of single-junction solar cells with 29.1% (Figure 1.2).[17,18] Nevertheless, both constituents, gallium and arsenic, are toxic and scarce. The lack of raw material and the expensive fabrication conditions make this technology very expensive and not competitive for large-scale deployment.

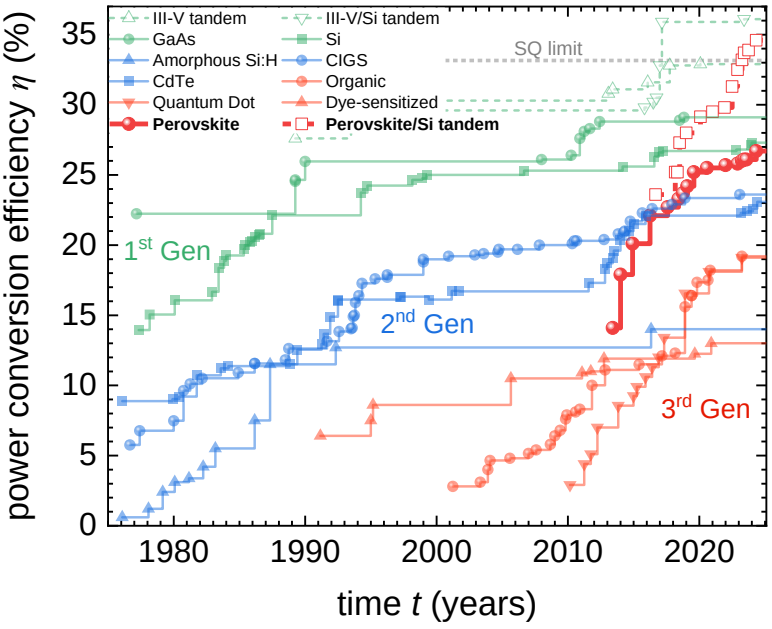


Figure 1.2 Solar cell efficiency chart of chosen photovoltaic technologies. The Shockley-Queisser (SQ) limit in gray defines the maximal theoretical achievable efficiency of a single-junction cell. The hollow symbols mark double-junction (tandem) cells and are not restricted to this limit. Data from [18].

The second generation of solar cells consists of the thin-film technologies CIGS, CdTe and amorphous Si:H that are under-represented on the market.[13] They absorb light more efficiently than Si and can be applied on flexible substrates but often lack power conversion efficiency, rely on toxic or rare materials and/or are more sensitive regarding moisture and oxygen. While CdTe solar cells were represented with 4% share the international market in 2021,[19] CIGS and amorphous Si:H are currently not of commercial interest. Finally, the emerging, 3rd generation of photovoltaics is not yet established at large scale and is still under fundamental investigation. The technologies offer possibilities such as earth-abundant materials, novel applications due to device transparency in the visible, high power-to-weight ratio, and flexible form factors. While organic, dye-sensitized and quantum dot (QD) solar cells still suffer from lower efficiency, perovskite solar cells have become very efficient in a short period of time with lab-scale efficiencies close to Si (Figure 1.2).[18] Thus, perovskite solar cells combine many advantages: they are made from readily-

accessible and cheap materials, feature a tunable direct bandgap, and can be consequently manufactured as thin, lightweight and flexible devices. They can become as economical as Si solar cells or even surpass them and can be integrated in Si solar cells, forming tandem cells with higher efficiencies (Figure 1.2), potentially reducing the price for energy generation even lower.[20] While there are already companies working on the commercialization of perovskite solar cells (such as Oxford PV, Swift Solar and Saule Technologies among others), many hurdles must be overcome before this becomes financially viable, such as upscaling and mass fabrication, Pb toxicity and stability. Additionally, solar cells of this material are fundamentally less understood than Si solar cells which were studied intensively since 1953.[21] Therefore, the physical properties and their limiting impact on perovskite solar cells are the topic of this thesis.

## 1.2 Operating principle of solar cells

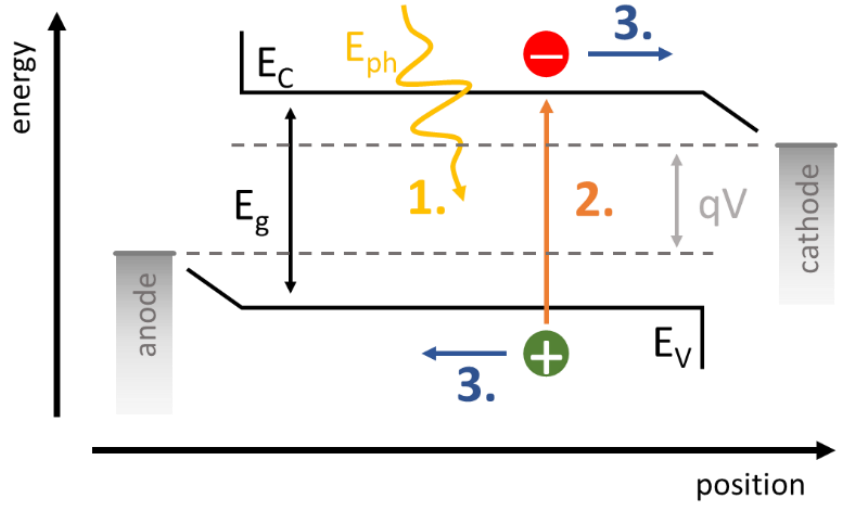


Figure 1.3 Scheme of the band diagram of a perovskite solar cell. A photon with energy $E_{ph}$ entering in the absorber layer with bandgap $E_g$ excites an electron from the valence band with energy $E_V$ to the conduction band with energy $E_C$. Drift and diffusion drive the electrons towards the cathode and the holes towards the anode that have an energy difference $qV$. Adapted from [22].

A solar cell is a device that converts light into electricity. The photovoltaic process can be simplified into three steps as illustrated in Figure 1.3: 1. A photon with energy higher than the bandgap of the absorber, $E_{ph} > E_g$, enters the solar cell. 2. It is absorbed and creates an electron-hole pair by exciting an electron from the valence band $E_V$ to the conduction band $E_C$ of the absorber material. 3. The charge carriers are separated and extracted through the selective contacts. The extraction is influenced by the applied voltage $V$ that creates an energy difference $qV$ between the anode and the cathode.

The ideal, in the sense of the simplest, solar cell is a *p-n* junction using a light-absorbing material. The dependence of the extracted current density $J$ on the voltage $V$ of a *p-n* junction in the dark is formulated by the Shockley **diode equation** which describes the equilibrium between the thermal generation and the recombination of charge carriers due to the applied voltage.[23] The superposition principle states that illuminating the device adds

to the dark current density the voltage-independent, photogenerated current density $J_{gen}$ that flows in the opposite direction,[24]

$$J = J_0 \left[\exp\left(\frac{qV}{n_{id}kT}\right) - 1\right] - J_{gen}. \quad (1.1)$$

Here, $J_0$ is the saturation current density, $q$ is the elementary charge, $n_{id}$ the ideality factor and $kT$ is the thermal energy. The **saturation current density** describes recombination losses which can be split up into radiative and non-radiative recombination ($J_0 = J_{0,rad} + J_{0,non\text{-}rad}$). When a system is in thermodynamic equilibrium, the principle of detailed balance dictates that every microscopic process within the system must be in equilibrium with its corresponding inverse process. Applied to a solar cell in equilibrium that means that a material has to emit light with the same rate that it absorbs light if there are no other recombination processes happening.[25] Therefore, radiative recombination is a necessary loss for a solar cell but non-radiative losses can be avoided. The radiative contribution of the saturation current density in the dark is given by the absorptance $A$ of the material and the radiation $\phi_{BB}$ of a black body at the temperature $T$ of the solar cell evaluated over all photon energies $E_{ph}$,

$$J_{0,rad} = q \int A(E_{ph}) \phi_{BB}(E_{ph}, T) \mathrm{d}E_{ph}. \quad (1.2)$$

Often, $J_0$ is seen as voltage-independent constant which however does not apply to perovskite solar cells and will be further discussed in this thesis. The **ideality factor** ranges typically between 0.75 and 2 is used to describe the voltage dependence of different recombination mechanisms. For an ideal *p-n* junction $n_{id}$ is unity. The recombination mechanisms will be explained in more detail in Chapter 1.3.

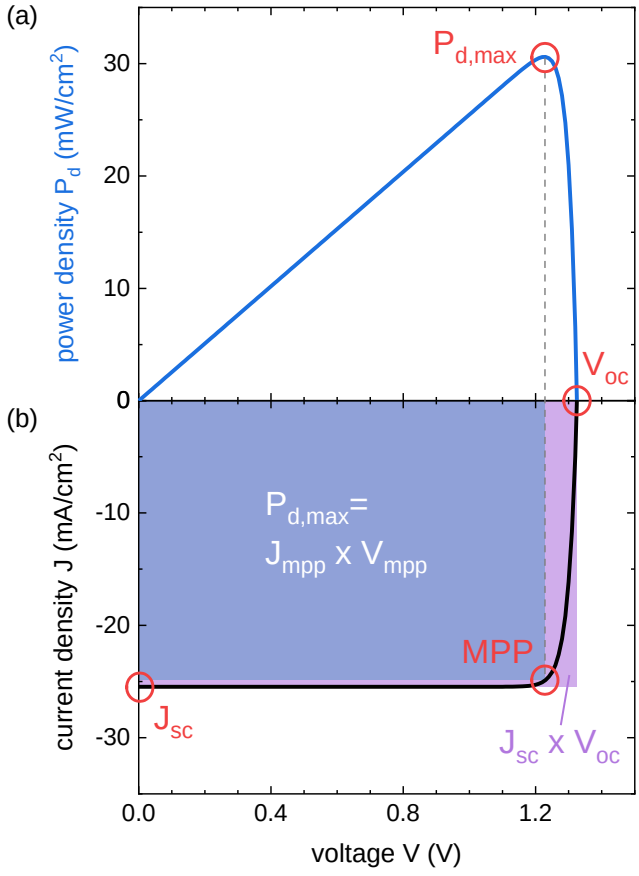


Figure 1.4 (a) Power density $P_d$ and (b) current density $J$ as a function of the applied voltage $V$ of an ideal solar cell with the bandgap $E_g$ = 1.6 eV. Indicated are the short-circuit current density $J_{sc}$, the open-circuit voltage $V_{oc}$ and the maximum-power point (MPP) that is on the $JV$ curve where the maximum power density $P_{d,max}$ is generated. This power density can be also illustrated by the blue area in the $JV$ curve and the ratio of the blue and the violet area gives the $FF$.

Figure 1.4 shows a current-voltage ($JV$) curve for a solar cell under illumination together with the power that can be extracted at each voltage point. The $JV$ curve is the most important characteristic of a solar cell as it tells the efficiency of the device and gives indications about the loss factors and therefore possibilities for improvement. Typically, the performance is discussed with the help of 4 parameters. The **power conversion efficiency (PCE) $\eta$** describes how much of the incoming optical power can be converted into electrical

power. The incoming power is for comparison reasons often fixed to a standardized spectrum of the sun (AM1.5G, 100 mW $cm^{-2}$).[26] Therefore, when I refer to the *JV* curve in this work, I refer to the *JV* curve when the solar cell is illuminated with this one-sun AM1.5G spectrum, unless otherwise noted. The outgoing power is the product of the current density $J_{mpp}$ and the voltage $V_{mpp}$ at the maximum-power point, which is typically represented by the product of the short-circuit current density $J_{sc}$, the open-circuit voltage $V_{oc}$, and the fill factor *FF*,

$$\eta = \frac{P_{\text{out}}}{P_{\text{in}}} = \frac{V_{\text{mpp}}\, J_{\text{mpp}}}{P_{\text{in}}} = \frac{V_{\text{oc}}\, J_{\text{sc}}\, FF}{P_{\text{in}}}. \tag{1.3}$$

The parameters $J_{sc}$, $V_{oc}$, and *FF* are helpful because they enable examining specific mechanisms in the solar cell in an isolated manner. The **short-circuit (SC) current density $J_{sc}$** is measured at a voltage of 0 (see Figure 1.4). Similar to the saturation current density, it can be calculated via

$$J_{\text{sc}} = q \int Q_{\text{E}}^{\text{PV}}(E_{\text{ph}})\phi_{sun}(E_{\text{ph}})\mathrm{d}E_{\text{ph}}, \tag{1.4}$$

where $\phi_{sun}$ is the AM1.5G sun spectrum and $Q_E^{PV}$ is the **external quantum efficiency (EQE)** spectrum, that quantifies the fraction of incident photons with energy $E_{ph}$ that generate charge carriers which are collected at the contacts of the device. The EQE depends on the bandgap of the absorber, the absorption efficiency, and charge collection efficiency of the device. Absorption losses can be further divided into reflection losses and parasitic absorption losses. While the reflectance *R* of the device is straightforward to measure, parasitic absorption occurs in non-active layers and is more challenging to quantify, often leading to inaccuracies in the analysis. **The internal quantum efficiency (IQE) $Q_I^{PV}$** can be defined as the fraction of absorbed photons that generate charge carriers which are collected, and is therefore independent of reflection losses, however still sensitive to parasitic absorption and charge collection issues. In many cases, it is assumed that IQE = 1, so that all absorbed charge carriers are collected, from which follows that $A = Q_E^{PV}$ and thus that the extracted short-circuit current is equal to the photogenerated current density $J_{sc} = J_{gen}$. Therefore, the EQE is often associated with the absorption properties of the absorber layer and the optics of the stack. However, we will see in Chapters 3 and 4 that the assumption of perfect extraction is not generally fulfilled in perovskite solar cells and that recombination even at short-circuit conditions can reduce the $J_{sc}$. At the **open-circuit (OC) voltage $V_{oc}$**, no charge is extracted at all ($J$ = 0), and the charge carriers must

recombine with the same rate as they are generated. Thereby, an equilibrium charge-carrier concentration is formed that defines the $V_{oc}$; the more (non-radiative) recombination, the lower the equilibrium voltage. Solving the diode equation (Equation (1.1) for $V_{oc}$ yields

$$V_{oc} = \frac{n_{id}kT}{q}\ln\left(\frac{J_{gen}}{J_0}+1\right) \approx \frac{n_{id}kT}{q}\ln\left(\frac{J_{sc}}{J_0}\right). \tag{1.5}$$

The approximation is valid because $J_{sc}$ is typically close to $J_{gen}$, even if it is diminished by recombination, and $J_0 \ll J_{sc} \approx J_{gen}$. Finally, the **fill factor *FF*** shows the rectification or "squareness" of the *JV* curve and is calculated according to Equation (1.3) via the ratio of the two squares indicated in Figure 1.4,

$$FF = \frac{V_{mpp}\,J_{mpp}}{V_{oc}\,J_{sc}}. \tag{1.6}$$

The fill factor is especially affected by extraction problems, including series resistance, shunt resistance or extraction barriers.

In presence of **series resistance $R_s$** and/or **shunt resistance $R_{sh}$** limitations, the diode equation from Equation (1.1) needs to be adjusted to

$$J = J_0\left[\exp\left(\frac{q(V-JR_s)}{n_{id}kT}\right)-1\right]+\frac{V-JR_s}{R_{sh}}-J_{gen}. \tag{1.7}$$

Shunt resistance typically arises from fabrication defects that create additional parallel pathways for charge carriers, often due to direct connections of the electrodes. Series resistance, on the other hand, is caused by difficulties to charge movement within the solar cell. Since series resistance is often assumed to be ohmic and constant, it is generally associated with the resistance in the electrodes. The impacts of constant resistances on the $J_{sc}$ and *FF* are discussed in Chapter 3. Other mechanisms such as low mobilities or extraction barriers result in voltage-dependent resistances, which will be quantified in Chapter 4.

To classify the $\eta$, $J_{sc}$, $V_{oc}$, and *FF*, one must know the theoretical limits of these parameters. The **Shockley-Queisser (SQ) model** is based on the thermodynamic principle of detailed balance and calculates the maxima of the 4 parameters for a *p-n* solar cell with just one absorber layer (single junction *p-n* solar cell).[27] In the process, Shockley and Queisser made several assumptions to define an ideal solar cell:

1. The SQ model can be applied to any light source. In the original publication, the source of the photons (the sun) was approximated with a black body of 6000K. While this is a fairly good approximation of the emission spectrum of the sun itself (AM0), earth's atmosphere filters out several wavelength regions, and scattering influences the spectrum as well. Nowadays, it is common to use the AM1.5G spectrum as a reference and I will do so also in this thesis.[28]
2. It is assumed that the absorber layer absorbs all photons with an energy above the bandgap but none below the bandgap. This leads to a step-function absorptance $A = 1$ for $E_g \leq E_{ph}$ and $A = 0$ for $E_{ph} < E_g$. In reality, every semiconductor has tail states that stretch into the bandgap due to structural and thermal disorder. Furthermore, not all photons above the bandgap are absorbed because of a finite absorption coefficient and layer thickness. Reflection losses diminish the absorptance further.
3. Every photon is supposed to create exactly one electron-hole pair. There are methods to create two electron-hole pairs with one high-energetic photon (via spontaneous parametric down-conversion) and therefore break the SQ limit.[29] This is however not yet practical to increase the efficiency of solar cells. In a common solar cell, parasitic absorption of free carriers in the absorber layer or in the contact layers do not generate electron-hole pairs.
4. When a photon with energy $E_g \leq E_{ph}$ is absorbed, it creates an electron-hole pair with an energy higher than the bandgap. In the SQ model, it is assumed that the charge carriers relax (thermalize) to the band edges. The surplus energy is lost at heat that dissipates perfectly into the environment, so that the solar cell and the environment are in thermal equilibrium at a temperature of 300 K. However, the operation temperature of a real solar cell is usually higher than the ambient temperature which reduces the efficiency.
5. Recombination leads to a loss of charge carriers and needs to be avoided. The detailed balance principle implies that radiative recombination has to happen since it is the inverse process to absorption. Therefore, radiative recombination is included in the SQ model, but non-radiative recombination processes are neglected. Therefore, the expression radiative limit is often used as a synonym for the SQ limit, which entails an ideality factor of $n_{id} = 1$. A substantial workload is invested in modern research to achieve this assumption, but sub-gap states due

to imperfections and the inherent Auger recombination (further discussed in Chapter 1.3) inhibit the accomplishment.

6. Finally, the charge carriers need to be extracted. The theory assumes that the external contacts only extract one type of carrier (they are selective). It is further assumed that the contacts do not show any resistive behavior. In reality, both assumptions cannot be ensured as contacts have ohmic losses and are not perfectly selective.

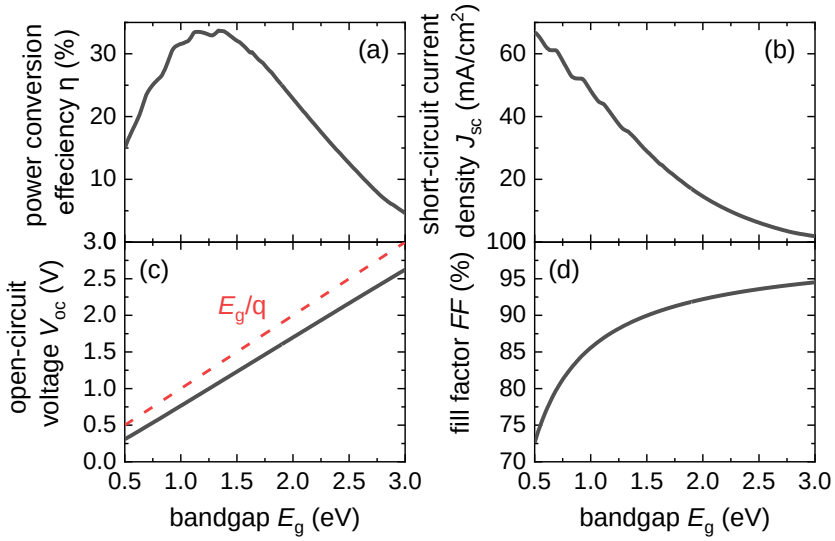


Figure 1.5 SQ limits of (a) the power conversion efficiency $\eta$, (b) the short-circuit current density $J_{sc}$, (c) the open-circuit voltage $V_{oc}$, and (d) the fill factor $FF$ as a function of the bandgap $E_g$ for a single-junction $p$-$n$ solar cell at 300 K. In panel (c), the voltage corresponding to the bandgap energy was plotted as reference.

With these assumptions, the $JV$ curve and the efficiency of a solar cell is solely dependent on the bandgap $E_g$ of the absorber material. The short-circuit current density is then given by

$$J_{sc,SQ} = q \int_{E_g}^{\infty} \phi_{sun}(E_{ph}) \mathrm{d}E_{ph}, \tag{1.8}$$

and the saturation current density by

$$J_{0,\mathrm{SQ}} = q\int_{E_\mathrm{g}}^{\infty} \phi_{\mathrm{BB}}(E_\mathrm{ph}, T)\mathrm{d}E_\mathrm{ph}. \tag{1.9}$$

The open-circuit voltage in SQ limit is

$$V_{\mathrm{oc,SQ}} = \frac{kT}{q}\ln\left(\frac{J_{\mathrm{sc,SQ}}}{J_{0,\mathrm{SQ}}}\right). \tag{1.10}$$

The fill factor does not have an analytical solution, but an empirical formula was found by calculating the *FF* via Equation (1.6) for many bandgaps,[30]

$$FF_\mathrm{SQ} = \frac{\upsilon_\mathrm{oc} - \ln(\upsilon_\mathrm{oc} + 0.72)}{\upsilon_\mathrm{oc} + 1} \tag{1.11}$$

with $\upsilon_\mathrm{oc} = \frac{qV_\mathrm{oc,SQ}}{n_\mathrm{id}kT}$.

Lastly, the efficiency can be calculated according to Equation (1.3)

$$\eta_\mathrm{SQ} = \frac{\max\left[V\left(J_{0,\mathrm{SQ}}\left[\exp\left(\frac{qV}{kT}\right) - 1\right] - J_{\mathrm{sc,SQ}}\right)\right]}{P_\mathrm{in}} = \frac{J_{\mathrm{sc,SQ}}V_{\mathrm{oc,SQ}}FF_\mathrm{SQ}}{P_\mathrm{in}}. \tag{1.12}$$

Figure 1.5 shows the parameters in the SQ limit as a function of the bandgap of the absorber material. $J_{\mathrm{sc,SQ}}$ decreases monotonically with the $E_\mathrm{g}$ because less photons are absorbed, $V_{\mathrm{oc,SQ}}$ on the other hand grows linearly with the bandgap and the $FF_\mathrm{SQ}$ increases weakly as well. This leads to an optimal bandgap region of 1.1-1.4 eV, for which efficiencies up to 33.6% can be expected.

## 1.3 Charge-carrier dynamics

Having discussed the general working mechanisms and performance characteristics of solar cells, I want to detail the physical processes and how to determine them. Therefore, I will change the view now from the external parameters such as current and voltage to the internal parameters like the charge carrier concentration and recombination coefficients. Later in this chapter I will discuss how to connect the external and internal views.

To start I will discuss a semiconductor in the dark with no voltage applied, i.e. in thermal and electrochemical equilibrium. A material is in thermal equilibrium when its temperature is equal to the ambient temperature and the electrochemical equilibrium means that no electrons are excited from the valence band into the conduction band by non-thermal

processes. This also implies no net change of charge carrier concentrations in time. Most of the electrons reside in the valence band and only few are found in the conduction band due to thermal excitation. Likewise, only few holes exist in the valence band. The **equilibrium electron concentration** in the conduction band $n_0$ is given by the occupation probability

$$f_{\mathrm{FD}}(E,T) = \left(1 + \exp\left(\frac{E - E_{\mathrm{F}}}{kT}\right)\right)^{-1} \approx \exp\left(-\frac{E - E_{\mathrm{F}}}{kT}\right), \tag{1.13}$$

that is described by the Fermi-Dirac statistics with Fermi level $E_{\mathrm{F}}$ (Figure 1.6, (1)), and the effective density of states in the conduction band $N_{\mathrm{C}}$,

$$n_0 = N_{\mathrm{C}}\left(1 + \exp\left(\frac{E_{\mathrm{C}} - E_{\mathrm{F}}}{kT}\right)\right)^{-1} \approx N_{\mathrm{C}} \exp\left(-\frac{E_{\mathrm{C}} - E_{\mathrm{F}}}{kT}\right). \tag{1.14}$$

The right-hand side of Equations (1.13) and (1.14) follows from the Boltzmann approximation that is valid if the numerator is much greater than the denominator and that can be applied for all considered cases. Accordingly, the **hole concentration** in the valence band **in equilibrium $p_0$** is given by the occupation probability and the effective density of states in the valence band $N_{\mathrm{V}}$,

$$p_0 = N_{\mathrm{V}}\left(1 + \exp\left(\frac{E_{\mathrm{F}} - E_{\mathrm{V}}}{kT}\right)\right)^{-1} \approx N_{\mathrm{V}} \exp\left(-\frac{E_{\mathrm{F}} - E_{\mathrm{V}}}{kT}\right). \tag{1.15}$$

Note that the Fermi level for both electrons and holes is the same in equilibrium and it indicates the doping of the semiconductor. If the sample is e.g. n-doped, the Fermi level is closer to the conduction band and there are more electrons than holes in the semiconductor. A sample is called intrinsic, if the Fermi level is located in the middle of the bandgap and the electron and hole concentration are of similar size. The product of electron and hole concentration in equilibrium, however, is independent of the Fermi level and just depends on the bandgap of the material and the density of states,

$$n_0 p_0 = N_{\mathrm{C}} N_{\mathrm{V}} \exp\left(-\frac{E_{\mathrm{C}} - E_{\mathrm{V}}}{kT}\right) = N_{\mathrm{C}} N_{\mathrm{V}} \exp\left(-\frac{E_{\mathrm{g}}}{kT}\right) = n_{\mathrm{i}}^2, \tag{1.16}$$

where I defined the intrinsic charge carrier concentration $n_{\mathrm{i}}^2$.

Moving away from the equilibrium situation, excess charge carriers can be generated by thermal, electrical or optical means. For characterization purposes, a solar cell is often electrically driven in the dark which lets it act as a light emitting diode, but in the power generating regime, the generation of charge carriers is solely based on light absorption. In

a first approximation, the light absorption in a solar cell is governed by the absorption in the absorber layer (Figure 1.6, (2)). According to the **Lambert-Beer law**, the light intensity $I$ with incoming light intensity $I_0$ is exponentially decaying inside the material depending on the wavelength-dependent absorption coefficient $\alpha(\lambda)$,

$$I(\lambda, x) = I_0 \exp(-\alpha(\lambda)x). \tag{1.17}$$

In most solar cells, reflections on the multitude of layers lead to interferences that create more complex patterns of absorption but especially for high absorption coefficients where all the light is absorbed in the perovskite layer the Lambert-Beer law is a good approximation.

Therefore, light absorption creates a non-uniform excess carrier distribution $\Delta n(x) = \Delta p(x)$, where most of the carriers are close to the illuminated side. However, drift and diffusion effects drive towards the homogenization of the charge concentration under open-circuit conditions. In the assumption of perfect uniformity over the layer thickness $d$, often the **mean generation rate $G$** is utilized that has the same units as the recombination rate ($s^{-1}$ $cm^{-3}$) and connects to the generated photocurrent via $J_{gen} = qdG$.

The **excess carrier concentration $\Delta n$** under standard illumination conditions is much greater than the intrinsic charge carrier concentration, $n_i << \Delta n$, but doping can introduce an asymmetry in the equilibrium charger carrier concentrations. In the case of a strongly p-doped material, the hole concentration in the dark can be higher than the excess carrier concentration due to a low-level injection, so that $n_0 << n_i << \Delta n << p_0$. Lead halide perovskites, however, are so weekly doped that for the purpose of most applications (including this thesis) they are always in the high-level injection regime and can be assumed as intrinsic,[31] so that the **total carrier concentration $n$** can be approximated by the excess carrier concentration, $n = n_0 + \Delta n \approx \Delta n$ and $n = p$. Therefore, I will discuss the case of an intrinsic semiconductor in the following. Since the semiconductor is not in equilibrium, the electrons in valence and conduction band cannot be described by the same distribution function anymore which leads to a splitting of the Fermi level into two quasi-Fermi levels; one for the electrons in the conduction band $E_{F,n}$ and one for the holes in the valence band $E_{F,p}$,

$$n \approx N_C \exp\left(-\frac{E_C - E_{F,n}}{kT}\right), \tag{1.18}$$

$$p \approx N_V \exp\left(-\frac{E_{F,p} - E_V}{kT}\right). \tag{1.19}$$

Their product is characterized by the intrinsic charge carrier concentration and the **quasi-Fermi level splitting (QFLS) $\Delta E_F$** which is the chemical potential in the absorber layer (Figure 1.6, (3)),

$$np = n_i^2 \exp\left(\frac{E_{F,n} - E_{F,p}}{kT}\right) = n_i^2 \exp\left(\frac{\Delta E_F}{kT}\right). \tag{1.20}$$

The QFLS is a useful parameter because it can be measured directly by photoluminescence spectroscopy as explained later and it gives the upper limit for the open-circuit voltage of the solar cell.

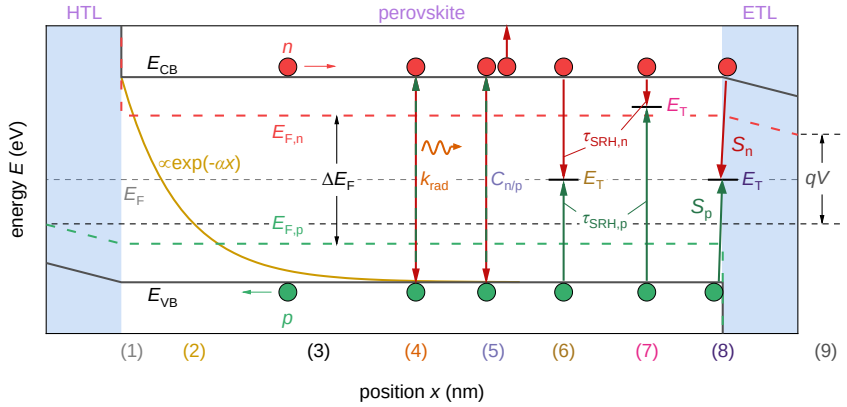


Figure 1.6 Band diagram of a *p-i-n* perovskite solar cell and overview of key characteristics in the carrier dynamics of a semiconductor. (1) Fermi level in equilibrium. (2) Light absorption following the Lambert-Beer law. (3) Quasi-Fermi level splitting $\Delta E_F$ with carrier concentrations $n$ and $p$. (4) Radiative recombination with radiative recombination coefficient $k_{rad}$. (5) Auger recombination on the example of the electron-electron-hole process with Auger coefficient $C_n$. (6) SRH recombination via deep trap with trap energy $E_T = (E_C + E_V) / 2$ and SRH lifetimes $\tau_{SRH,n}$ and $\tau_{SRH,p}$. (7) SRH recombination via shallow acceptor-like trap with trap energy close to the conduction band and SRH lifetimes $\tau_{SRH,n}$ and $\tau_{SRH,p}$. (8) Interface recombination via deep trap with trap energy $E_T = (E_C + E_V) / 2$ and surface recombination velocities $S_n$ and $S_p$. (9) Applied or measured voltage $V$ at the electrodes of the device.

Any disturbed system tends back to its equilibrium state. In the context of excited charge carriers, the function of returning to equilibrium is carried out by **recombination**. As the semiconductor is able to create charge carriers by absorbing photons, detailed balance

requires it to emit photons when electrons and holes recombine. This process is called **radiative recombination** (Figure 1.6, (4)). It is inevitable in a solar cell and therefore already included in the SQ limit. The radiative recombination rate $R_{rad}$ depends on the electron and hole concentration and the radiative recombination coefficient $k_{rad}$,

$$R_{\mathrm{rad}}(n,p) = k_{\mathrm{rad}}\left(np - n_{\mathrm{i}}^2\right) \propto n^2, \tag{1.21}$$

where the proportionality (right-hand side) follows from the assumption of an intrinsic semiconductor and high charge carrier concentration and shows that radiative recombination is a bimolecular process. The radiative recombination coefficient is connected to the absorption coefficient via the van Roosbroeck-Shockley equation,[32]

$$k_{\mathrm{rad}} n_0 p_0 = \int 4n_{\mathrm{r}}^2 \, \alpha(E) \phi_{\mathrm{BB}}(E) \, \mathrm{d}E, \tag{1.22}$$

that equates the spontaneous emission (= radiative recombination) in equilibrium with the absorption of the ambient black-body spectrum $\phi_{\mathrm{BB}}(E) = \frac{2\pi \mathrm{E}^2}{h^3 c^2} \exp\left(-\frac{E}{kT}\right)$ (= charge generation in equilibrium). Here, $n_r$ is the refractive index of the material, $h$ is the Planck constant, and $c$ is the speed of light.

Additionally, there is the possibility of non-radiative recombination processes happening that reduce the solar cell efficiency to below the SQ limit. The aim of solar cell researchers is therefore to reduce them to a minimum. One of these processes is **Auger recombination** (Figure 1.6, (5)) where an electron and a hole recombine, and the excess energy excites an already excited carrier to a higher energy level. The recombination rate $R_{Auger}$ is given by

$$R_{\mathrm{Auger}}(n,p) = C_{\mathrm{n}}\left(n^2 p - n_0^2 p_0\right) + C_{\mathrm{p}}\left(p^2 n - p_0^2 n_0\right) \propto n^3, \tag{1.23}$$

where again the right-hand side is true for an intrinsic semiconductor and the scaling illustrates that three carriers are involved in the process. The Auger recombination coefficients $C_n$ and $C_p$ are material constants.[33,34] As further discussed in Chapter 1.4, Auger recombination is negligible in perovskites for most applications.

Furthermore, I want to discuss **trap-mediated recombination** via the Shockley-Read-Hall (SRH) formalism.[35] Here, electrons and holes recombine via bulk trap states that lay in the bandgap of the semiconductor by phonon transitions. The recombination rate $R_{SRH}$ is dependent on the SRH lifetimes for electrons $\tau_{SRH,n}$ and holes $\tau_{SRH,p}$, and the trap depth $E_T$

that is included in the equation via the detrapping parameters $n_1 = N_C \exp[-(E_C - E_T)/(kT)]$ and $p_1 = N_V \exp[-(E_T - E_V)/(kT)]$,

$$R_{\mathrm{SRH}}(n,p) = \frac{\left(np - n_i^2\right)}{(n+n_1)\tau_{\mathrm{SRH,p}} + (p+p_1)\tau_{\mathrm{SRH,n}}} \propto \begin{cases} n & \text{for} \quad n \gg n_1, p_1 \\ n^2 & \text{for } n_1 \text{ or } p_1 \gg n. \\ n^\delta \ , 1 < \delta < 2, & \text{for } n \approx n_1 \text{ or } p_1 \end{cases} \tag{1.24}$$

It can be seen that the scaling of the SRH recombination can change with the charge carrier concentration. If the charge carrier concentrations are higher than $n_1$ and $p_1$ which is equivalent to the trap level $E_T$ being between the quasi-Fermi levels $E_{F,n}$ and $E_{F,p}$, the trap is considered as deep. A typical example of a deep trap is a trap in the middle of the bandgap where $n_1$ and $p_1$ are minimized and the recombination is maximized (Figure 1.6, (6)). This is the most commonly assumed case of SRH recombination where the recombination scales linearly with n,

$$R_{\mathrm{SRH,deep}}(n) = \frac{n}{\tau_{\mathrm{SRH,p}} + \tau_{\mathrm{SRH,n}}}. \tag{1.25}$$

However, traps can also lay close to the band edges. These traps are called shallow traps (Figure 1.6, (7)). In this case either $n_1$ or $p_1$ dominate, which reduces the recombination due to increased detrapping to the closest band, and the recombination rate scales quadratically with the charge carrier concentration, like radiative recombination. For example, for a trap close to the conduction band, we find

$$R_{\mathrm{SRH,shallow}}(n) = \frac{n^2}{n_1 \tau_{\mathrm{SRH,p}}}. \tag{1.26}$$

The SRH lifetimes are parameters describing the traps and are given by the inverse of the product of trap concentration $N_T$ and the corresponding capture coefficient of electrons $\beta_n$ and holes $\beta_p$,

$$\tau_{\mathrm{SRH,n/p}} = \frac{1}{N_T \beta_{\mathrm{n/p}}}. \tag{1.27}$$

The SRH recombination is the fastest-acting and therefore dominant recombination mechanism in most semiconductors. This leads to recombination losses in comparison to the radiative recombination. Therefore, it is beneficial to increase the SRH lifetimes as this

reduces the non-radiative losses. This can be achieved e.g. by reducing the concentration of defects in the crystal because these can lead to traps in the bandgap. In a perfect crystal, the trap density $N_T$ goes to zero, resulting in infinitely long SRH lifetimes.

In addition to the bulk, recombination via traps can also happen at the interface of two materials or a bare surface. The **surface recombination rate $R_{surface}$** can be defined similar to SRH recombination (Figure 1.6, (8)), however only at a thin two-dimensional surface with thickness $\delta x$,

$$\delta x\, R_{\mathrm{surface}}(n,p) = \frac{np - n_{\mathrm{i}}^2}{\frac{(n+n_1)}{S_p} + \frac{(p+p_1)}{S_{\mathrm{n}}}}, \tag{1.28}$$

where $S_n$ and $S_p$ are the surface recombination velocities for electrons and holes, respectively, that are parameters defining the kinetics of the transition, in analogy to $\tau_{SRH,n}$ and $\tau_{SRH,p}$. The surface recombination velocities however should be as low as possible to be able to neglect the surface recombination. Typically, at an interface in a solar cell, there is a majority and a minority carrier, e.g. at the interface of the perovskite with the ETL, there should be more electrons than holes. Therefore, only $S_p$ is important and vice versa at the HTL interface. For simplification, these two surface recombination velocities at both interfaces are often set as equal, $S = S_{n,HTL} = S_{p,ETL}$. Then the surface recombination velocity can be connected to a surface lifetime $\tau_s$ via

$$\tau_{\mathrm{s}} = \frac{d}{2S} + \frac{1}{D}\left(\frac{d}{\pi}\right)^2, \tag{1.29}$$

where $D$ is the diffusion coefficient that is assumed equal for electron and holes. The first term stands for the actual recombination, averaged over the layer thickness, and the second term for the diffusion through the layer, in case the transport is the limiting process. If, however, the diffusion is fast, only the first term remains.

All these recombination mechanisms add up to a total recombination rate $R_{tot}$ that can have a complicated dependence on the charge carrier concentration. The **effective charge carrier lifetime $\tau_{eff}$** can be defined via

$$\tau_{\mathrm{eff}}(n) = \frac{\Delta n}{R_{\mathrm{tot}}(n)}, \tag{1.30}$$

that also changes generally with charge carrier concentration in contrast to the SRH and surface lifetimes. Only in the case that the total recombination is dominated by a deep defect either in the bulk or at the surface, the effective carrier lifetime becomes constant over a specific regime.

With this knowledge, I want to connect some internal parameters with external, measurable parameters. The simple 1-diode equation (Equation (1.1) can be motivated by noting that the rate of extracted electrons can be described by the difference between charge generation and the voltage-dependent recombination. To get the current density, one needs to multiply the extraction rate by the electron charge and the device thickness,

$$\begin{aligned} J(V) = qd(R_{\mathrm{tot}}(V) - G) &= qd\left[\frac{\Delta \mathrm{n}}{\tau_{\mathrm{eff}}(n)} - G\right] \\ &= qd\left[\frac{n_{\mathrm{i}}}{\tau_{\mathrm{eff}}(V)}\left(\exp\left(\frac{qV}{2kT}\right) - 1\right) - G\right], \end{aligned} \tag{1.31}$$

where the voltage dependence follows from Equation (1.20) under assumption of $n = p$ and the -1 term from the definition of $R_{\mathrm{tot}}$ with the excess instead of the total carrier density. Furthermore, it was assumed that the QFLS $\Delta E_{\mathrm{F}}$ inside the perovskite, a chemical potential, translates directly into the voltage $V$ between the electrodes, an electrostatic potential, $\Delta E_{\mathrm{F}} = qV$. In practice, a difference between the voltage and the QFLS can occur (Figure 1.6, (9)), as I will discuss further in Chapter 4. The voltage dependence of the effective lifetime is often transferred into the ideality factor, so that Equations (1.1) and (1.31) are equivalent, where $J_0 = \frac{qdn_{\mathrm{i}}}{\tau_{\mathrm{eff}}(0V)}$.

Another key measurable parameter in the characterization of perovskite solar cells is the **photoluminescence (PL)**, which arises as a direct consequence of radiative recombination. Each radiative recombination event corresponds to the emission of a single photon, establishing a direct relationship between recombination rate and light intensity. However, not all photons generated within the perovskite layer escape the sample. Processes such as reflection, reabsorption, and parasitic absorption within the material and surrounding architecture influence the amount of emitted light. Consequently, the detectable PL intensity is attenuated relative to the radiative recombination rate by the escape probability $p_{\mathrm{e}}$. Furthermore, the measured photon flux $\phi_{\mathrm{PL}}$ cannot discriminate the depth of the photon generation, corresponding to the integral over the layer thickness,

$$\phi_{\mathrm{PL}} = \int_0^d p_{\mathrm{e}}\, R_{\mathrm{rad}}\, \mathrm{d}x = \int_0^d \mathrm{p_e} k_{\mathrm{rad}}\, np\, \mathrm{d}x = \int_0^d \mathrm{p_e} k_{\mathrm{rad}} n_{\mathrm{i}}^2 \exp\left(\frac{\Delta E_{\mathrm{F}}}{kT}\right) \mathrm{d}x\,. \tag{1.32}$$

Therefore, the PL intensity is a measure of the product of the charge carrier concentrations *np* and of the QFLS, following Equation (1.20). This relationship is particularly valuable as it enables a non-contact method to probe the maximum achievable $V_{\mathrm{oc}}$ of a sample, and this thesis makes extensive use of it to assess device performance. However, Equation (1.32) cannot be directly applied because the parameters $k_{\mathrm{rad}}$, $p_{\mathrm{e}}$, and $n_{\mathrm{i}}$ are typically unknown. Nevertheless, assuming all quantities as position-independent and using the van Roosbroeck-Shockley equation (Equation (1.22)), the generalized Planck law can be derived,[36] which extends black-body radiation to semiconductors out of equilibrium by incorporating the QFLS,

$$\phi_{\mathrm{PL}}^{\mathrm{E}}(E) = A(E)\, \phi_{\mathrm{BB}}(E) \exp\left(\frac{\Delta E_{\mathrm{F}}}{kT}\right) = \frac{2\pi E^2}{h^3 c^2}\, A(E) \exp\left(-\frac{E - \Delta E_{\mathrm{F}}}{kT}\right). \tag{1.33}$$

Here, the spectral photon flux $\phi_{\mathrm{PL}}{}^{\mathrm{E}}$ is the emitted photon density per time and energy interval (typically in units of $\mathrm{cm^{-2}\,s^{-1}\,eV^{-1}}$). We find that the absorptance of the film shapes the PL spectrum by shifting its emission peak and altering its intensity, while the QFLS enhances the emission energy-independent (Figure 1.7a).

If the complete absorption spectrum is known, especially extending into sub-bandgap region, and the PL can be measured in absolute photon numbers, it becomes possible to calculate the QFLS. However, accurately measuring the entire absorption spectrum is often impractical. As a good approximation for absorber layers, one can assume a flat absorptance close to 1 above the bandgap, which simplifies the energy dependence,

$$\ln\left(\frac{h^3 c^2 \phi_{\mathrm{PL}}^{\mathrm{E}}(E)}{2\pi A E^2}\right) = \frac{E}{kT} - \frac{\Delta E_{\mathrm{F}}}{kT}. \tag{1.34}$$

Therefore, a linear **fit using the high-energy tail** of the spectrum yields the carrier temperature *T* and the QFLS (see also Figure 4.3a).

A commonly employed, simpler alternative is to estimate the **external photoluminescence quantum yield (PLQY)** $\boldsymbol{Q_{\mathrm{e}}^{\mathrm{PL}}}$, which is the ratio of the emitted photon flux $\phi_{\mathrm{PL}}$ over the absorbed photon flux $\phi_{\mathrm{abs}}$,

$$Q_e^{PL} = \frac{\phi_{PL}}{\phi_{abs}} = \frac{p_e k_{rad} np}{(p_e + p_a) k_{rad} np + R_{non-rad}}. \tag{1.35}$$

where the steady-state condition was employed, implying that carrier generation and recombination need to be equal. Additionally, it includes the possibility that an emitted photon is parasitically absorbed by another layer with the probability $p_a$.

The PLQY provides an indirect measure of the QFLS as it quantifies the deviation from the radiative limit. Using Equation (1.5), we can derive the connection between the QFLS and the PLQY,

$$\begin{aligned} \Delta E_F = \mathrm{kT} \ln\left(\frac{J_{sc}}{J_0}\right) = \mathrm{kT} \ln\left(\frac{J_{sc}}{J_{0,rad}}\right) + \mathrm{kT} \ln\left(\frac{J_{0,rad}}{J_0}\right) = V_{oc,rad} + \mathrm{kT} \ln\left(\frac{\phi_{PL}}{\phi_{abs}}\right) \\ = V_{oc,rad} + \mathrm{kT} \ln(Q_e^{PL}) = V_{oc,rad} - \Delta V_{oc,non-rad}. \end{aligned} \tag{1.36}$$

In this case, the current densities refer to the charge carrier densities leaving only the absorber layer instead of the complete solar cell as usual. As the PLQY is based on the integration over the PL peak instead on a fit, this method is typically more robust to noise in comparison to the high-energy tail fit and it is independent of the assumption of a flat absorption spectrum.

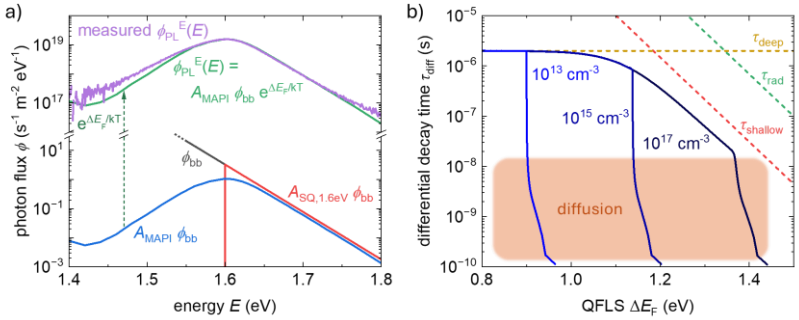


Figure 1.7 a) Explanation of the formation of the PL spectrum by the product of black-body spectrum, the absorptance of the film and the scaling by the QFLS. The SQ limit of the absorptance and the experimentally measured PL are shown for comparison. A temperature of 300 K and a QFLS of 1.13 eV were assumed. b) Simulated differential decay time as a function of the QFLS for three starting conditions ($n(0)$=$10^{13}$, $10^{15}$, $10^{17}$ cm$^{-3}$). The simulation includes radiative recombination ($k_{rad}$ = 3×$10^{-11}$ cm$^3$ s$^{-1}$), one shallow trap ($E_T$ = 1.59 eV, $N_T$ = $10^{16}$ cm$^{-3}$, $\tau_{SRH,n}$ = $\tau_{SRH,p}$ = $10^{-9}$ s), one deep trap ($\tau_{SRH,n}$ = $\tau_{SRH,p}$ = $10^{-6}$ s) and diffusion ($\mu_n$ = $\mu_p$ = 10 cm$^2$ V$^{-1}$ s$^{-1}$) due to an inhomogenous charge generation ($\alpha$ = 4×$10^5$ cm$^{-1}$). The isolated effects of the recombination mechanisms are indicated by the dashed lines. The diffusion is marked by the orange area corresponding to early delay times after the excitation.

Finally, the PL can also be measured as a transient. In this **time-resolved photoluminescence (TRPL)**, a short laser pulse excites the sample, and the decaying PL signal is registered. Just as the steady-state PL, this measurement scales with $n^2$, so effectively one can measure the decay of the charge carrier concentration, which explains its usage to extract the effective charge carrier lifetime. However, in a transient, there is no fixed recombination rate and trap occupation, instead trapping, detrapping, drift and diffusion change over time and need to be considered. Therefore, the lifetime $\tau_{diff}$ from a transient measurement can differ from $\tau_{eff}$. The differential decay time from a TRPL measurement can be determined via[37]

$$\tau_{\mathrm{diff}} = -2\left(\frac{\mathrm{d}\ln\phi_{PL}}{\mathrm{d}t}\right)^{-1}. \tag{1.37}$$

After long times, drift and diffusion effects often become negligible, leaving recombination as the primary mechanism influencing charge carrier dynamics (Figure 1.7b). If a deep trap dominates, the decay of electrons and holes occurs linear with their concentration, leading to an exponential PL decay. Under these conditions, the differential decay time becomes constant, $\tau_{diff}$ = $\tau_{SRH,p}$ + $\tau_{SRH,n}$, mirroring the steady-state case in Equation (1.25). A similar

scenario applies to deep surface traps, as described by Equation (1.29). If, however, any other kind of recombination dominates, $\tau_{\mathrm{diff}}$ will change in time and charge carrier concentration, potentially deviating from the steady-state results. If several recombination mechanisms are active simultaneously, their lifetimes sum up inversely, $\tau_{\mathrm{tot}} = \left(\frac{1}{\tau_{\mathrm{rad}}} + \frac{1}{\tau_{\mathrm{SRH}}} + \frac{1}{\tau_{\mathrm{s}}} + \cdots\right)^{-1}$.

## 1.4 Perovskite solar cells

In this thesis, I deal exclusively with solar cells using metal halide perovskites as absorber layer. Perovskites in general describe a class of materials that are defined by their common crystal structure. The first mineral of this class, $CaTiO_3$, was discovered in a sample from the Urals by German scientist Gustav Rose in 1839 and named in honor of Count Lev Perovski, a Russian politician and mineralogist.[38] Nowadays, they are intensively investigated, as silicate perovskites are the most abundant materials inside the lower mantle of the Earth and other planets and engineered perovskites can be used for many applications such as scintillators, high-temperature superconductors, catalysis, light-emitting diodes (LEDs), lasers, and more.[39–43] Recently, metal halide perovskite solar cells were found as a promising candidate to tackle climate change as discussed in Chapter 1.1. Perovskites have the formula $ABX_3$ (Figure 1.8a), where for metal halide perovskites A is a monovalent cation, B is a bivalent cation, and X is a monovalent anion. For simplicity of language from now on, I will use the term perovskite exclusively for metal halide perovskites except otherwise stated. For this class of perovskites, the bivalent cation B is usually lead ($Pb^{2+}$) or tin ($Sn^{2+}$), and the monovalent anion X can be iodide ($I^-$), bromide ($Br^-$) or chloride ($Cl^-$). The A cation is often either methylammonium (MA: $CH_3NH_3^+$), formamidinium (FA: $CH_2(NH_2)_2^+$) or cesium ($Cs^+$), but other cations like Na, K, Rb, guanidinium (GUA: $C(NH_2)_3^+$) and more can be mixed in when used in small quantities. The deciding factor is the stability of the crystal lattice that depends on the size of the employed constituents. Norwegian mineralogist Viktor Goldschmidt found that perovskites are stable if their tolerance factor $t_{\mathrm{tol}}$, given by a ratio of the ionic radii $r_{\mathrm{A}}$, $r_{\mathrm{B}}$, and $r_{\mathrm{X}}$ of the ions A, B and X,

$$t_{\mathrm{tol}} = \frac{r_{\mathrm{A}} + r_{\mathrm{X}}}{\sqrt{2}(r_{\mathrm{B}} + r_{\mathrm{X}})}, \tag{1.38}$$

is between 0.8 and 1.[44] Perovskites with $0.9 < t_{tol} < 1$ form cubic crystal structures (as illustrated in Figure 1.8a), for lower values the lattice is more distorted and becomes tetragonal or orthorhombic.[45] If larger A cations are incorporated and the tolerance factor is over 1, lower-dimensional perovskites can form. For solar cells for instance, it is a common strategy to employ a thin two-dimensional perovskite layer on top of a three-dimensional perovskite absorber for defect passivation and lattice stabilization.[46] A very important feature of perovskites is that the bandgap changes depending on the incorporated ions (Figure 1.8b). The bandgap is increased for smaller halides or bigger metals, but the A cation changes $E_g$ only slightly. The bandgap tunability enables different applications of metal halide perovskites in optoelectronic devices; LEDs are mostly used in the visible range; solar cells need a lower bandgap depending on whether they are used in single- or multi-junction devices.

The first solar cell employing perovskite was a dye-sensitized solar cell in 2009 utilizing $MAPbI_3$ and $MAPbBr_3$ as a dye to absorb light in a matrix of mesoporous $TiO_2$ for electron extraction.[47] The $MAPbI_3$-based device achieved a PCE of 3.8% but was not air-stable; a problem that still remains under study. It was not until 2012 that perovskite-sensitized solar cells were picked up on for improvements and it was demonstrated that perovskites have good charge transport properties, so that the mesoporous $TiO_2$ scaffold was not necessary.[48,49] Since then, the number of publications referring to perovskite solar cells increased rapidly and so did the efficiency (up to 26.7%, as was already shown in Figure 1.2).

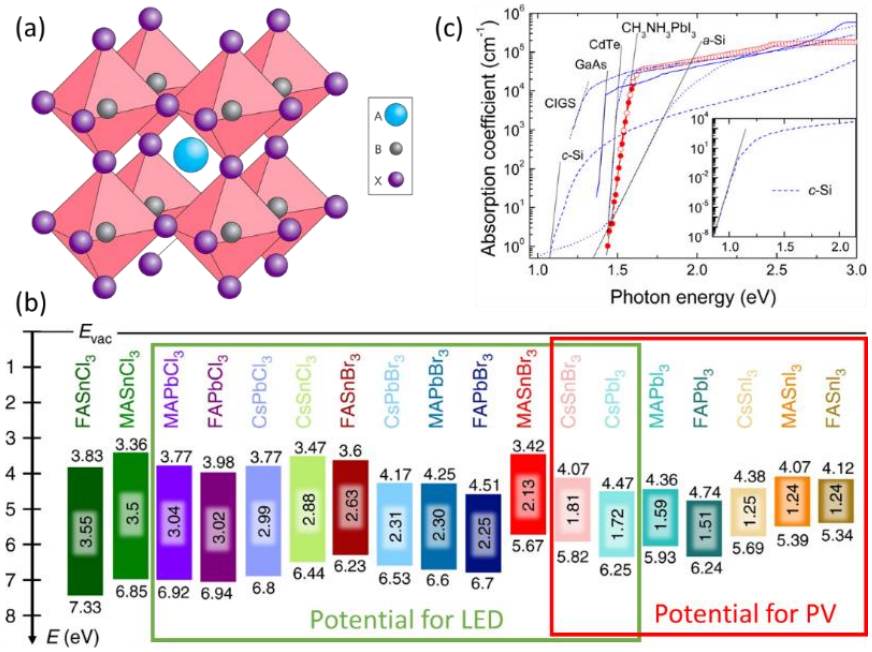


Figure 1.8 (a) Crystal structure of perovskites. A is a monovalent cation, B a bivalent cation and X is a monovalent anion. Reproduced with permission from ref [50]. (b) Energy level diagram of the fundamental perovskites used in opto-electronic devices with corresponding valence-band energy $E_V$, optical bandgap $E_g$ and conduction-band energy $E_C$ away from the vacuum level $E_{vac}$. The red box marks the perovskites potentially interesting for photovoltaic (PV) applications and the green box marks perovskites for visible LEDs. Adapted with permission from ref [51]. (c) Absorption coefficient of typical photovoltaic materials. The straight lines correspond to the slope of the Urbach tail. The inset shows the low absorption values of crystalline silicon (c-Si). Reproduced with permission from ref [52].

The origin of the high performance lays in some of the physical properties that make perovskites close to ideal candidates as absorber layer for PV applications.[53] In the following, I will discuss the most important characteristics of perovskites for solar cells.

Even for a direct bandgap material, they have especially high absorption coefficients already close to the bandgap energy, with a steep decay in the bandgap (Figure 1.8c).[52,54] The high absorption coefficient enables the use of very thin films (< 1 µm) to absorb the sunlight fully in a step-function-like fashion without the necessity of complicated light-trapping mechanisms, leading to high $J_{sc}$ values.

On the other hand, the low Urbach energy $E_U$, defined by the slope of the sub-bandgap absorption edge, indicates low disorder of the crystal lattice (thermal or structural),

especially the absence of long-range disorder.[54,55] This is highly beneficial for a photovoltaic technology because strong disorder with Urbach energies above the thermal energy ($E_U$ < 25.8 meV at room temperature) are associated with substantial $V_{oc}$ losses.[52,56] Lead halide perovskites have shown the potential for low Urbach energies between 12 and 20 meV which are on par with values from highly crystalline GaAs or Si, but other compositions demonstrated significantly higher values.[54,57] In Chapter 3, I will discuss the effect of the Urbach tail on the performance in co-evaporated perovskite solar cells.

Another intrinsic feature in semiconductors is Auger recombination that limits the maximum $V_{oc}$ of, for instance, Si solar cells.[33,58,59] While the ambipolar Auger recombination coefficient in perovskites is even higher than in Si,[33,34] this type of recombination is negligible when operating the cell under standard conditions.[60] The reason is again the high absorption coefficient that directly correlates with a high radiative recombination coefficient because of the detailed balance principle.[32] Therefore, at charge carrier densities corresponding to 1-sun illumination conditions, the charges decay faster due to radiative recombination than due to Auger recombination. Just under high concentrations of sun light, Auger effects play a role due to their scaling with $n^3$.

Finally, SRH recombination due to crystal defects such as interstitials, vacancies, impurities or dangling bonds at grain boundaries and surfaces diminishes the $V_{oc}$ if their energy lies in the bandgap. As one advantage of metal halide perovskites, it is discussed that many point defects have transition energies in or close to the valence or conduction band (shallow traps) and the defects that lay deep in the bandgap have high formation energies.[61–64] This permits to produce perovskite films with low temperature processes that might have a high defect density but still good electronic properties. Furthermore, perovskites are found to have a low intrinsic doping density as mentioned before.[31] This indicates that there is not a specific predominant defect which would effectively dope the material. Nonetheless, it remains a complex engineering challenge to form the perovskite layer in such a way that the crystal contains as little as possible in-gap states. Perovskite films with outstanding external PLQYs up to 66% indicating internal PLQYs close to 100% and carrier lifetimes over several microseconds have shown that the challenge can be tackled.[34,65–72] This is however not universal to all perovskites as will be shown in chapter 5. Concluding the above-mentioned arguments, perovskites show the potential of achieving high open-circuit voltages close to the SQ limit.

Nevertheless, to achieve high PCEs, not only does the recombination have to be minimized but the charges must be well separated and collected, too. Electrons and holes are created locally close to each other upon photon absorption. Depending on their electrostatic Coulomb forces they might form a bound state which is called an exciton. These excitons need to be separated, as excitons travel slow, the opposite charge carriers need to be collected at opposite sides of the solar cell and the proximity of them increases the recombination coefficient, which reduces the time available for collection. Beneficially for opto-electronic devices, the exciton binding energies $R^*$ of perovskites with bandgaps interesting for PV is below the thermal energy at room temperature ($R^* < kT = 25.8$ meV) which means that the charge carriers separate immediately after generation into free carriers. On the other hand, perovskites with higher bandgaps have higher exciton binding energies, efficiently increasing the electroluminescence quantum yield in LEDs.[73,74]

Once the charge carriers are separated, they need to be transported towards their corresponding electrode which can happen via drift by an electric field or via diffusion. Both processes are affected by the charge carrier mobility of the material. The mobility of the free charges in perovskites is with 1-100 $cm^2\ V^{-1}\ s^{-1}$ low in comparison to inorganic semiconductors such as Si or GaAs (> 400 $cm^2\ V^{-1}\ s^{-1}$) but higher than in organic semiconductors (< 0.01 $cm^2\ V^{-1}\ s^{-1}$) which additionally suffer from strongly-bound excitons.[75–77] Due to the long lifetimes, the mobility is sufficient to yield diffusion lengths above 1 µm, which is consequently longer than the typical perovskite thicknesses of 0.1 – 1 µm in solar cells that arise from the high absorption coefficient.[78]

As diffusion hence suffices for efficient charge transport, additional support from a built-in electric field is not necessary. This is advantageous because in perovskites mobile ions can move to screen a field applied over the layer so that drift barely plays a role in the perovskite layer.[79–83] Mobile ions are a big topic in perovskite solar cells because their existence directly indicates an instability of the crystal lattice – ideally the ions should be fixed in their lattice position. Therefore, mobile ions are often discussed in relation to the fast degradation that is still impeding the commercialization of perovskite solar cells.[84–87] Furthermore, the field screening leads to effects in dynamic measurements, especially to hysteresis in *JV* curves, which are dependent on the scan speed and direction, but also to changes in techniques as impedance spectroscopy and transient photovoltage.[83,88–90] It was shown that, while the unwanted hysteresis can be reduced, the mobile ions are intrinsic to perovskites and low activation energies were theoretically and experimentally found for the

ion migration.[79,91–93] In this thesis, however, the influence of ions is of minor relevance, as only freshly fabricated solar cells were investigated, and these exhibited no signs of hysteresis under the applied measurement conditions. All-in-all, perovskites show a high potential as an absorber layer in solar cells.

For a solar cell to work however, an asymmetry needs to be introduced into the device to motivate the charge separation and extraction to the external circuit. Therefore, I want to discuss the device architecture shortly. Typically, the charge separation is realized via an electron and a hole transport layer (ETL and HTL, respectively) sandwiching the perovskite film. There are certain requirements for such a charge transport layer (CTL). For example, an ETL ought to have a high electron mobility, and its conduction band should be well aligned with the conduction band of the perovskite to ensure efficient electron extraction. The valence band of the ETL should be at a lower energy than the perovskite's valence band to block holes. Additionally, a low hole mobility is beneficial. Finally, the layer needs to be as transparent as possible which is often achieved by very low thicknesses.

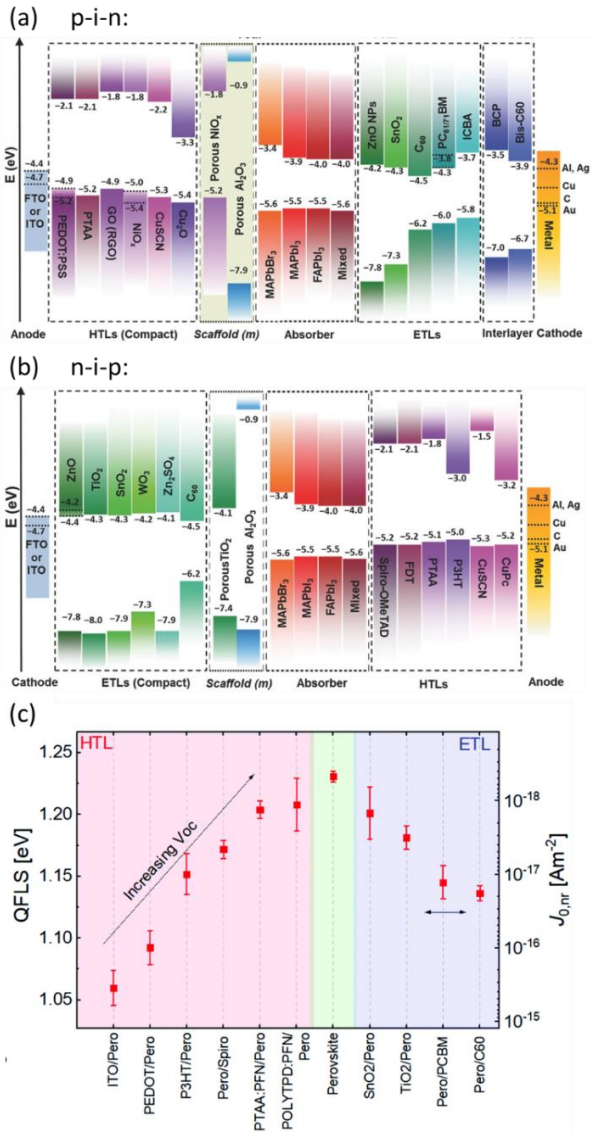


Figure 1.9 Energy level diagram for representative metal halide perovskites and CTLs relevant for (a) *p-i-n* and (b) *n–i–p* configuration. dotted lines correspond to material work function. Reproduced with permission from ref [94]. (c) The quasi-Fermi level splitting of heterojunctions of the perovskite layer with different hole and electron transporting materials using absolute photoluminescence measurements. Reproduced with permission from ref [94].

Practically, it makes a difference which CTL is on which side of the perovskite, so it is often distinguished between *p-i-n* and *n-i-p* configurations; *n* and *p* representing the ETL and HTL, respectively, and *i* representing the intrinsic perovskite. The main reason for this distinction is the fabrication process employed.

Typically, perovskite solar cells are grown on glass substrates, covered with a transparent conductive oxide (TCO) layer (on the left side of panels a and b in Figure 1.9). The TCO acts as an electrode for effective charge collection over long distances (mm-cm) and is made of a material that is transparent to visible light and conducts electricity well, such as indium tin oxide (ITO) or fluorine-doped tin oxide (FTO).

On top of the TCO, the semiconductor layers are deposited which define the configuration. Due to the requirements discussed above, there is a limited number of materials that are suitable as CTLs in perovskite solar cells. An overview of typical materials in *p-i-n* and *n-i-p* configuration is given in Figure 1.9a and b, respectively. There are partly different materials for both configurations, because the deposition method and the material chemistry must be compatible with the rest of the solar cell.

For the bottom layer (the one directly on top of the TCO), the fabrication requirements are comparatively low because the TCO is usually thermally and chemically stable.[95] The main requirement is that the perovskite must grow well on it, without introducing many electronic states in the bandgap due to surface chemistry or crystal defects that reduce the quasi-Fermi-level splitting. The reduction can be determined via steady-state photoluminescence on the heterojunctions (Figure 1.9c). This negative effect may be reduced by the introduction of a thin passivation layer between the bottom CTL and the perovskite.[96]

Additionally, the bottom layer needs to withstand the deposition of the perovskite film and, similarly, the deposition of the top layer (on top of the perovskite) should not harm the perovskite. The protection of the underlying layers is of great importance as perovskite solar cells are often fabricated via solution-processing methods. The solvent of the added layer should not dissolve the underlying layer as well. Therefore, either materials of different polarity must be chosen, or a bottom polymer may be crosslinked to reduce their solubility. This factor excludes many CTLs as a top layer that are useful as bottom layers, and it renders the fabrication of complex devices with many layers such as perovskite tandem solar cells difficult.[97] Therefore, vapor deposition techniques like atomic layer deposition (ALD), pulsed laser deposition (PLD), sputtering and thermal evaporation are used that

impose different requirements. Sputtering for example usually has a high impact energy that can damage soft materials as perovskites. The perovskite solar cells used in this thesis are fully fabricated by thermal evaporation (with a few exceptions detailed in Chapter 2.1). Thermal evaporation enables additive processes, i.e. different layers can be deposited on top of each without damaging the underlaying layers. Furthermore, it allows for homogenous and flat films with a good thickness control. However, not all materials can be used in this technique as some might decompose before vaporizing or they sublime at very low temperatures which makes the process difficult to control. Therefore, this method can also restrict the choice of materials and often a combination of deposition methods are used to fabricate a complete solar cell.

After the addition of the perovskite and the top CTL, the top electrode is deposited on the stack, typically made of a material such as gold or silver. In principle, on both sides TCOs can be used to create a bifacial cell, that can collect light from both sides. The use of a metal electrodes is however often preferred, because the metals show lower resistive losses and can act additionally as a back mirror for the light that passes through the absorber layer. The reflection of not-absorbed light allows to reduce the thickness of the absorber layer, reducing costs and potentially increasing efficiency.

The distinction between the fabrication methods of the perovskite film is especially important in view of the motivation of this thesis. In 99.5% of publications, the perovskite is deposited via solution processing, mostly via spin coating.[98] Spin coating is a simple and low-cost technique that can produce complex perovskite formulations in a fast way as a multitude of precursors can be mixed in a solution. Due to these advantages solution-processing is the most-explored fabrication technique for perovskites and most characterization works are based on them. Co-evaporation is a more cost-intensive and complex fabrication method and is therefore less investigated for perovskite films. However, it is important to understand this technology on a lab scale, as it is relevant for fabricating perovskites on an industrial scale. An advantage is the precise control over the deposition rates of each precursor materials which enables high stoichiometric control and danse, pinhole-free films with a smooth surface. The uniform layers with a consistent thickness across large substrate enable scalability for large-area applications. The controlled environment leads to higher reproducibility and independence of manual skill and an integration into existing vacuum-processing setups is facilitated. Finally, the solvent-free processing avoids potential health hazards and solvent-induced defects. In this thesis, I

exclusively investigate co-evaporated perovskite films. Although these films are nominally the same material as those produced by other methods, perovskites fabricated with different techniques can exhibit distinct characteristics.[37,99–106] These aspects are significantly less studied in co-evaporated perovskites compared to solution-processed counterparts.

## 1.5 Aim of the thesis

Although the PCE of perovskite solar cells has demonstrated the fastest progress among solar technologies to date, the rate of improvement has recently started to level off. Consequently, it is essential to explore the underlying mechanisms more deeply that continue to limit PCE. Since solution-processed perovskites have been extensively studied due to their predominant use in solar cells, the characteristics of vacuum-deposited perovskites, which exhibit distinct growth and interface properties, require further investigation. The aim of this thesis is therefore to identify the factors responsible for performance losses in co-evaporated perovskite solar cells.

- To this end, **Chapter 3** will give an overview of the limiting device parameters in terms of $V_{oc}$, $J_{sc}$, and *FF* in four types of co-evaporated perovskite solar cells with bandgaps ranging from 1.52 to 1.88 eV. These parameters will be evaluated against their theoretical limits to quantify their contribution to overall PCE losses. Furthermore, the origins of $V_{oc}$ losses will be dissected into contributions from $J_{sc}$ losses, radiative recombination and non-radiative recombination via sensitive EQE measurements. The influence of the absorption tail and the Urbach energy will be addressed, and *FF* losses will be related to $J_{sc}$ losses.
- In **Chapter 4**, the focus shifts to a more detailed examination of *FF* and $J_{sc}$ losses. Voltage-dependent PL measurements are presented as a tool to characterize recombination losses during charge extraction, indicating current losses. The voltage-dependent PLQY will be determined at each bias point, and the expected *JV* curve in the limit of perfect charge transport will be discussed.
- Finally, **Chapter 5** will investigate the source of non-radiative $V_{oc}$ losses in co-evaporated perovskite solar cells. Recombination can occur either in the bulk of the perovskite or at the interfaces with the CTLs. Identifying the primary site of recombination is critical for optimizing device performance, as this will

dictate the dominant source of $V_{oc}$ losses that must be reduced. The investigation is conducted via a combination of JV measurements, PL measurements on the perovskite film and the complete device, and drift-diffusion simulations. Additionally, surface recombination of the bare perovskite film is explored via PL measurements employing a multitude of passivation materials and TRPL measurements.

# 2 Experimental Methods

In this chapter, I introduce the experimental methods required to obtain the results of these doctoral studies. As several setups in Chapters 2.3 and 2.4 were either developed or refined during this research, and since the results largely depend on these methods, these chapters contain more detailed descriptions compared to other sections.

## 2.1 Sample preparation

It should be noted that, due to the focus on characterization, the fabrication of solar cells was not part of the workload of this thesis and was performed by colleagues of the author. The author extends gratitude to all contributing team members for their valuable assistance.

Nevertheless, the fabrication methods shall be shortly presented. As already discussed, there are different thin-film deposition techniques that can be divided into two main categories: solution-based methods (such as spin-coating, blade-coating, inkjet printing, etc.) and vapor deposition techniques (including thermal evaporation, PLD, ALD, and sputtering). While the most employed methods for perovskite films are solution-based, in this thesis all layers are deposited using thermal evaporation, with the exception of the passivation materials presented in Chapter 5, which are applied via spin coating. Hence, I provide a brief introduction into these two deposition methods.

**Thermal evaporation** is a thin-film deposition technique, commonly employed in the fabrication of high-performance electronic and optoelectronic devices.[107,108] In this method, the material to be deposited is thermally vaporized from a solid source within a high-vacuum environment, typically at around $10^{-6}$ mbar, to maximize the mean free path that the vaporized atoms can travel without impact with residual gas molecules. This ensures a ballistic trajectory of the atoms from the source to the substrate, promoting uniform and controllable film growth. The evaporation process consists of heating the source material, that is placed in a crucible or a resistive filament, until its vapor pressure is so high that

atoms or molecules move from the surface into the vapor. These vaporized species condense on the colder substrate, forming a thin film. The control of deposition parameters such as evaporation rate, vacuum pressure, and substrate temperature is critical in achieving the desired film thickness, morphology, and crystallinity. Thermal evaporation is widely used for producing high-purity films with minimal defects. However, the technique is limited by the requirement for materials with sufficient vapor pressure at moderate temperatures, as compounds with low thermal stability may degrade before vaporization. Co-evaporation is a variant of the thermal evaporation process, in which multiple materials are simultaneously evaporated from separate sources, allowing for the controlled deposition of multi-component thin films, such as perovskites (Figure 2.1a). Each precursor is heated independently, enabling precise control over the individual evaporation rates, which is critical for achieving the desired stoichiometry and composition in the final film. Yet, the necessity of individual sources for each precursor impedes the complexity of film compositions that can be realized. For perovskite films, several approaches were shown that accomplish the formation of elaborate stoichiometries.[109,110]

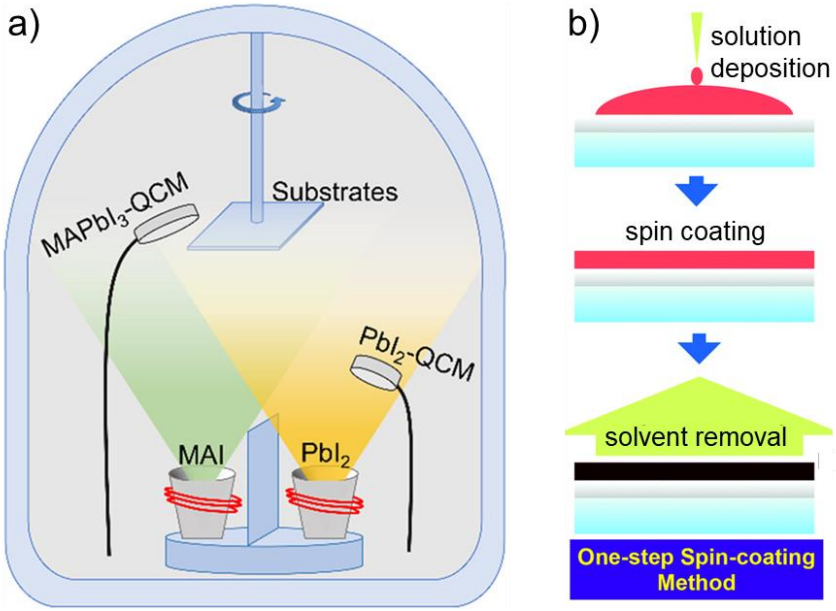


Figure 2.1 a) Schematics of an evaporation chamber to co-evaporate MAI and $PbI_2$ to form $MAPbI_3$. Reproduced from ref [111] (CC BY-NC-ND 4.0). b) Illustration of the spin-coating method. Adjusted with permission from ref [112].

**Spin-coating** creates a thin-film by dropping a solution containing the precursor onto the center of a substrate which is afterwards rotated at high speeds (Figure 2.1b). Due to the rotation, the solution distributes evenly over the substrate and excess material is flung off the edge. The thin-film crystallizes during the evaporation of the solvent, often by placing the substrate on top of a hot plate. The film thickness and uniformity can be adjusted by adjusting the spin speed, spin duration or the concentration of the solution. Spin coating is a simple and cheap technique suitable to produce high-quality thin-films in a small laboratory scale.

Following, I give a step-by-step explanation of the **details of device fabrication** for the employed samples. All processes required to fabricate perovskite solar cells were conducted in a class 10000 cleanroom.

Initially, the ITO-coated glass substrates were cleaned with soap, water, deionized water, and isopropanol using an ultrasonic or sonication bath to ensure thorough removal of contaminants. This was followed by an ultraviolet (UV) or UV-ozone treatment lasting 20 minutes to achieve surface purity.

Then, the samples were transferred into a nitrogen-filled glovebox ($H_2O$ and $O_2 < 0.1$ ppm). Several vacuum chambers were available, each specialized for specific materials to avoid contamination: one for inorganics (molybdenum (VI) oxide ($MoO_3$), Ag, and Au), one for the organic CTLs (N,N,N′,N′-Tetra([1,1′-biphenyl]−4-yl)[1,1′:4′,1″-terphenyl]−4,4″-diamine (TaTm), bathocuproine (BCP), 2,2′,2″-(1,3,5-benzinetriyl)-tris(1-phenyl-1-*H*-benzimidazole (TPBi), and $C_{60}$) and several for the different perovskite compositions. Before deposition, each vacuum chamber was evacuated to a pressure of $10^{-6}$ mbar. The evaporation chamber for the inorganics was equipped with aluminum boats to place the source materials. The other chambers contain several independent temperature-controlled evaporation sources (Creaphys) fitted with ceramic crucibles. The sources were directed upward with an angle of approximately 90° with respect to the bottom of the evaporator. Each source has an individual quartz crystal microbalance (QCM) in its proximity to control the evaporation rate and thickness without cross-reading from other sources. The distance from the substrate holder to the evaporation sources is around 20 cm. For thickness calibration, each layer was individually sublimed, and a calibration factor was obtained by comparing the thickness inferred from the QCM sensors with that measured with a mechanical profilometer (see Chapter 2.2).

For ***p-i-n* solar cells** used in Chapters 3 and 4, on top of the cleaned substrates 5 nm of $MoO_3$ was sublimed by applying a current of 4.8 A to the boat. Afterwards, the $MoO_3$ layer was annealed at 100 ºC inside the glovebox for 10 minutes. The samples were transferred to the evaporator for organic source materials in which 10 nm of TaTm was evaporated at a rate of 0.5 Å $s^{-1}$. It followed the perovskite deposition that is detailed below. Afterwards, 25 nm of the fullerene $C_{60}$ and 7 nm of BCP were evaporated at rates of 0.5 Å $s^{-1}$ and 0.2-0.3 Å $s^{-1}$, respectively. Finally, 100 nm of Ag was deposited as a metal top contact by running a current of 3-4 A through the aluminum boat.

For ***n-i-p* solar cells** used in Chapter 3, a $TiO_2$ dispersion was deposited in air on the cleaned substrates by spin-coating at 3000 rpm for 30 s and annealed at 100 °C for 30 min, leading to a 50–80 nm-thick compact layer. For *n-i-p* solar cells used in Chapter 5, on top of the cleaned substrates a 20 nm layer of $SnO_2$ was deposited by ALD using an Arradiance's GEMStar XT Thermal ALD system integrated into another nitrogen-filled glovebox as detailed in reference [113]. The ALD chamber was heated to 90 °C; one ALD cycle consisted of consecutive purges of tetrakis(diethylamino)tin for 550 ms and water vapor for 200 ms, each followed by $N_2$ purges of 30 and 105 s, respectively (final growth per cycle: 1.5 Å). For all *n-i-p* cells, 12 nm of $C_{60}$ was deposited with a deposition rate of 0.5 Å $s^{-1}$. After the perovskite deposition, 10 nm of TaTm and around 1 nm of TPBi were added at rates of 0.5 Å $s^{-1}$ and 0.2-0.3 Å $s^{-1}$, respectively. To finish the device, 6 nm of MoO3 and either 100 nm of Au (for Chapter 3) or Ag (for Chapter 5) were sublimed.

All devices were encapsulated with $Al_2O_3$ deposited by ALD at 40 °C similar to a protocol prior published, consisting of consecutive purges of trimethylaluminum for 15 ms and water vapor for 150 ms, each followed by $N_2$ purges of 45 and 100 s, respectively.[114]

In Chapter 5, I present additional PL measurements on perovskite films that are directly deposited on a glass substrate. A similar cleaning procedure was applied to the glass substrates as for the ITO coated substrates. Numerous materials were tested as **passivation layers** on top of the perovskite. Different solutions and concentrations were prepared according to previous reports found in literature. For the large ammonium cations (PEAI, BzAI, 4F-BzAI, ChMAI, ChAI), a solution containing ≈10 mg $mL^{-1}$ in isopropanol was used, which was then deposited by spin-coating 100 µL at 4000 rpm. GuaI (3 mg $ml^{-1}$) was deposited at 5000 rpm. A solution of 6 mg $mL^{-1}$ TP6 in toluene was spin-coated at 4000 rpm, while PEO was prepared by dissolving 10 mg $ml^{-1}$ in chlorobenzene and

depositing it via spin-coating at 4000 rpm. Similarly, PMMA was dissolved in chlorobenzene (1 mg $mL^{-1}$) and deposited at 5000 rpm. TOPO was dissolved in hexane (10 mg $mL^{-1}$) and deposited at 2000 rpm. In the case of OPA, 10 mg $ml^{-1}$ solution was prepared in hexane:tbutOH (3:1) and coated at 2000 rpm. All the layers were annealed at 100 °C for 10 min after passivation. The $Al_2O_3$ layer was deposited by ALD as described above.

In this thesis, the data of five different perovskite compositions ($MAPbI_3$, $MAPb(I_yCl_{1-y})_3$, $FA_xMA_{1-x}PbI_3$, $FA_xCs_{1-x}Pb(I_yBr_{1-y})_3$, and $CsPbI_2Br$) is displayed. The first two compositions were deposited in the same vacuum chamber while the remaining three were deposited in a separate chamber.

The **$MAPbI_3$** films in Chapters 3 and 4 were deposited by co-evaporation of MAI and $PbI_2$ precursors simultaneously at the rates of 1.0 and 0.6 Å $s^{-1}$, respectively, measured by two individual sensors and the total perovskite thickness by a third one. In time, the evaporation procedure of this perovskite evolved, rendering a more reproducible fabrication.[111] Therefore, in Chapter 5, the procedure is different. In summary, the evaporation chamber uses only two QCMs, one close to the $PbI_2$ source designated to monitor exclusively the $PbI_2$ precursor ($PbI_2$-QCM), with no cross reading, and a second one fixed at the height of the substrates to monitor simultaneously the total amount of $PbI_2$ and MAI mass reaching the substrates ($MAPbI_3$-QCM). Initially, only $PbI_2$ was heated, and the temperature was fine-tuned to lead to a stable sublimation rate of precisely 0.50 Å $s^{-1}$ on both $PbI_2$-QCM and $MAPbI_3$-QCM. Then, MAI was heated, and the temperature was adjusted so that the sublimation detected on the $MAPbI_3$-QCM increased from the previous 0.50 to 0.66 Å $s^{-1}$, while the rate on the PbI2-QCM was kept stable at 0.50 Å $s^{-1}$. The evaporation was finished when 500 nm of $MAPbI_3$ was deposited (corresponding to ≈4 kÅ on $MAPbI_3$-QCM. The final film contains small amounts of excess $PbI_2$, which helps with the crystallization of the perovskite in the cubic phase.[99,111] In the case of devices containing **$MAPb(I_yCl_{1-y})_3$**, a third thermal source with a corresponding QCM was simultaneously used during the $MAPbI_3$ co-evaporation at an evaporation rate of 0.05 Å $s^{-1}$.

The vacuum chamber for the $FA_xMA_{1-x}PbI_3$, $FA_xCs_{1-x}Pb(I_yBr_{1-y})_3$, and $CsPbI_2Br$ perovskites was equipped with four evaporation sources (Creaphys), each featuring independent temperature controllers and shutters. Each source has an individual QCM sensor, and an additional QCM sensor is installed close to the substrates to measure the

overall deposition rate. All sources were individually calibrated for their respective materials, and cross-reading between different materials is prevented by the strategic positioning of the sources, shutters, and sensors. The base pressure at the beginning of each deposition was $10^{-6}$ mbar. Throughout the deposition process of all perovskites, the chamber pressure was maintained below $8 \times 10^{-6}$ mbar, and the substrates were kept at room temperature. During the **$FA_xMA_{1-x}PbI_3$** perovskite deposition, the individual QCM deposition rates were 1 Å $s^{-1}$ for formamidinium iodide (FAI), 1 Å $s^{-1}$ for $PbI_2$, and the rate for MAI was varied in the range of 0.7–1.9 Å $s^{-1}$ until reaching a film thickness of 500 nm. During the **$FA_{1-n}Cs_nPb(I_{1-x}Br_x)_3$** perovskite deposition, the FAI and $PbI_2$ deposition rates were kept constant at 0.8 Å $s^{-1}$ and 1 Å $s^{-1}$, respectively. In order to tune the bandgap while ensuring phase stability, $PbBr_2$ and CsI were sublimed at varying deposition rates, in the range of 0.25–0.45 Å $s^{-1}$ and 0.07–0.22 Å $s^{-1}$, respectively. The film thickness was 500 nm. Typical sublimation temperatures for the precursors were 150 °C for FAI, 310 °C for $PbI_2$, 280–300 °C for $PbBr_2$, and 490–520 °C for CsI. For the **$CsPbI_2Br$** perovskite, the precursors CsI, CsBr, and PbI2 were co-deposited after calibration of their deposition rates, using 3 sources simultaneously with an overall deposition rate of 2 Å $s^{-1}$, resulting in a total perovskite thickness of 250 nm.

In the following I will list the vendors of the **materials used** in the fabrication process. Photolithographically patterned ITO coated glass substrates were purchased from Naranjo Substrates. TaTm was provided by Novaled GmbH and TCI Europe N.V. Fullerene ($C_{60}$) was purchased from Sigma Aldrich. $PbI_2$, CsBr, $PbBr_2$, and CsI were purchased from Tokyo Chemical Industry CO (TCI). MAI, $MoO_3$ and BCP were purchased from Luminescence Technology Corp. FAI and phenethylammonium iodide (PEAI) was purchased from Greatcell Solar. Guanidinium iodide (GuaI), cyclohexylammonium iodide (ChAI), cyclohexylmethylammonium iodide (ChMAI), benzylammonium iodide (BzAI), 4-fluoro-benzylammonium iodide (4F-BzAI), trioctylphosphine oxide (TOPO), octylphosphonic acid (OPA), polyethylene oxide (PEO), and poly(methyl methacrylate) (PMMA) were purchased from Merck KGaA. All materials were used as received.

## 2.2 Structural analysis

The crystalline structure of the film samples was studied by **X-ray diffraction crystallography** (XRD). By directing X-rays at a sample, XRD measures the angles and

intensities of the diffracted beams, which result from the arrangement of atoms within the crystal lattice. The patterns were collected in Bragg-Brentano geometry on an Empyrean PANalytical powder diffractometer with a copper anode operated at 45 kV and 40 mA.

Cross-sectional and top-view **scanning electron microscopy** (SEM) was used to capture high-resolution images of the perovskite film and the complete device to study the crystal grain size. SEM images were taken with a High-Resolution Field Emission Scanning Electron Microscope (HR-FESEM) ZEISS GeminiSEM 500, with a Secondary Electron In-Lens Detector using an accelerating voltage of 1KV.

The film thicknesses were measured with the **mechanical profilometer** Ambios XP1 by generating thin scratches with a sharp object (e.g. scalpel). The profilometer records the topography of a sample in a line by moving a stylus over the surface while applying a downward force. Therefore, it can detect the film thicknesses by the step height over the scratch.

## 2.3 Optical analysis

### 2.3.1 UV-Vis spectroscopy

UV-Vis spectroscopy measures the wavelength-dependent transmittance and reflectance of films and film stacks. In Chapter 4, the **transmittance** of the glass/ITO/$MoO_3$/TaTm stack is determined to estimate the total current that is generated in the perovskite after optical losses. It was measured by white-light illumination (Avantes AvaLight-DH-S-Bal, deuterium-halogen) that was guided onto the sample surface in a $N_2$-filled glovebox by fiber optics and the transmitted light was collected with fiber optics coupled to a spectrometer (Avantes AvaSpec-ULS2048L). A measurement without a sample was performed to calibrate the transmittance to 100%. In Chapters 3 and 4, I present **reflectance** data of a glass substrate and the complete solar cell to further estimate optical losses. Here, the same light source, fiber optics and spectrometer were used, but the fiber optics were connected to an integrating sphere (Avantes AvaSphere-50-REFL, see Figure 2.2b). The integrating sphere has a hole and is placed on top of the sample, so that only reflected light (both specular and diffuse) is collected and transmitted light is lost. For calibration, a reference tile (Avantes WS-2-Cal) is used that is covered with the same material as the integrating sphere (diffuse PTFE).

### 2.3.2 Photoluminescence

As detailed in Chapter 1.3, the PL can be used as a measure of the radiative recombination and the QFLS inside the perovskite film. A significant part of the work displayed in this thesis involved the development of PL experimental setups, the creation of analysis software, and the execution of PL experiments. Hence, I will present the setups used in Chapters 4 and 5 in greater detail.

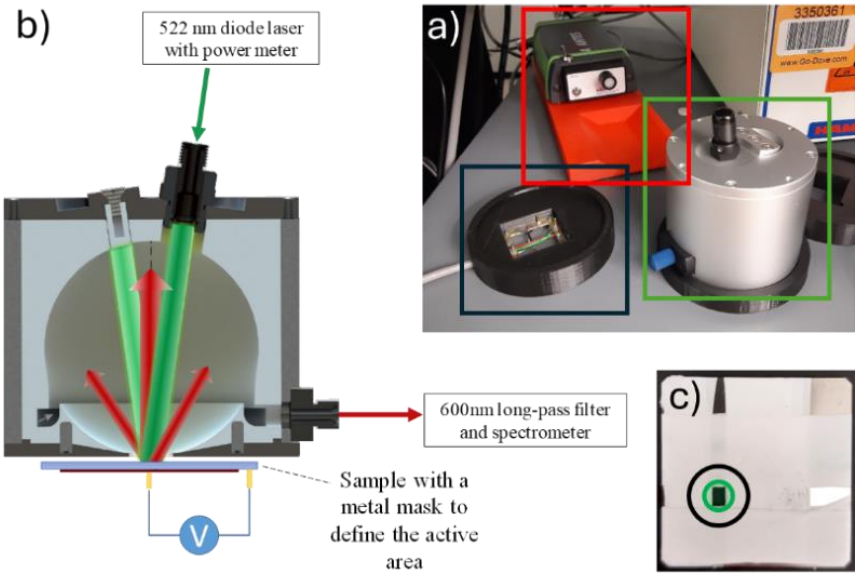


Figure 2.2 Details of the PL setup used in Chapter 4. a) Picture of the employed instruments. Blue box: Custom-built sample holder with electrical contacts. Green box: Integrating sphere. Red box: Calibration lamp. b) Schematic of the setup. Figure of the integrating sphere adapted with permission from ref. [115]. c) Picture of the metal mask wrapped in PTFE tape. The black circle indicates the opening of the integrating sphere. The green circle indicates the spot size of the laser.

**Chapter 4** shows the simultaneous measurement of current and PL under different bias points, also called voltage-dependent PL. In contrast to traditional PL measurements that are always performed under OC conditions, this measurement technique needs electrical contacts for the application of a bias voltage. Therefore, it can only be measured in completed solar cells. To perform the measurement, the cell was placed on a custom-built sample holder (Figure 2.2a) with electrical contacts, connected with 4 wires to a Keithley 2400 source measure unit to approach four-terminal sensing. The cell was covered with a

metal mask with a 0.06 $cm^2$ aperture to define the active area (Figure 2.2b). The mask was wrapped in white reflective PTFE tape around the aperture (Figure 2.2c). An integrating sphere (Avantes AvaSphere-50-REFL) was placed on top of the stack and served for the illumination as well as the collection of the emitted light (Figure 2.2b). The device was illuminated with a diode laser (Integrated Optics 0515L-16A-NI-NT-NF), emitting at 522 nm and connected to the integrating sphere via fiber optics. The spot size on top of the mask was 0.28 $cm^2$, which was reduced on the sample due to the aperture of the mask. The laser power was adjusted to match the current density under simulated AM1.5G illumination. To control the stability of the laser power, 10 % of the light was collected by an optical power meter (Thorlabs PM100D with S140C power head) via a fiber optic coupler with a 90:10 splitting ratio. The integrating sphere was used to collect the light emitted into all directions into the hemisphere in front of the sample homogeneously. The emitted light was collected behind a baffle for homogenization, send through an in-line filter holder (Ocean Optics INLINE-SFH) equipped with a 600 nm long-pass filter to filter the excitation laser and detected by a spectrometer (Avantes AvaSpec-ULS2048L). The system was calibrated spectrally and to absolute photon numbers by a NIST traceable halogen light source (Avantes AvaLight-HAL-CAL-ISP50-MINI) which was placed in front of the sample port of the integrating sphere. This step is crucial to finally calculate the optically emitted current density $J_{rad}$, as described in Chapter 4. A voltage (or current for a $V_{oc}$ measurement) was applied and the PL and current (or voltage) signal were recorded for 40 s per voltage step, with a PL integration time of 5 s, to be able to observe time-dependent effects and to average for noise reduction. A forward scan from 0 V to $V_{oc}$ and a reverse scan from $V_{oc}$ to -0.5 V were acquired in 0.1 V steps, resulting in a scan speed of 0.0025 V $s^{-1}$. Fast JV scans were obtained in a −0.2 to 1.2 V voltage range, with 0.01 V steps and integrating the signal for 20 ms after a 10 ms delay, corresponding to a speed of about 0.3 V $s^{-1}$. In the analysis, the PL peaks were integrated from 1.47 eV to 1.8 eV and the result multiplied by the electric charge to calculate the radiatively-emitted current density $J_{rad}$. The electrical current density $J_{extr}$ was obtained by the mean of the current signal over time.

During the course of this doctoral thesis, the quantitative study of PL (as detailed in Chapter 5) was established as a standard characterization technique across the research group. Therefore, an optical setup was required that could facilitate high-throughput measurements in a rapid, reliable, and quantitative manner. Furthermore, due to the low PLQY of certain films and film stacks (as discussed in Chapter 3 and 5), it was crucial to design a system

capable of efficient light collection. The use of an integrating sphere provided an initial solution; however, it presented significant practical challenges. First, the residues of a multitude of different materials contaminated the sphere requiring tedious cleaning procedures and recalibrations. Second, the in-line filter holder proved cumbersome, as replacing the small long-pass filters was both intricate and time-consuming. Finally and most importantly, the poor collection efficiency of the integrating sphere resulted in long integration times and noisy spectra which increased the uncertainty in derived parameters.

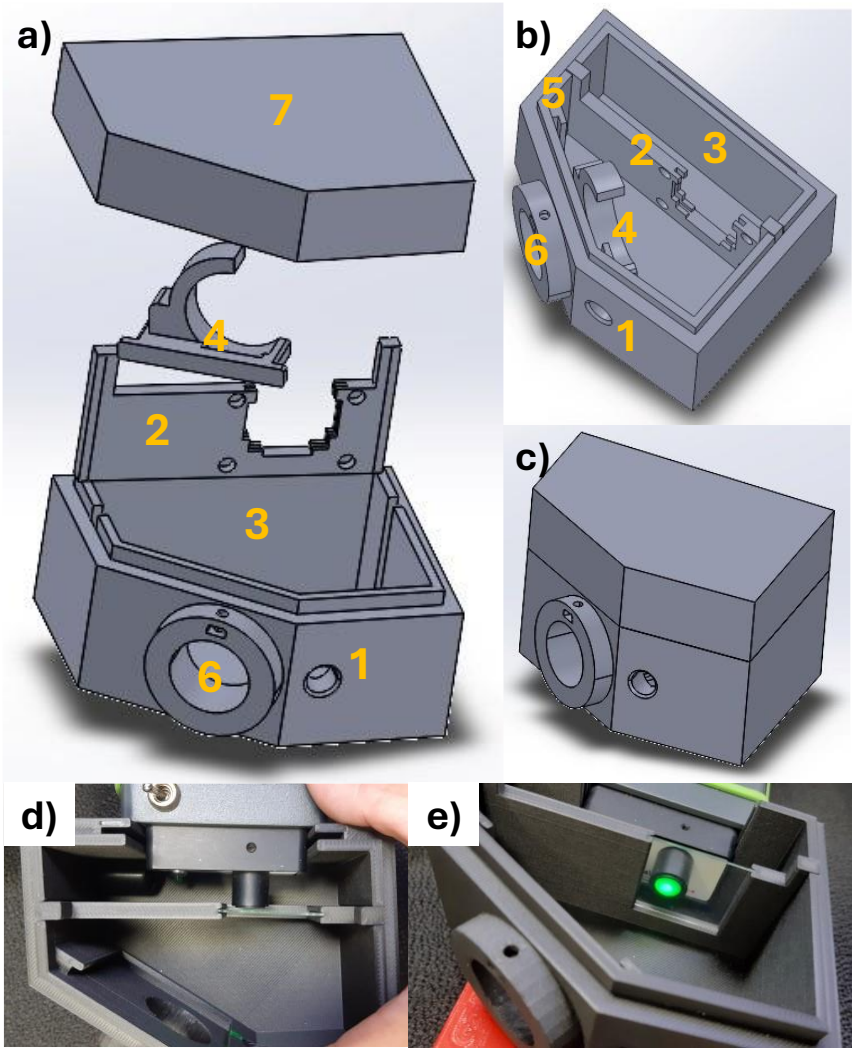


Figure 2.3 Design of the custom-built PL box. 3D-model showing the a) exploded view, b) internal structure, and c) closed exterior. 1: Opening for the excitation collimating lens. 2: Exchangeable sample-holder wall with inlets for magnets to mount the electric connection. 3: Removable back wall to place the calibration lamp. 4: Removable lens clip. 5: Slot for 2"x2" filters. 6: Opening for the collection collimating lens. 7: Top cover. Pictures of the printed box showing the calibration lamp positioned identically to the sample position in d) top-view, and e) front-top-view. The green light stems from the excitation laser.

Therefore, it was part of this thesis to develop a **low-maintenance, efficient and flexible system for PL measurements**. Since the setup was intended for use within a glovebox

environment with many different users, it needed to be compact and robust. I opted not to use a traditional optical breadboard, due to its large footprint and susceptibility to misalignment. Instead, I designed with the help of colleagues a 3D-printed black box that contained all necessary components. The 3D modeling for this enclosure was completed by colleagues who provided invaluable assistance throughout the design phase. In Figure 2.3a-c we see the preparation for the following elements: 1. A collimating lens with fiber port (Avantes COL-UV/VIS) was mounted for coupling the laser out in a quasi-collimated beam onto the sample with a spot size of approximately 0.05 $cm^2$. The spot size was defined by the D4σ method, with an Ophir SP907 beam profiling camera. The power of the lasers was characterized by a Thorlabs PM100D meter with a S121C photodiode sensor. Power densities between 0.4 to 700 mW $cm^{-2}$ could be reached. The beam hits the sample under an angle of approximately 87°, so that the laser light is reflected onto the black wall next to the fiber collimator. 2. A sample-holder wall places the substrate into the intersection of the excitation beam and the focus point of the collection path. For the wall shown in the figure, magnets were glued in the four inlets around the sample slit that serve as holding mechanism for the electrical contacts to be able to perform voltage-dependent PL measurements as in Chapter 4 or also electroluminescence measurements. The wall is exchangeable to accommodate different sample types and sizes. 3. The enclosure contains a removable back wall that provides an opening for the precise positioning of the calibration lamp (Avantes AvaLight-HAL-CAL-ISP50-MINI). Figure 2.3d and e show that the emission surface is placed exactly on the emission spot of the sample. 4. The collection path is oriented at an angle of approximately 58° relative to the sample surface. For an efficient light collection, a 1" lens was incorporated via a replaceable clip in around 35 mm distance to the sample. To maximize the collection of all wavelengths from the largest possible solid angle, I chose an achromatic doublet with a short focal length of $f$ = 50 mm. The purpose of this lens is to collimate the PL, enabling subsequent efficient collection. The focal length is on purpose longer than the distance to the sample, since we want to collect the PL from the illuminated area instead of a focused point. 5. To eliminate the signal from the reflected excitation laser, 2"x2" long-pass filters can be placed into the designated slot. Since various lasers with wavelengths between 375 and 515 nm are frequently used in the research group, the long-pass filters are easily interchangeable or can be removed entirely for electroluminescence measurements. 6. A 1" fiber collimator (Thorlabs F810SMA-780) couples the collimated PL efficiently into the 200 µm-core fiber which is connected to the

spectrometer outside of the glovebox. 7. Finally, a cover is placed on top of the box to block ambient light.

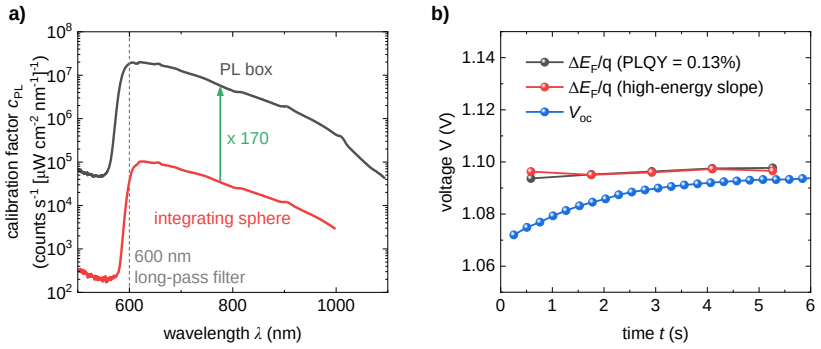


Figure 2.4 a) Calibration spectra of the integrating sphere and the custom-built PL box. b) Comparison of the QFLS, obtained from the PL spectra from the PL box via the high-energy tail and the PLQY method, and the simultaneously electrically measured $V_{oc}$ as a function of time.

The custom-built setup, compared to the integrating sphere, offers greater flexibility as it accommodates different types of samples and allows adjustments through 3D-printing new components. Additionally, the system is less susceptible to contamination, as light is collected directly from the emitting sample. The most significant advantage is an increased collection efficiency of a factor of 170 that can be seen in Figure 2.4a. This improvement factor was tested by comparing the calibration spectra $c_{PL}$ of both setups that are used to calculate the absolute photon flux $\phi_{PL}$ from the counts of the spectrometer $\phi_{spec}$ which are normalized by their integration time $t_{int}$, $\phi_{PL} = \frac{\phi_{spec}}{t_{int}\, c_{PL}}$. The spectra of the calibration lamp $\phi_{spec}$ were acquired by positioning it at the sample location in both setups and collecting the light using a 600 nm long-pass filter. To determine the calibration factor, the integration-time-normalized $\phi_{spec}$ was multiplied by a factor of 4. This adjustment accounts for a discrepancy in data processing, as the Avantes software stores calibration spectra in 14-bit resolution, while sample spectra are recorded in 16-bit resolution. Although this correction is typically automated by the software, it was performed manually in this case to enable the plotting of the calibration spectra. These spectra reflect the spectral response of the entire measurement system, which is predominantly influenced by the spectrometer. The similarity in spectral shape from both systems indicates the absence of a spectral shifts due to the collection setups. The improved collection efficiency results in shorter integration

times, facilitating faster measurements and increasing the signal-to-noise ratio in the spectra.

While the direct collection of light is advantageous in terms of minimizing contamination influence and enhancing collection efficiency, it introduces a significant drawback due to its dependence on the emission profile of the sample. This disadvantage complicates the determination of the absolute photon flux emitted from the sample which is crucial for the QFLS calculation. However, this limitation can be mitigated if the calibration lamp exhibits the same emission profile as the sample. The employed calibration lamp is equipped with a cosine corrector to generate a Lambertian emission profile. In the application of the setup, we need to assume that the samples, which consist of a film stack on a glass substrate, also exhibit a Lambertian profile. This assumption holds true for most cases where no elaborate light outcoupling scheme is employed, e.g. if a strong optical cavity influences the light direction in the film stack.[116–118] It should be noted however, that for samples in powder form, that emit isotropically, the performed calibration is not valid. To assess the validity in the used samples, I compared the QFLS of a solar cell, derived from the calibrated PL spectrum, with the $V_{oc}$ measured simultaneously via electrical contacts. Under OC conditions, the external voltage is generally equal to the internal voltage, providing a means to verify the calibration.[119,120] I measured the PL and $V_{oc}$ of a *p-i-n* $MAPbI_3$ solar cell, illuminated with a green laser (Integrated Optics 0515L-16A-NI-NT-NF) at the power density matching the $J_{sc}$ under AM1.5G illumination ($P_d$ = 61 mW $cm^{-2}$ for a 515 nm laser). The QFLS $\Delta E_F$ was calculated from the calibrated PL spectrum following the methods of fitting the high-energy tail (as used in Chapter 4) and by integrating the spectrum to calculate the PLQY (as used in Chapter 5), that were discussed in Chapter 1.3. In Figure 2.4b), the QFLS from both methods is plotted together with the measured $V_{oc}$ over a time of six seconds. The QFLS is stable at $\Delta E_F$ = 1.096 eV. Although both determination methods yield similar results for clean spectra with low noise as demonstrated here, experience has shown that the PLQY method provides more reliable outcomes, especially for samples with very low PLQY. The open-circuit voltage starts from $V_{oc}$ = 1.072 V and saturates around $V_{oc}$ = 1.094 V. The increase in the beginning is most likely explainable with a re-orientation of ions that leads to a better band alignment.[119,121,122] The difference between $\Delta E_F$ and saturated $V_{oc}$ is with 2 meV small enough to confirm that the calibration of the optical setup works. In general, I attribute an uncertainty of ± 10 meV to the QFLS

determination due to uncertainties of the calibration and local inhomogeneities of the samples (compare with Figure 5.1e).

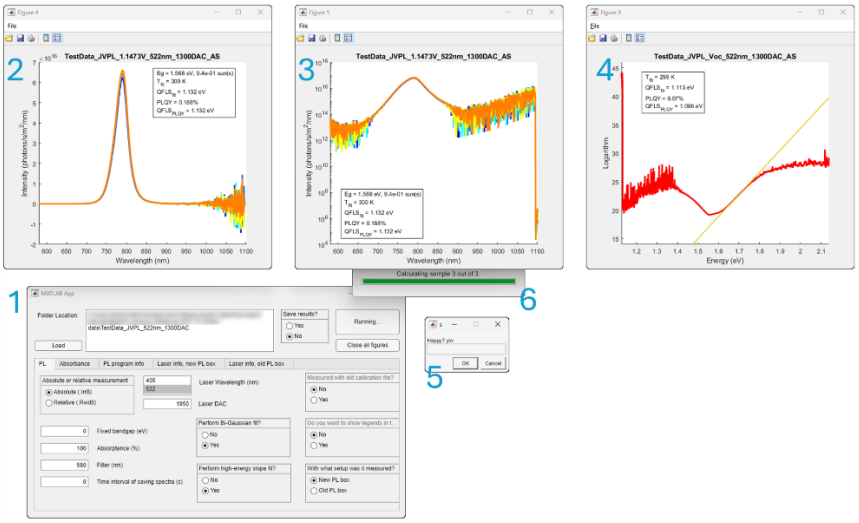


Figure 2.5 Screenshot of the stand-alone software *Avantes_PL_and_Abs_analysis* during execution, cycling over three measurements (stopped in the third iteration). 1: Main program with settings. 2 and 3: Time series of PL spectra of the previous iteration in linear and semilogarithmic scale, respectively. The laser settings are included in the folder name (which is shown as title of the figures) for automatic extraction. The extracted parameters are shown in the box. 4: Time series of the logarithm of the parameters defined in Equation (1.34) of the current iteration together with the fit of the high-energy tail and extracted parameters. 5: The program asks the users whether they are content with the fit. Otherwise, they can define new energy bounds for fitting. 6: Progress bar of the program indicating the current iteration.

Furthermore, a **stand-alone software** for the analysis of optical data (Avantes_PL_and_Abs_analysis.exe) was developed using MATLAB. The program is user-friendly, requiring neither MATLAB nor programming expertise, although the MATLAB source code is available for any necessary adjustments. While it is possible to extract the bandgaps from UV-Vis measurements automatically and compare their absorbance and Tauc plot, the main function of the program is to calculate the PLQY and QFLS of calibrated PL measurements.

Users can select a main directory containing either the raw data files or subdirectories with individual data sets. The software treats all files within a single folder as a time series representing a single sample; consequently, each folder should contain data specific to one

sample under fixed experimental settings. Measurement details such as laser wavelength, laser power, setup configuration, and sample temperature are automatically parsed from the (sub-)folder names.

The program systematically reads in the files, extracting from them the wavelengths and the spectra in both units: counts from the spectrometer (scope mode) and the absolute photon flux (absolute irradiance mode). First, it applies corrections for potentially incorrect calibration files, ensuring data accuracy. Next, it corrects the spectra for the laser spot size and converts the units to $nm^{-1}s^{-1}m^{-2}$. For samples without metal back electrode, the intensity is multiplied by a factor of 2 to adjust for the light escaping through the back. The software also extracts the integration time and the number of averaged spectra during the measurements. After that, it calculates the elapsed time since the start of the measurement for each spectrum, enabling temporal analysis of the data. Finally, the program displays all spectra in time in both linear and logarithmic scales and opens an interactive window for defining integration boundaries to determine the emitted photon flux. An included algorithm detects if the laser was turned on or off in the beginning or end of the measurements and excludes such data from further analysis.

The graphical user interface (GUI) offers the option for a bi-Gaussian fit, that was initially intended to quantify halide segregation in mixed-halide perovskite films. While this analysis was found ineffective, it is valuable for accurately determining the peak PL signal. Given that perovskites exhibit negligible Stokes shift, the bandgap is derived from this peak. The determined bandgap can be subsequently used to calculate the sun-equivalent power density and the radiative limit of $V_{oc}$, unless a fixed bandgap value is provided in the GUI.

The software then calculates the PLQY by determining the ratio of the integrated emitted photon count to the excitation photon count, which is itself derived from the laser power density, photon energy, and the absorptance of the perovskite film at the excitation wavelength. The QFLS is calculated via Equation (1.36).

If the QFLS should additionally be determined via the high-energy tail fit (which can be defined in the GUI), the program plots the logarithm (Equation (1.34)) versus energy and asks interactively for the boundaries in which it should find a linear fit. It automatically searches for a fit that returns a temperature closest to 300 K by looping over the designated fitting range, as this provides the most reliable results. Afterward, it shows the fit to the user

and prompts them to confirm if they are content with the fit; if not, they can choose a new fitting range.

Both the QFLS values, obtained from the PLQY and from the high-energy tail fit, are plotted versus time. All results, including spectra plots and data, bi-Gaussian fit data, and overview files containing extracted parameters (i.e., time, photon counts, PLQY, QFLS, temperature and QFLS from the high-energy tail fit, extracted bandgap, laser intensity in equivalent suns) are saved automatically.

After processing all subfolders, the software generates overview plots summarizing key extracted parameters as a function of time of all measurement sets. For each set, it determines the measurement with maximum PLQY value and generates a CSV file containing the parameters of this measurement. Additionally, comparison plots of the corresponding spectra are produced in linear, logarithmic, and normalized logarithmic scales.

As an example, I want to show the analysis of the $MAPbI_3$ film from **Chapter 5**, which spectrum and PLQY are shown in Figure 5.1c and d, respectively. The PL peak was integrated numerically from 650 to 900 nm and yielded a total emitted photon number of $\phi_{PL} = 1.89 \times 10^{18}$ $s^{-1}m^{-2}$. This needs to be put in relation to the excitation photon density of $\phi_{abs} = 610$ $Wm^{-2} \times (6.24 \times 10^{18}$ $eC^{-1}) \times (2.4$ $eV)^{-1} = 1.60 \times 10^{21}$ $s^{-1}m^{-2}$ and an absorptance of 80% at 522 nm to yield an external PLQY of 0.15%. In Chapter 5, the radiative limit of the open-circuit voltage was not extracted from the SQ limit, as the software typically does, but it was calculated from EQE measurements via Equation (1.5), as detailed in Chapter 3, with $J_{sc} = 20.9$ mA $cm^{-2}$ and $J_{0,rad} = 1.1 \times 10^{-21}$ mA $cm^{-2}$ (see also Figure 5.6d) to give $V_{oc,rad} = 1.324$ V. Following Equation (1.36), the estimated QFLS reads $\Delta E_F = 1.324$ eV + 0.0258 eV ln(0.0015) = 1.156 eV.

### 2.3.3 Time-resolved photoluminescence

As detailed already in Chapter 1.3, **TRPL** can provide valuable information about recombination processes by disentangling their scaling in time. In Chapter 5, it was used to estimate surface recombination on bare perovskite films on glass.

TRPL was measured by the group of Fréderic Laquai at King Abdullah University of Science and Technology (KAUST). The measurements were carried out using an Innolas

piccolo MOPA Laser with a pulse duration of 1 nanosecond and repetition rate of 50 kHz. The samples were excited at 532 nm at moderate fluences of 8, 37 and 147 nJ $cm^{-2}$. The PL of the samples was collected by an optical telescope (consisting of two plano-convex lenses), and it was further focused on the slit of a spectrograph (PI Spectra Pro SP2300), and eventually detected with a Streak Camera (Hamamatsu C10910) system with a temporal resolution of 1.4 picosecond (ps). All samples were kept in a nitrogen-filled chamber and measured at room temperature. The data was acquired in photon counting mode using the Streak Camera software (HPDTA) and was sent to Valencia. Here, the author exported the data to Origin Pro 2020 for further analysis. The spectra at each time delay were integrated over a small wavelength region from 746 to 803 nm (120 points). This region was chosen to maximize the signal-to-noise ratio by averaging out the noise in the signal but also keeping it small enough to not integrate over noise in weak spectra at long decay times. The obtained intensities were plotted against the delay time where the maximum was set at the time 0 and normalized to 1. Then the logarithm of the intensity $\phi$ was fitted with a 4$^{th}$ degree rational function $\left(y = \frac{ax^4+bx^3+cx^2+dx+e}{x^4+fx^3+gx^2+hx+i}\right)$. The purpose of the 4$^{th}$ degree rational function was solely to follow the shape of the decay accurately and avoid measurement noise. This was necessary because the effective decay time $\tau_{eff} = -2(d\ln(\phi)/dt)^{-1}$ depends on the derivative of the intensity, which amplifies noise in the presence of already noisy data.[123] Finally, the QFLS was calculated from the intensity. The maximum value of the QFLS directly at time 0 was calculated by the measured absorbed laser fluence. From the fluence and the perovskite thickness, the absorbed photon density and subsequently the average charge-carrier density per volume $n$ was calculated. It was assumed that the sample was in high-level injection at early times ($n = p$) and the QFLS $\Delta E_F$ was calculated from $\Delta E_F = kT \ln\left(\frac{n^2}{n_i^2}\right)$ where $n_i = 8.05 \times 10^4$ $cm^{-3}$ is the intrinsic charge-carrier density in the $MAPbI_3$ perovskite.[124] Then the fact was used that there was always an exponential relation between the quasi-Fermi-level splitting and the PL flux ϕ, which allows to write $\phi \propto \exp\left(\frac{q\Delta E_F}{kT}\right)$. This determines the QFLS at later times.

## 2.4 Optoelectronic analysis

**Current-voltage (*JV*) curves** were used to extract the PCE as well as the parameters $J_{sc}$, $V_{oc}$, and *FF* to get a first insight of the governing loss mechanisms in the investigated solar cell as detailed in Chapter 1.2. The *JV* curves under simulated AM1.5G illumination were recorded using a Keithley 2612A SourceMeter in a -0.2 and 1.2 V voltage range, with 0.01 V steps and integrating the signal for 20 ms after a 10 ms delay, corresponding to a scan speed of about 0.3 V $s^{-1}$. The device was illuminated under a Wavelabs Sinus 70 LED solar simulator. The light intensity was calibrated before every measurement using a calibrated Si reference diode equipped with an infrared cutoff filter (KG-3, Schott). Intensity-dependent $V_{oc}$ measurements (Suns-$V_{oc}$) were obtained by placing neutral density filters, whose transmission was measured, in front of the sample. The layout used to test the solar cell has 4 equal areas (0.0651 $cm^2$, defined as the overlap between the ITO and the top metal contact) and measured through a shadow mask with 0.06 $cm^2$ aperture.

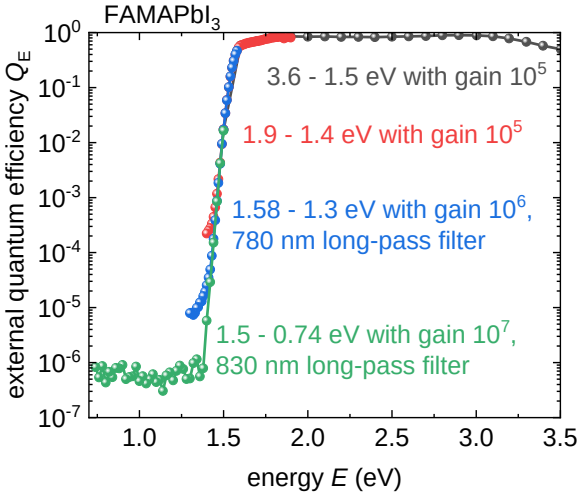


Figure 2.6 Overlay of EQE measurements with different ranges, gain settings and long-pass filters. To obtain the overall EQE spectrum, the single measurements are stitched together.

The **external quantum efficiency (EQE)** gives wavelength-dependent information about the loss of the short-circuit current. Additionally, its tail at energies below the bandgap affects the dark saturation current and therefore the $V_{oc}$ in the radiative limit. As this tail

decays exponentially, one needs to be able to detect it over a large order of magnitude. In Chapter 3, I present and discuss sensitively measured EQE spectra of various co-evaporated perovskite solar cells. For the sensitive EQE measurements, the light source was a Quartz-Tungsten-Halogen lamp (Newport Apex 2-QTH). The light was filtered first roughly through a filter wheel to exclude wavelengths from higher-order diffractions and afterwards through a monochromator (Newport CS130-USB-3-MC) with around 7 nm bandwidth. The nearly monochromatic light went through an optical chopper which was driven at 271 Hz and the device current was measured with a current-to-voltage amplifier connected to a lock-in amplifier (Stanford Research Systems SR830). The use of the lock-in amplifier allows to exclude currents with a different frequency than the one of the chopper wheel which increases the signal-to-noise ratio. The chopper frequency was set on purpose far away from multiples of 50 and 60 Hz to rule out any influence from surrounding electrical equipment and room lights. To calibrate the system, two calibrated photodiodes were used with known EQE spectrum. The Si photodiode (Thorlabs FDS100-CAL) could be used for photon energies between 1.13 and 3.54 eV, the Ge photodiode (Thorlabs FDG03-CAL) between 0.73 and 1.55 eV. For each EQE measurement, a new calibration measurement was performed where the calibration diodes were placed at the sample position to adjust for potentially changed parameters (temperature, intensity of the lamp, room light, etc.). The stability of the lamp was checked by a calibration measurement in the end of the sample measurement. The two calibration measurements were always identical and ensured the stability of the light source for several hours.

As part of the thesis, the setup was slightly modified to improve the sensibility and achieve absolute EQE measurements. This was realized by placing two lenses ($f$ = 75 mm and $f$ =50 mm) after the optical chopper: the first one to collimate the light as well as possible and the second to focus it down. The beam spot at the focus point was smaller than the active area of both the reference cell and the solar cell under test, making an absolute measurement possible. Furthermore, the decreased spot size increased the power density and hence the current density measured by the device which increased the signal-to-noise ratio additionally.

To measure the broad absorption region, the setup was calibrated with the Si photodiode and the device current was determined as a function of energy from 3.5 to 1.5 eV in 0.07 eV steps with a gain of $10^5$, averaging over 10 measurements with a time constant of the low-pass filter of 0.3 s (see black curve in Figure 2.6). For the sensitive measurements in the

bandgap region, several measurements were necessary. The first one used the same settings as the broad measurement, but in a decreased range around the bandgap (e.g. for FAMAPbI$_3$ solar cells with Eg = 1.56 eV from 1.9 to 1.4 eV) with a reduced step size of 0.02 eV to resolve the absorption edge well and an increased time constant of 1 s to increase the signal-to-noise ratio (see red curve in Figure 2.6). These settings led to a dynamic range of 3 orders of magnitude and were kept for the following measurements. For the second measurement, an optical long-pass filter was placed in the beam in front of the sample to block light with energies above the bandgap (e.g. for FAMAPbI$_3$ solar cells a RG780 filter) that might pass the monochromator by scattering or higher-order diffractions (see blue curve in Figure 2.6). Even with weak intensity, this light leads to a considerable background current as the absorption coefficient of the perovskite is larger at these energies. Filtering these wavelengths increased the signal-to-noise ratio. The EQE was measured from the cut-off energy of the long-pass filter to about 1.3 eV, using the Si photodiode for the calibration as before. Since the currents in this region were lower, the gain was increased to $10^6$, leading to a higher sensitivity of the setup. These settings allowed for EQE measurements down to $10^{-5}$. In a final measurement, the entire range of the Ge photodiode was used, employing a RG830 long-pass filter to block any potential stray light (see green curve in Figure 2.6). The gain was further increased to $10^7$, enabling highly sensitive EQE measurement with a noise floor of $10^{-7}$ – $10^{-6}$. In the end, all these measurements were stitched together to form one extensive EQE spectrum.

## 2.5 Drift-Diffusion Simulation

In Chapter 5, device simulations were performed using **SIMsalabim** (Version 3.77), an open-source drift-diffusion simulator for semiconductor devices, a software developed by Jan-Anton Koster et al.[125] The code can be obtained for free from https://github.com/kostergroup/SIMsalabim.

The drift-diffusion simulator solves the continuity equations including recombination, drift, diffusion and charge transfer between layers in the lateral device dimensions by input parameters such as the energy levels, permittivity, mobilities, and thickness of the layers as well as trap states or applied voltages. In this thesis, SIMsalabim was used to fit implied pseudo-*JV* curves that were estimated via PL and *JV* measurements at different light intensities. These curves were associated with progressively expanded theoretical limits,

each including more loss mechanisms, starting from the inner layers and moving to the outer layers, which together formed one conclusive device model. With the obtained model as basis, the simulation software was used to generate predictions for potential device improvements, offering insights into optimization strategies.

# 3 Efficiency Loss Origins in JV Parameters

As discussed in the introduction, the *JV* curve is the basic characterization method for solar cells. The curve gives direct access to the PCE, but the parameters $V_{oc}$, $J_{sc}$, and *FF* also enable a first distinction between different loss mechanisms, when compared to their theoretical limits. Therefore, this chapter will examine a multitude of solar cell structures with different perovskite compositions all fabricated using co-evaporation to quantify the loss mechanisms in the solar cells and to find common trends.

## 3.1 Introduction

To gain an accurate understanding of the losses, it is essential to establish the upper limits of the *JV* parameters. So far, the theoretical limits have been discussed in relation to the SQ limit. Shockley and Queisser assumed in their thermodynamic calculations a perfect semiconductor with a step-function absorption onset and only radiative recombination.[27] However, every solar cell architecture for a specific material has certain limitations that it cannot overcome, even in theory. In the context of solar cell optimization, it is instructive to determine the PCE limit given these material constraints. For Si solar cells for example, the limiting efficiency was calculated to be 29.8% when considering a planar structure with Auger recombination, free-carrier absorption, and additional radiative losses - in comparison to the SQ limit of 32.3%.[59] While the loss due to free carrier absorption is insignificant, Auger recombination leads to a considerable decrease in PCE in Si solar cells. The additional radiative recombination compared to the SQ limit is caused by an imperfect absorption onset due to localized states close to the band edge, the so-called Urbach tail. The Urbach tail decays exponentially into the bandgap and is characterized by a defining parameter, the Urbach energy $E_U$.[126] A high Urbach energy can result from structural and thermal effects, such as polycrystallinity or local deviations from stoichiometry.[54,57,127] The additional absorption due to the tail has little effect on the $J_{sc}$ but it can increase $J_{0,rad}$ significantly and has therefore a negative impact on the $V_{oc}$. The band tail leads to a PCE

decrease of about 1% absolute in Si solar cells. In other solar cell technologies this loss is even larger.[128–130] Given that perovskites encompass a wide range of materials with varying structural quality influenced by compositional changes and crystallization methods, it is valuable to investigate the behavior of co-evaporated perovskite based solar cells.[57,131]

Experimentally, the Urbach tail can be accessed with either optical excitation - such as photothermal deflection spectroscopy (PDS),[52,57] Fourier-transform photocurrent spectroscopy (FTPS),[52,130] and EQE[57,132] - or entirely electrical characterization - such as charge extraction[133] and admittance measurements.[134] Electrical measurements probe the density of states also deep in the bandgap with a high sensitivity but they can suffer from an overestimation of the Urbach energy due to internal series resistances.[135] For the estimation of the voltage loss caused by additional radiative recombination, the part of the band tail close to the bandgap is the most important, as here the product of $\phi_{BB}(300\ K)\times Q_E^{PV}$ (= the EL spectrum at 0 V) forms its maximum.

Here, to avoid the risk of overestimating $E_U$, I study the absorption tail by high-dynamic range EQE measurements. This optoelectronic method allows for a sensitive assessment of the band tail to estimate the Urbach energy precisely and gives additionally spectral information to resolve potential trap states or charge transfer states.[130,136–138] I measure the EQE of a large number of devices with different perovskite compositions covering a range of bandgaps. For each sample, I extract the bandgap and Urbach energy and decompose the $V_{oc}$ losses into short-circuit, radiative, and non-radiative losses. By analyzing the relationship between these parameters, we observe that non-radiative voltage losses increase with the bandgap as seen before.[139,140] A weak correlation between the Urbach energy and bandgap is also noted, but due to the consistently low Urbach energies of the samples, radiative losses are minimal. Instead, non-radiative losses dominate, showing no strong dependence on the Urbach tail. To better understand efficiency losses, I determine the *JV* parameters $V_{oc}$, $J_{sc}$, and *FF* relative to their radiative limits and find that all three parameters contribute equally to the performance losses across the different compositions. I quantify the reflective losses and calculate the IQE, identifying contributions from collection inefficiencies and/or parasitic absorption. By examining the relationship between $J_{sc}$ and *FF* losses, considering the effects of optical losses and electrical losses from shunt and series resistances, I conclude that the observed losses are primarily influenced by electrical losses associated with recombination.

## 3.2 Results and Discussion

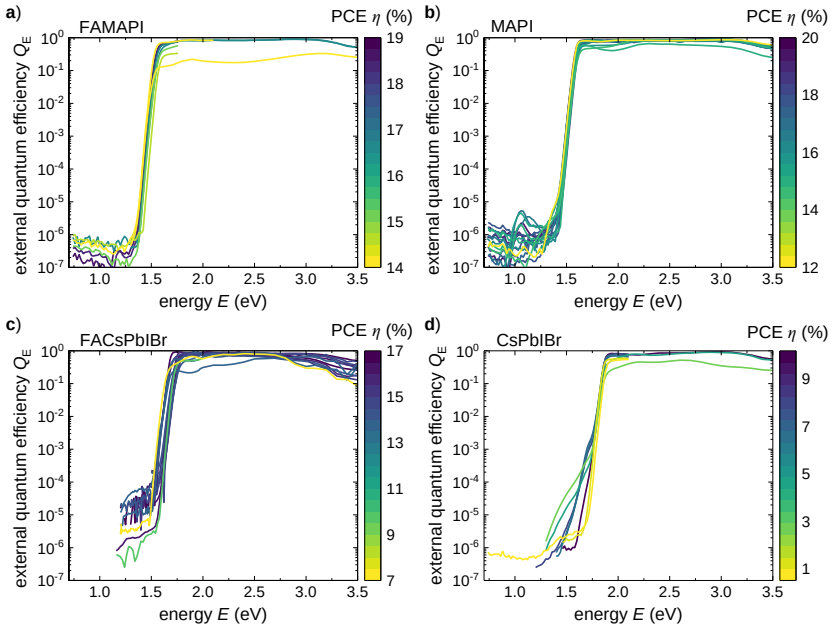


Figure 3.1 Collection of all measured EQE curves in semilogarithmic scale for specific perovskite compositions: a) FAMAPI, b) MAPI, c) FACsPbIBr, and d) CsPbIBr. The color of the lines encodes the power conversion efficiency.

I measured sensitive EQE on a multitude of samples employing four different principal perovskite compositions, all fabricated by co-evaporation in the MOED research group. The samples might vary in the choice of charge CTLs, the configuration (*n-i-p* vs *p-i-n*) and the thickness of the perovskite layer. Some of the EQE spectra have been published to help discussing the optimization of the specific technology.[109,141–143] Figure 3.1 shows all the sensitively measured EQE spectra for each composition. The figures are plotted in semilogarithmic scale to display the detectable dynamic range of the band tail. The spectra were recorded partly over the whole measurement range (max 3.5 eV), partly just in the bandgap region. It was chosen to plot them in groups to show the reproducibility for the specific perovskite compositions. While $MAPbI_3$ (MAPI) (Figure 3.1b) and $CsPbI_2Br$ (CsPbIBr) (Figure 3.1d) are aimed for the same composition every time and just vary due to fabrication variations and optimizations, in $FA_xMA_{1-x}PbI_3$ (FAMAPI) (Figure 3.1) and

$FA_xCs_{1-x}Pb(I_yBr_{1-y})_3$ (FACsPbIBr) (Figure 3.1c) the stoichiometries are varied to obtain different bandgaps and optimize the performance. The color of the lines indicates the PCE as illustrated by the color bar on the side. I will discuss the general shape of the curves on the example of the lowest bandgap material (FAMAPI, Figure 3.1a).

At high energies down to the bandgap around 1.55 eV, the light is absorbed well and the EQE response is close to 1. This region determines the $J_{sc}$. Some samples show lower EQEs across the whole spectrum which corresponds to a low $J_{sc}$ and therefore directly to a lower PCE as indicated by the colors.

At energies below the bandgap, the EQE decays exponentially until it reaches the noise level of $10^{-7}$-$10^{-6}$ at around 1.35 eV. The noise level changes most likely due to the dark current of the sample and temperature fluctuations between the days of measurement.[144] The noise floor for some samples of FACsPbIBr is higher ($10^{-5}$ - $10^{-4}$) because these were measured before the EQE setup was optimized. The region of exponential decay is our main interest for the determination of $V_{oc,rad}$. This region is comparably homogenous for FAMAPI and MAPI (Figure 3.1a and b) but varies more for the wide-bandgap perovskites FACsPbIBr and CsPbIBr (Figure 3.1c and d).

CsPbIBr is special in the sense that all samples show similar behavior in the EQE range from $5\times10^{-3}$ to $10^{-1}$ but at lower values some diverge and show an increased EQE response. Multiple effects can cause such a feature, for instance optically active defect states or optical excitation between different materials.[136,138] Two devices do not show this feature (the yellow lines in Figure 3.1d). These two devices are the only ones of the CsPbIBr cells in *n-i-p* configuration and use SnO2 as ETL instead of $C_{60}$. This suggests an involvement of $C_{60}$ in the origin of the increased EQE response. It was found that there is a significant energy offset between the conduction band of CsPbIBr and $C_{60}$.[145] This band misalignment could potentially lead to the excitation of a charge-transfer state, where an electron from the valence band of CsPbIBr is excited into the conduction band of $C_{60}$.[136,145] This absorption adds little to the observed current, but it leads to more radiative and potentially non-radiative recombination.

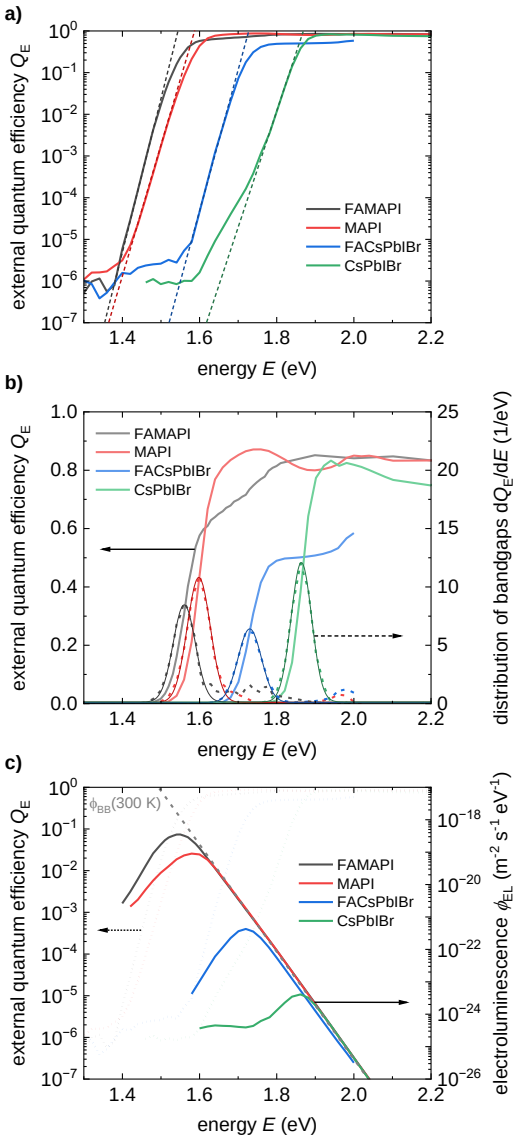


Figure 3.2 a) Demonstration of the fit of $E_U$ (dashed lines) on the tail region of the EQE in semilogarithmic scale. b) Extraction of the bandgap $E_g$ via the derivative $dQ_E^{PV}/dE$, which can be interpreted as a distribution of SQ bandgaps. The maximum of the peak fit is used for $E_g$. c) Calculation of the electroluminescence spectra (solid lines) in the dark without bias from the EQE spectra (dotted lines) and the black-body spectrum (dashed line) used for the determination of $V_{oc,rad}$. All plots contain a representant of each of the 4 different perovskite compositions.

For the other three perovskite compositions, certain spectra exhibit peaks that emerge out of the noise region. The origin of these peaks is most likely a combination of defect states and optical interference due to layer thicknesses.[138] Since these features were not reproducibly detectable, they could not be investigated in further detail, but they indicate an additional recombination pathway.

To be able to quantify the discussed features I extract the Urbach tail $E_U$, the bandgap $E_g$, and the radiative limit of the open-circuit voltage $V_{oc,rad}$ from the EQE spectra. Figure 3.2 illustrates how these parameters are determined. To calculate $E_U$, I fit the exponential function $\exp(E/E_U)$ to the tail region of the EQE (Figure 3.2a). The fit describes the EQE tail well until it reaches the noise level for FAMAPI, MAPI, and FACsPbIBr. For CsPbIBr, only the region unaffected by the enhanced absorption feature is fitted.

Now I discuss the extraction of the bandgap value via the EQE. Assuming a SQ-like EQE with a step function at the bandgap value, the latter can be recognized easily in the derivative $dQ_E^{PV}/dE$ on the delta-function-like peak at $E_g$. Taking the derivative of a measured spectrum gives a broader peak (Figure 3.2b). This peak can therefore be interpreted as a distribution of SQ bandgaps.[128] Due to the symmetry of the peaks, I use the peak maximum as the definition of the bandgap. This corresponds to the steepest point on the EQE curve.

Finally, the radiative limit of the $V_{oc}$ is extracted from the measured short-circuit current density $J_{sc}$ and the radiative limit of the dark saturation current density $J_{0,rad}$ according to Equation (1.5). Following Equation (1.2), $J_{0,rad}$ can be found via the integral of the electroluminescence (EL) spectrum, obtained from the product of the black-body spectrum and the EQE, where especially the energy region around and below the bandgap is crucial. Figure 3.2c illustrates this calculation of the EL spectrum on the example of the four perovskite compositions. The EL is drawn until the EQE reaches the noise level. We can see that the high-energy part of the EL spectrum follows the black-body spectrum because of the relatively flat EQE close to 1; only for the chosen example of FACsPbIBr it lays below, as the EQE is limited to 0.5 in the observable energy range (compare Figure 3.2b). The peak maximum and the low-energy part of the EL depend strongly on the band tail of the EQE. For CsPbIBr, the increased EQE response at energies below 1.75 eV (in comparison to the expected behavior according to $E_U$) leads to a constant EL response. The

overlap of the bandgap (from Figure 3.2b) with the peak of the EL indicates small radiative voltage losses as we will also see in the following.[128]

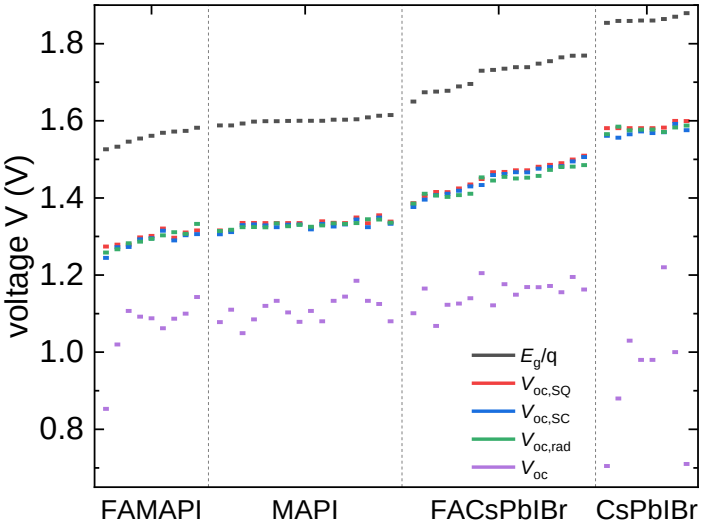


Figure 3.3 Open-circuit voltage limitations under a 1-sun equivalent illumination. The extracted bandgap divided by the elementary charge, the SQ limit of the $V_{oc}$, the short-circuit limit, the radiative limit and the experimentally measured $V_{oc}$ are illustrated.

The losses of the measured $V_{oc}$ can be understood better by splitting them up into their origin. As already discussed, one important distinction comes from the separation of the radiative limit and the non-radiative losses $\Delta V_{oc,non\text{-}rad}$,

$$V_{oc} = \frac{kT}{q}\ln\left(\frac{J_{sc}}{J_0}\right) = \frac{kT}{q}\ln\left(\frac{J_{sc}}{J_{0,rad}}\right) + \frac{kT}{q}\ln\left(\frac{J_{0,rad}}{J_0}\right) = V_{oc,rad} - \Delta V_{oc,non-rad}. \quad (3.1)$$

The origin of $\Delta V_{oc,non\text{-}rad}$ is discussed in Chapter 5. But also the radiative limit can be split up into different contributions,

$$V_{\mathrm{oc,rad}} = \frac{kT}{q}\ln\left(\frac{J_{\mathrm{sc}}}{J_{0,\mathrm{rad}}}\right) = \frac{kT}{q}\ln\left(\frac{J_{\mathrm{sc,SQ}}}{J_{0,\mathrm{SQ}}} \times \frac{J_{\mathrm{sc}}}{J_{\mathrm{sc,SQ}}} \times \frac{J_{0,\mathrm{SQ}}}{J_{0,\mathrm{rad}}}\right) = V_{\mathrm{oc,SQ}} - \Delta V_{\mathrm{oc,sc}} - \Delta V_{\mathrm{oc,rad}}. \quad (3.2)$$

$V_{\mathrm{oc,SQ}}$ is the $V_{\mathrm{oc}}$ of the SQ limit as discussed in Chapter 1.2. $\Delta V_{\mathrm{oc,sc}}$ corresponds to the $V_{\mathrm{oc}}$ losses due to a lower $J_{\mathrm{sc}}$ than in the SQ limit, which leads to the limit $V_{\mathrm{oc,SQ}}$, and $\Delta V_{\mathrm{oc,rad}}$ refers to the change in $V_{\mathrm{oc}}$ that follows from a different radiative recombination given by the non-ideal light absorption.

Figure 3.3 shows the measured $V_{\mathrm{oc}}$, the limits $V_{\mathrm{oc,SQ}}$, $V_{\mathrm{oc,sc}}$, $V_{\mathrm{oc,rad}}$, as well as the bandgap, expressed as a voltage, of all measured solar cells, ordered per their bandgap energy. The bandgaps of the perovskites aimed for fixed stoichiometry exhibit minor fluctuations with a total amplitude of 0.025 eV around their respective average values of 1.601 eV and 1.863 eV, indicating the reproducibility of the fabrication process and the precision of the measurement technique. Apart from variations of the stoichiometry, the optical extraction of the bandgap is sensitive to the film thickness, optical effects, stress or strain within the material, crystallinity, and the resolution of measurement equipment. On the other hand, the $E_{\mathrm{g}}$ values for the other two perovskites display a broader range of bandgaps due to targeted compositional differences.

$V_{\mathrm{oc,SQ}}$ is in theory only dependent on the bandgap. However, I derived it by numerically integrating the corresponding spectra for energies above the bandgap using the energy spacing of the EQE measurements. As this might be different between measurements, $V_{\mathrm{oc,SQ}}$ may vary for a given bandgap slightly. This approach was chosen to align it with $V_{\mathrm{oc,rad}}$ for comparison purposes. $V_{\mathrm{oc,sc}}$ displays a voltage loss between 0.3 and 3 meV. While 3 meV is not negligible, the efficiency loss due to a low $J_{\mathrm{sc}}$ in this case is much more detrimental, ultimately rendering the solar cell ineffective. Moreover, these voltage losses due to a reduced $J_{\mathrm{sc}}$ are often mitigated by $\Delta V_{\mathrm{oc,rad}}$, which is predominantly negative and therefore effectively a voltage gain in comparison to $V_{\mathrm{oc,sc}}$ (discussed further below). In total, $V_{\mathrm{oc,rad}}$ closely mirrors $V_{\mathrm{oc,SQ}}$. However, non-radiative voltage losses are substantial and make up almost the complete voltage loss.

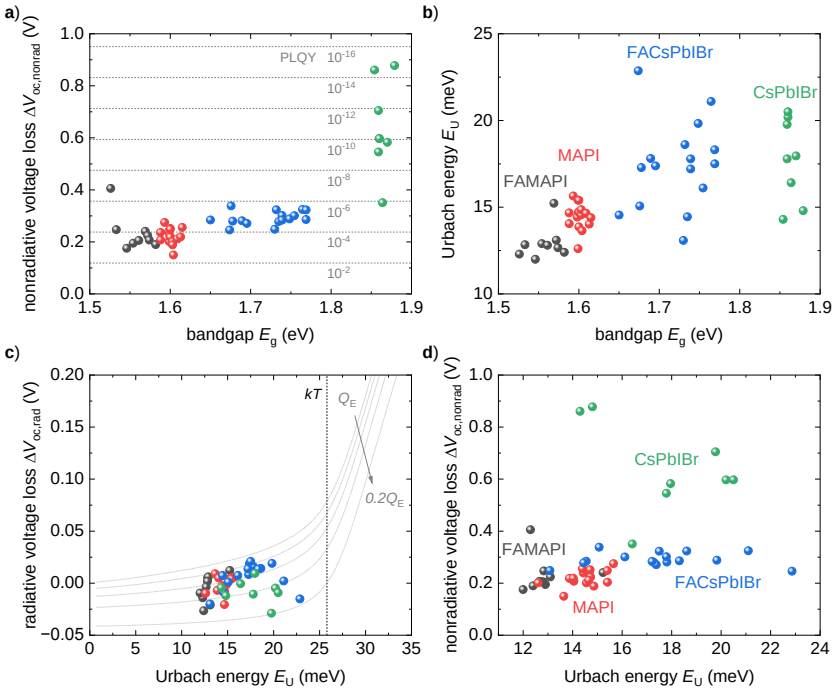


Figure 3.4 a) Nonradiative voltage losses as a function of the bandgap. The gray lines indicate the PLQY values that correspond to the specific voltage losses. b) Urbach energy as a function of the bandgap. c) Radiative and d) non-radiative voltage losses as a function of the Urbach energy. In c), the thermal energy $kT$ and the calculated behavior for $\Delta V_{\mathrm{oc,rad}}$ are illustrated. For the calculation, $Q_{\mathrm{E}}^{\mathrm{PV}} = b$ above the bandgap and $Q_{\mathrm{E}}^{\mathrm{PV}} = b \times \exp\left((E - E_{\mathrm{g}})/E_{\mathrm{U}}\right)$ below the bandgap is used where $b$ is an energy-independent factor between 0.2 and 1 representing imperfect light collection.

Therefore, Figure 3.4a illustrates the dependence of the non-radiative voltage loss on the bandgap directly. It is evident that except for a few outliers $\Delta V_{\mathrm{oc,non\text{-}rad}}$ grows with the bandgap. The increased voltage loss for wide bandgap perovskite solar cells is a known issue which is explained by poor CTL alignment, high interface recombination and partly halide segregation, displaying the complex influence of material and architectural factors on the performance.[146,147] Assuming the reciprocity relation is fulfilled and good electrical transport, $\Delta V_{\mathrm{oc,non\text{-}rad}}$ can be directly related to the PLQY of the device via $\Delta V_{\mathrm{oc,non-rad}} = \frac{kT}{q}\ln(Q_{\mathrm{e}}^{\mathrm{PL}})$. From the gray lines in Figure 3.4a, we can see that the PLQY in the best devices reaches only 0.3%, indicating possibilities for improvement. I use the relationship to the

PLQY in Chapter 5 to discuss the origin of voltage losses within co-evaporated perovskite solar cells in terms of device optimization.

Figure 3.4b shows the correlation between the extracted Urbach energy and the extracted bandgap for all samples of the four different perovskite compositions. The $E_U$ values for FAMAPI and MAPI range between 12 and 16 meV, showing minimal variation as previously discussed in Figure 3.1. FACsPbIBr and CsPbIBr demonstrate higher average values, but with stronger fluctuations spanning from 13 to 23 meV, indicating that achieving low Urbach energies is possible but dependent on the specific conditions of the fabrication process.

As the Urbach tail is the deciding factor of the low-energy part of the EL spectrum, a direct connection between the Urbach energy and the radiative voltage loss can be expected. The data plotted in Figure 3.4c do however not show a clear trend. As mentioned above, most of the $\Delta V_{oc,rad}$ values are negative, corresponding to an effective gain in comparison to $V_{oc,SQ}$. This somewhat surprising result can be explained by comparing the EL spectrum of the SQ limit with the one calculated from the EQE. The EL spectrum of the SQ limit follows $\phi_{BB}$ perfectly at high energies until the bandgap and then drops to 0. The calculated EL spectrum however extends to lower energies due to the band tail region of the EQE, effectively increasing $J_{0,rad}$ and consequential $\Delta V_{oc,rad}$. Nonetheless, if the EQE response just above the bandgap is below 1, the EL peak and high-energy part are reduced, leading to a decrease in $J_{0,rad}$ from which a negative $\Delta V_{oc,rad}$ can follow. To get an impression of the magnitude of the two effects, I perform a simple simulation. Artificial EQE curves are defined via

$$Q_E = \begin{cases} b \times \exp\left(\frac{E-E_g}{E_U}\right) & \text{for } E < E_g \\ b & \text{for } E \geq E_g \end{cases}, \tag{3.3}$$

where $b$ is a constant factor between 0 and 1, representing an overall EQE and corresponding $J_{0,rad}$ reduction. This EQE definition is used to calculate $\Delta V_{oc,rad}$ in dependence of $E_U$ for different $b$ and plotted as the gray lines in Figure 3.4c. As expected, $\Delta V_{oc,rad}$ is always positive for $b = 1$. This line represents the losses due to the increased absorption of the Urbach tail. For $b < 1$ and low $E_U$, $\Delta V_{oc,rad}$ becomes negative. Even though it is a simplified scenario, the curves can explain the variance of $\Delta V_{oc,rad}$ well. Note that the factor $b$ at high energies is irrelevant. Due to the influence of $\phi_{BB}$, only the EQE values up to 150 meV above the bandgap are important. As can be seen in the examples of Figure

3.2b, the experimental EQE values at these energies vary between 0.25 and 0.9 even for good performing cells. Therefore, I conclude that these two effects can explain the experimental data.

Another effect can be seen from the simulation, namely that the radiative voltage loss increases substantially for Urbach energies about the thermal energy *kT*, as also discussed before on experimental findings.[56] This is often observed for organic solar cells that show a large Stokes shift.[129] Notably, all extracted $E_U$ values remain below *kT*. Summing up, radiative recombination due to extended bandgap absorption does not play a substantial role in the voltage losses of co-evaporated perovskite solar cells.

As the Urbach tail is caused by structural and thermal disorder, there is the possibility that the Urbach energy is indicative of non-radiative recombination centers. Before, a linear relationship between $\Delta V_{oc,non\text{-}rad}$ and $E_U$ was found.[148] In our data in Figure 3.4d, I cannot see such a connection. Indeed, low Urbach energies lead to the lowest non-radiative losses but $\Delta V_{oc,non\text{-}rad}$ also varies for the same $E_U$. The voltage loss of FACsPbIBr cells is independent of the Urbach energy and the lowest $E_U$ of CsPbIBr cells lead to the highest loss.

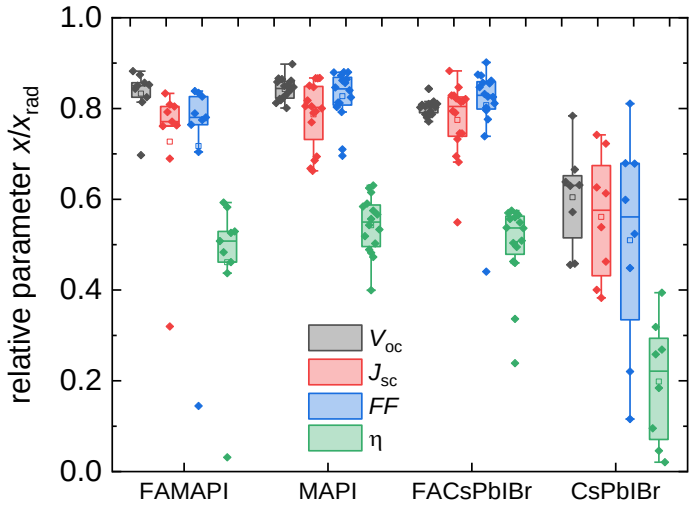


Figure 3.5 Box chart of the 4 relative parameters $V_{oc}/V_{oc,rad}$, $J_{sc}/J_{sc,rad}$, $FF/FF_{rad}$, and $\eta/\eta_{rad}$ for the 4 perovskite compositions.

Finally, having quantified $V_{oc,rad}$, $FF_{rad}$ can be estimated according to Equation (1.11). Assuming $J_{sc,rad} = J_{sc,SQ}$, the radiative limit of the PCE $\eta_{rad}$ is calculated following Equation (1.3). These parameters are the limits that need to be compared to the measured *JV* parameters, to find the biggest loss factor in co-evaporated perovskite solar cells. Therefore, in Figure 3.5 the fractions $x/x_{rad}$ are shown for the different perovskite compositions, where $x$ stands for one the four *JV* parameters. I find that for all investigated solar cells, each of the factors $V_{oc}$, $J_{sc}$, and *FF* contribute roughly equally to the PCE losses. For FAMAPI, MAPI, and FACsPbIBr, the individual losses amount to around 15-25%, resulting in a relative PCE loss of 45-50%. CsPbIBr shows the highest relative losses, highlighting the challenges in developing high-efficiency wide-bandgap perovskite solar cells. This is based on the issues of halide segregation of mixed halide perovskites and the difficulties of finding suitable CTLs.

All-in-all, I find no dominating loss factor regarding $V_{oc}$, $J_{sc}$, and *FF* for the efficiency in co-evaporated perovskite solar cells. Therefore, all 3 factors need to be investigated in further detail. I discussed $V_{oc}$ losses above, attributing them primarily to non-radiative

recombination mechanisms. Now, I expand on $J_{sc}$ and *FF* losses. $J_{sc}$ losses are conventionally ascribed to optical factors like reflection losses or parasitic absorption. Significant transport problems can however also influence the $J_{sc}$.

To clarify the origin of these losses, I examine the EQE spectrum of a MAPI solar cell in a linear scale in Figure 3.6a, providing spectral information on the $J_{sc}$ generation. At photon energies above the bandgap, the EQE remains consistently at a level above 80% up to 3 eV, from which point it declines. This decrease at high energies most likely stems from parasitic absorption of the ITO/$MoO_3$/TaTm top layers (compare with Figure 4.5a). The constantly high EQE indicates that the perovskite film is sufficiently thick to absorb photons near the bandgap. Nonetheless, to reduce the remaining 20% loss, a deeper understanding of its origins is required. For more insights, I determined the absorptance of the same device. In a complete solar cell with metal back electrode, no light is transmitted and the absorptance can be calculated solely by the light that is not reflected, $A = 1 - R$. Figure 3.6a indicates that the reflection losses contribute roughly 10% absolute to the $J_{sc}$ losses. Reflection losses can be mitigated by well-designed anti-reflective coatings or advanced light management.[149–153]

To exclude the effect of reflection losses, I determine the IQE by normalizing the EQE to the absorptance. Figure 3.6a shows that the IQE increases from around 85% at the bandgap to 95% at its maximum at 3 eV. The sub-unity IQE may be caused by both parasitic absorption and the charge collection efficiency, defined as the likelihood that a photogenerated charge carrier within the perovskite is extracted from the contacts. Given the wide bandgaps of most auxiliary layers in perovskite solar cells, parasitic absorption occurs primarily at high photon energies. Only the $C_{60}$ on the backside of the perovskite has a low bandgap and absorbs light efficiently which could explain the observed IQE behavior. At low photon energies, where the perovskite absorption coefficient declines, photons may pass through the perovskite layer, reflect off the Ag back electrode, and therefore transit through the $C_{60}$ twice on its way back to the perovskite. This could amplify parasitic absorption at low photon energies relative to higher energies where a single pass through the perovskite layer is sufficient for absorption. An alternative explanation for the below-unity IQE might be electrical losses. Constant series and shunt resistances can reduce the $J_{sc}$ wavelength-independent as discussed below. Furthermore, wavelength-dependent losses may be caused by a combination of recombination and extraction problems.[154–156] When a high-energy photon is absorbed, it creates an electron-hole pair near the front contact of the

solar cell, which is the hole extracting contact in the case of a *p-i-n* solar cell as in Figure 3.6a. The hole can be extracted immediately, while the electron must travel through the perovskite layer to reach the ETL. If trap states are present at the front interface, the proximity of both charge carriers enhances the interface recombination of these states. Consequently, a reduction in IQE at high photon energies suggests interface recombination at the HTL interface. In contrast, low-energy photons generate charge carriers more homogenously throughout the absorber layer. An IQE dip at low energies as observed here, is more indicative of bulk recombination or recombination at the ETL interface.

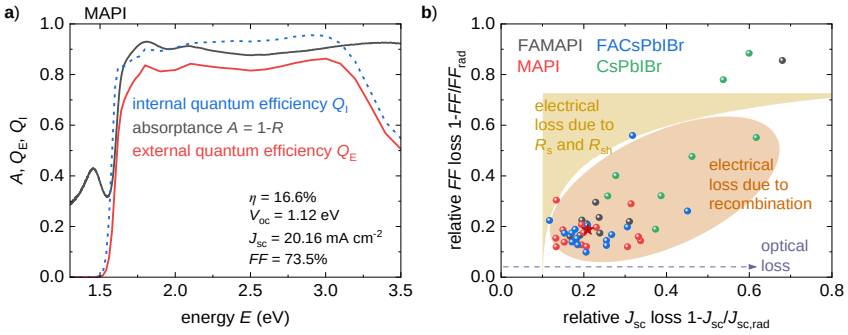


Figure 3.6 a) Absorptance $A$ of the device stack, external quantum efficiency $Q_E^{PV}$, and resulting internal quantum efficiency $Q_I^{PV}$ of a *p-i-n* MAPI solar cell. The *JV* parameters are listed. b) Relative *FF* loss vs. relative $J_{sc}$ loss, with point color indicating the perovskite composition. The yellow area indicates the impact of constant series and shunt resistances $R_s$ and $R_{sh}$, based on simulations with a 10% optical $J_{sc}$ loss. The horizontal arrow marks optical loss effects. The orange area highlights data points unexplained by constant $R_s$ and $R_{sh}$. The cell from a) is marked by a dark-red star.

In order to distinguish between optical and electrical losses, the relative *FF* loss is plotted as a function of the relative $J_{sc}$ loss in Figure 3.6b. The minimum measured *FF* loss is 10% of the radiative limit and the minimum $J_{sc}$ loss 12%. Over all data points, the two parameters seem weakly correlated where higher $J_{sc}$ losses accompany higher *FF* losses. Theoretically, the *FF* is predominantly influenced by electrical losses. Optical losses are manifested as a reduction in light intensity. Although the relationship between the *FF* and light intensity is generally complex, the *FF* shows minimal variation within the intensity range of 0.1 to 1 sun in most perovskite solar cells.[157] This suggests that if optical losses were solely responsible for a decrease in $J_{sc}$, the *FF* would largely remain stable, which is indicated in Figure 3.6b by the horizontal arrow. Therefore, optical losses cannot explain the general

trend of the measurement data. In the case of electrical losses, typically the effects of constant series and shunt resistances are discussed.[2] To illustrate the effect of the resistances, I performed a series of numerical evaluations of the *JV* behavior based on Equation (1.7) with the series resistance spanning from 0 to 1000 Ω $cm^2$ and the shunt resistance logarithmically from $10^4$ to 1 Ω $cm^2$ and extracted the *FF* and $J_{sc}$ losses. For the calculation, a bandgap of 1.6 eV and a 10% optical loss of $J_{sc}$ were assumed, according to the result of Figure 3.6a. All extracted simulated points fall within the yellow region shown in Figure 3.6b, while most experimental measurements lie outside this area. One explanation might be a co-occurrence of varying optical characteristics and resistances. However, given that the majority of the investigated solar cells share the same layers and that the refractive indices across the different perovskites are comparable, I infer that optical losses are relatively consistent among the cells analyzed.[158] Notably, the parameters of the solar cell from Figure 3.6a (marked by a star in Figure 3.6b) also fall outside of the yellow region. Therefore, I conclude that the losses in $J_{sc}$ and FF cannot be explained by constant series and shunt resistances plus optical losses. Instead, the losses likely arise from a combination of extraction problems and recombination, as discussed above and further examined in Chapter 4.

## 3.3 Conclusion

In this study, I analyzed the efficiency losses in co-evaporated perovskite solar cells, focusing on the contributions of $V_{oc}$, $J_{sc}$, and *FF* to the overall performance. Importantly, all three JV parameters were found to contribute equally to the efficiency losses. Using high-dynamic-range EQE measurements across various perovskite compositions, voltage losses were split up into absorptive, radiative, and non-radiative components. Our findings confirm that non-radiative recombination dominates the voltage losses, with radiative losses being negligible due to the low Urbach energies of the materials studied. For the purpose of optimizing the device efficiency, it is necessary to know the spatial origin of the non-radiative recombination. This can happen inside the absorber layer or at the interfaces with the CTLs which will be investigated in Chapter 5. I further evaluated the sub-unity IQE, identifying parasitic absorption and collection inefficiencies as potential contributors to $J_{sc}$ losses. By analyzing the interplay between $J_{sc}$ and FF, I isolated the effects of optical and electrical losses, concluding that electrical recombination and extraction issues are the

drivers of FF and $J_{sc}$ losses. In chapter 4, I will explore a method to investigate these recombination losses during extraction.

# 4 Recombination Losses during Extraction

In Chapter 3, I demonstrated that co-evaporated perovskite solar cells exhibit a correlation between $J_{sc}$ and *FF* losses, primarily attributed to electrical losses that cannot be fully described by constant series and shunt resistances. In this chapter, I delve deeper into the origins of these losses. Here and in Chapter 5, I focus specifically on MAPI solar cells, as this perovskite system benefits from a well-established baseline fabrication process and exhibited the smallest relative losses in the previous analysis. Part of the content of this chapter has been published in ref [159]. I would like to mention that a work of a similar nature was published concurrently as the results presented herein.[119]

## 4.1 Introduction

As already mentioned, under OC conditions no charge is extracted; hence, all photogenerated charge carriers must recombine either radiatively or non-radiatively. Ideally, only radiative recombination occurs (radiative limit); in practice, however, non-radiative recombination reduces the charge carrier density, thus lowering the $V_{oc}$ in the device. At SC conditions, it is generally assumed that all generated charges are extracted. Consequently, low $J_{sc}$ in halide perovskite solar cells is commonly attributed to limited charge carrier generation, which may result from low perovskite absorptivity or suboptimal light management, such as reflection losses or parasitic absorption in the CTLs. However, if charge extraction is hindered (e.g. due to charge barriers or low mobilities), charges may recombine even at SC and thus reduce $J_{sc}$ as well. The *FF*, ideally dictated by the $V_{oc}$ and the ideality factor, is also influenced by recombination. Yet, additional transport-related challenges, such as resistive losses or a combination of mobility and recombination problems, can further reduce the *FF*.[119,160]

The values of $V_{oc}$, *FF*, and $J_{sc}$ in metal halide perovskite solar cells are approaching their theoretical radiative limits.[161] Achieving further improvements requires a profound

understanding on the cells working mechanisms. However, identifying the physical processes that constrain performance is challenging due to the unconventional properties of these materials, such as their intrinsic nature and ion migration, which add complexity to their behavior.[31,162,163]

In this context, PL analysis emerges as a valuable tool to investigate residual losses in high-performing solar cells. Qualitative comparisons of PL signals across perovskite films have been widely used to infer variations in film quality, where stronger PL signals are associated with reduced non-radiative recombination.[164–166] Moreover, if PL is measured in an absolute scale (photons $eV^{-1}$ $s^{-1}$ $m^{-2}$) by calibrating the detection system with a quantitatively known light source, the signal can be directly related to the QFLS in the absorber layer of the device.[36] Studies employing this technique have explored QFLS differences in composition spread libraries,[167] surface passivation,[168] interface voltage losses,[169,170] spatial homogeneity of the QFLS,[171] and the ideality factor[172] among others. All these measurements were performed at OC conditions (not contacted) where the PL intensity should peak in the energy-generating regime due to the requirement that all photogenerated charge carriers recombine.

Complete devices, however, can be electrically contacted and subjected to different bias conditions during the PL measurement. At SC, the PL intensity in an ideal solar cell should approach Planck radiation levels as all the photogenerated charge carriers are extracted. This enables the differentiation of absorption losses from extraction problems at SC[173,174] and was already employed in a relative scale for perovskite devices.[174,175] In silicon solar cells, PL measurements under an extended region of applied bias voltages have been used to investigate diffusion length and surface passivation.[155,176] For example, Haug et al. demonstrated how applied bias affects surface recombination velocity at the back contact, providing insights into recombination-active defects and field-effect passivation. In ternary organic solar cells, Tress et al. could distinguish the emission of locally bound exciton states from the more delocalized excimer states with voltage-dependent PL measurements.[177]

Here, I integrate absolute photon calibration with bias-dependent PL measurements to estimate the radiative and ultimately the non-radiative recombination current densities along the *JV* curve under one-sun equivalent illumination. The resulting voltage dependence of the low PLQY indicates a complex source of recombination. Furthermore, the high QFLS even under SC conditions suggests significant charge extraction problems

that lead to recombination losses. The differences between absorbed, generated and extracted current densities yield substantial parasitic absorption and recombination losses under all bias conditions, effectively reducing $J_{sc}$ and *FF*.

## 4.2 Results and Discussion

The measurements are performed on a *p-i-n* vacuum-deposited MAPI solar cell similar to those reported elsewhere,[178,179] with an architecture consisting of an ITO coated glass slide, covered with $MoO_3$/TaTm/MAPI/$C_{60}$/BCP/Ag. The *JV* measurement under simulated AM1.5G illumination results in $V_{oc}$ = 1.11 V, *FF* = 70%, and $J_{sc}$ = 18.0 mA cm$^{-2}$, yielding $\eta$ = 14.0% (see Figure 4.1a).

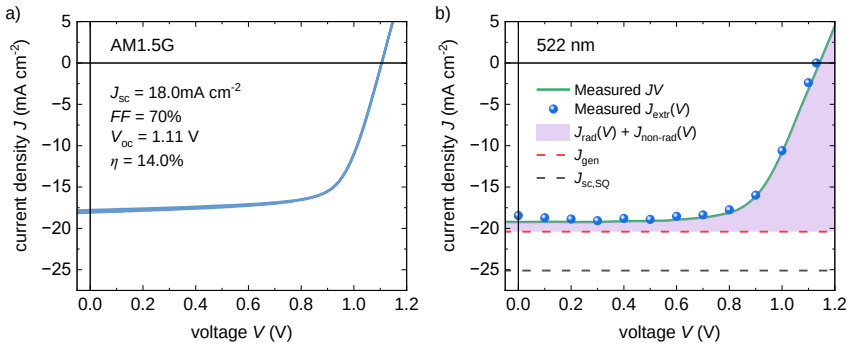


Figure 4.1 a) *JV* characteristics of the MAPI solar cell under simulated AM1.5G illumination and fast scan speed. b) *JV* characteristics under one-sun-equivalent laser illumination of the MAPI solar cell. The current density $J_{extr}$ is measured simultaneously with the steady-state absolute PL, resulting in a slow scan speed due to the PL integration time, while the *JV* scan was measured under the same illumination but with a fast scan speed. The total photogenerated current $J_{gen}$ as estimated from Figure 4.5 is assumed to be voltage independent, as well as $J_{sc,SQ}$ which represents its maximum theoretical value. The recombination losses are the difference between $J_{gen}$ and $J_{extr}$ and are shown as shaded area.

To obtain information about the recombination rates, it is essential to study the detailed balance between charge generation, recombination and extraction currents. Figure 4.1b indicates their relation. $J_{gen}$ is the current density of free charge carriers photogenerated within the absorber and is expressed therefore in units of electrical current density, mA cm$^{-2}$, where the charge carrier generation rate *G* is integrated over the absorber thickness and multiplied by the elementary charge *q*. This parameter is assumed to be voltage-independent, considering the low exciton binding energy of MAPI.[180] The maximum value

for $J_{gen}$ is the SQ limit of the short-circuit current density $J_{sc,SQ}$ as defined in Equation (1.8) which has the assumption that all photons of the solar spectrum with energies above the bandgap are absorbed and generate an electron-hole pair that is extracted. For our vacuum-deposited MAPI in the cubic phase with a typical $E_g$ = 1.61 eV, $J_{sc,SQ}$ reaches 25.1 mA cm$^{-2}$.[99] However, the actual value of $J_{gen}$ is reduced mainly by sub-unity absorption, front reflection, and parasitic absorption. The generated charge carriers are either extracted as current density at the metal contacts, which I call $J$ for a fast $JV$ scan and $J_{extr}$ for the combined voltage-dependent PL measurement (Figure 4.1b, green line and red dots, respectively), or they recombine with rate $R_{tot}$ which can be translated into a recombination current density $J_{rec}$ (Figure 4.1b, yellow area). Recombination can occur radiatively, associated with a radiative recombination current density $J_{rad}$, or non-radiatively, associated with a non-radiative recombination current density $J_{non\text{-}rad}$. Importantly, the charge extraction and recombination can in general be voltage dependent. Therefore,

$$\begin{aligned} J_{\mathrm{gen}} &= J_{\mathrm{extr}}(V) + qdR_{\mathrm{tot}}(V) = J_{\mathrm{extr}}(V) + J_{\mathrm{rec}}(V) \\ &= J_{\mathrm{extr}}(V) + J_{\mathrm{rad}}(V) + J_{\mathrm{non-rad}}(V) \end{aligned} \tag{4.1}$$

The generated and radiative current density can be calculated in accordance with Equations (1.2) and (1.4) and non-radiative recombination can be split-up in Auger and trap-mediated SRH recombination,[181,182]

$$J_{\mathrm{gen}} = q\int_0^{\infty} A(E)\left(\phi_{sun}(E) + \phi_{\mathrm{BB}}(E)\right) dE \tag{4.2}$$

$$J_{\mathrm{rad}}(V) = qd\, k_{\mathrm{rad}} n_{\mathrm{i}}^2 \exp\left(\frac{qV}{kT}\right) = q \exp\left(\frac{qV}{kT}\right)\int_0^{\infty} A(E)\phi_{\mathrm{BB}}(E)dE, \tag{4.3}$$

$$J_{\mathrm{SRH,deep}}(V) = qd\, \frac{n_{\mathrm{i}} \exp\left(\frac{qV}{2kT}\right)}{\tau_{\mathrm{SRH,p}} + \tau_{\mathrm{SRH,n}}}, \tag{4.4}$$

$$J_{\mathrm{SRH,shallow}}(V) = qd\, \frac{n_{\mathrm{i}}^2 \exp\left(\frac{qV}{kT}\right)}{n_1\, \tau_{\mathrm{SRH,p}}}, \tag{4.5}$$

$$J_{\mathrm{Auger}}(V) = qd\, C_{\mathrm{Auger}} n_{\mathrm{i}}^3 \exp\left(\frac{3qV}{2kT}\right). \tag{4.6}$$

Here, the black-body radiation was added additionally in comparison to Equations (1.2) and (1.4) to account for processes happening in thermal equilibrium. I want to point out that $A$

refers here to the absorptance of the perovskite film and not the complete device. Further, $n = p$ was assumed. Equations (4.3) - (4.6) describe the general voltage dependence of the recombination mechanisms, where for the SRH recombination in Equation (4.4) a deep trap was considered and in Equation (4.5) a shallow trap.

At SC conditions, ideally, all the photogenerated charge carriers are extracted ($J_{gen} = J_{sc}$); a circumstance which is assumed in many works.[129,169,170,182–185] From Equations (4.3) - (4.6) it is apparent that in this case ($V = 0$) only the intrinsic charge carriers will recombine and therefore just Planck radiation will be emitted which is too small to measure with most detectors. However, in a real device, it can happen that the charge extraction is not substantially faster than the recombination and therefore also the radiative and non-radiative current densities can have substantial magnitude and reduce $J_{sc}$ as each excess charge carrier that recombines at SC conditions cannot be extracted and is a loss.

At OC conditions, there is no net current flow from the device contacts ($J_{extr}(V_{oc}) = 0$), so $J_{gen}$ and the recombination current densities compensate:

$$J_{\mathrm{gen}} = J_{\mathrm{rad}}(V_{\mathrm{OC}}) + J_{\mathrm{non-rad}}(V_{\mathrm{OC}}). \tag{4.7}$$

At these conditions, the PLQY is often used to quantify the sample quality. At OC, the PLQY shows the share of radiative recombination among the total recombination ($Q_{\mathrm{e}}^{\mathrm{PV}} = \frac{J_{\mathrm{rad}}(V_{\mathrm{OC}})}{J_{\mathrm{rad}}(V_{\mathrm{OC}}) + J_{\mathrm{non-rad}}(V_{\mathrm{OC}})}$). One can define a generalized voltage-dependent extraction-independent PLQY analogously,

$$\begin{aligned} Q_{\mathrm{e}}^{\mathrm{PV}}(V) &= \frac{J_{\mathrm{rad}}(V)}{J_{\mathrm{rad}}(V) + J_{\mathrm{non-rad}}(V)} \\ &= \frac{1}{1 + \frac{1}{\left(\tau_{\mathrm{SRH,p}} + \tau_{\mathrm{SRH,n}}\right) p_{\mathrm{e}} k_{\mathrm{rad}} n_{\mathrm{i}} \exp\left(\frac{qV}{2kT}\right)}}. \end{aligned} \tag{4.8}$$

On the right-hand side, I neglected Auger recombination and included the escape probability $p_e$ of the radiative recombination. Equation (4.8) gives an estimation of the voltage dependence of the PLQY for an intrinsic semiconductor with a deep trap. However, other trap depths, transport issues and localized effects such as interface recombination, inhomogeneous charge distribution or ionic movement might complicate the voltage dependence.[172,186,187] Therefore, it is necessary to characterize the dependence in experiments more thoroughly.

In a standard *JV* measurement, only $J_{extr}(V)$ is reported for solar cells. By placing an integrating sphere which is calibrated to absolute photon numbers onto the electrically contacted solar cell, it is possible to record $J_{extr}(V)$ and $J_{rad}(V)$ simultaneously, as discussed in Chapter 2.3.2. Here, I neglect other potential losses such as PL which is laterally guided out of the structure or absorbed by the CTLs and thus not collected. The solar cell is illuminated by a green laser ($\lambda$ = 522 nm) under one sun equivalent intensity which is achieved by matching the $J_{sc}$ obtained by the measurement using the solar simulator. The solar cell *JV* measured under this illumination achieves a $V_{oc}$ = 1.13 V, *FF* = 68 %, and $J_{sc}$ = 19.2 mA cm$^{-2}$ (as illustrated in Figure 4.1b), values which are comparable to the ones measured under AM1.5G simulated illumination. The PL signal is separated from the laser via a 600 nm long-pass filter and collected in a spectrometer. For further details about the experimental methods see Chapter 2.3.2.

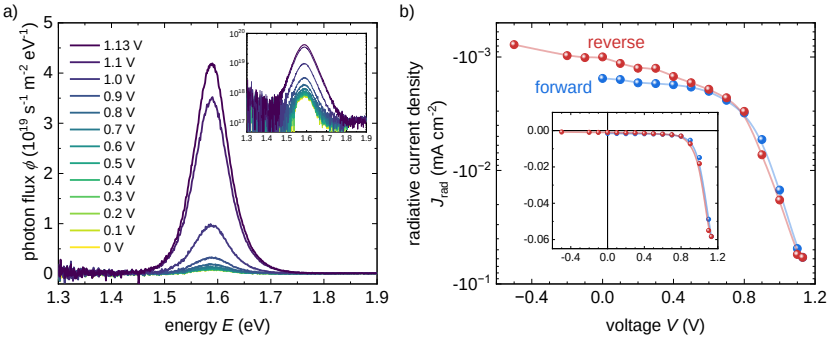


Figure 4.2 (a) Absolute photoluminescence spectra obtained at different steady state operating voltages for the solar cell measured under one sun equivalent illumination in the forward direction and (b) $J_{rad}$ derived from both the forward and reverse direction with logarithmic y scale. The inset depicts the same data in a linear scale.

The measurement of the steady-state absolute PL at bias potentials along the *JV* enables the direct estimation of $J_{rad}$ (see Figure 4.2) by integrating the PL peak and multiplying by the electric charge of an electron. The emission has to be maximized at OC conditions, where there is no net current flow ($J_{extr}$ = 0). In the ideal case, non-radiative recombination paths are considered inactive and thus $J_{non\text{-}rad}$ = 0 and $J_{gen} = J_{rad}$. The fact that $J_{rad}(V_{oc}) << J_{sc} \leq J_{gen} \leq J_{sc,SQ}$ (compare Figure 4.1b and Figure 4.2) indicates significant non-radiative losses. In the end of the reverse scan, the cells started to degrade, making the data points at low voltages ($V$ < 0.5 V) less trustworthy.

At SC conditions, perfect extraction is often assumed, implying $J_{gen} = J_{sc}$, in which case no recombination of the excess charge carriers should happen and only the black-body radiation for a semiconductor with a bandgap of $E_g$ = 1.61 eV should be emitted from the solar cell.[174] Despite the recorded luminescence at $V = 0$ is small (Figure 4.2), it is however much greater than $J_0$ which implies a certain degree of radiative losses compared to the ideal fully-quenched case. This kind of signal at SC conditions would be expected in the case of charge extraction problems or low mobility systems,[173] a circumstance which has also been discussed for metal halide perovskites.[188] Assuming that the relation $J_{rad} << J_{non\text{-}rad}$ is also fulfilled at SC, as discussed below, this suggests that $J_{non\text{-}rad}$ might not be negligible and therefore $J_{sc} < J_{gen}$, as previously suggested in Chapter 3 and in the literature by other electrical techniques.[189]

It should be noted that $J_{rad}$ does not show the exponential behavior as expected from Equation (4.3), as a straight line would be expected in the semi-logarithmic plot, but it rather saturates at low voltages. This indicates that the internal voltage or QFLS $\Delta E_F$ in the perovskite layer is higher than the externally applied voltage which can be ascribed to imperfect charge extraction.

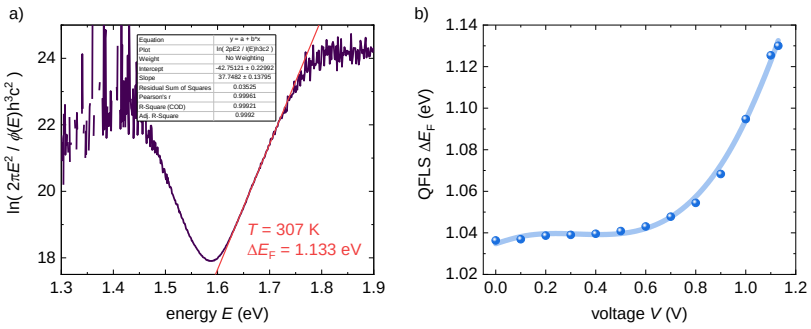


Figure 4.3 a) High-energy tail fit of the spectrum measured under OC conditions to determine the QFLS $\Delta E_F$. b) QFLS as a function of the applied voltage.

In order to check the difference between the voltage and the QFLS, $\Delta E_F$ is calculated from the luminescence at OC conditions via the fit of the high-energy tail as discusses in Chapter 1.3 following previously reported procedures.[190] Furthermore, this approach validates the calibration of the measurement setup, since at OC conditions $\Delta E_F = V_{oc}$, if no strong band misalignments occur in the device.[191] As shown in Figure 4.3a, I obtain a QFLS of 1.13 eV, in excellent agreement with the electrically measured $V_{oc}$. The carrier temperature $T$ is a

fitting parameter and appears with 307 K realistic. At other applied voltages, the QFLS is determined via $\Delta E_F(V) = \Delta E_F(V_{oc}) + kT \ln\left(\frac{J_{rad}(V)}{J_{rad}(V_{oc})}\right)$, as the spectra at low voltages become too noisy for accurate fitting. Figure 4.3b illustrates that the QFLS decreases only slightly with the applied voltage and saturates at voltages below 0.6 V. Even at SC conditions, the QFLS is maintained at 1.035 eV, indicating a high charge carrier density within the perovskite.

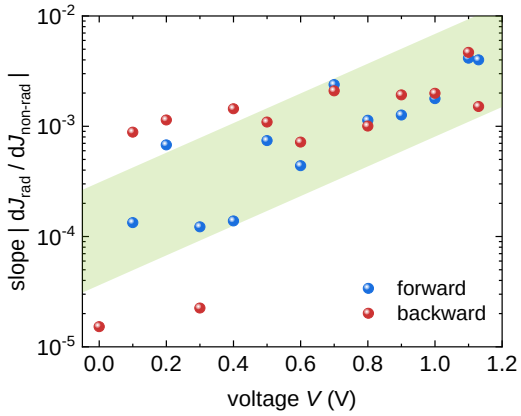


Figure 4.4 Slope of the relation $J_{rad}(J_{non\text{-}rad})$ of the solar cell at different voltages as determined by Equation (4.9). Both forward and reverse scans are represented. The green band is a fit of the data from the forward direction and serves as guide to the eye.

Despite the additional knowledge of $J_{rad}$, $J_{gen}$ remains elusive, preventing precise determination of $J_{non\text{-}rad}(V)$ and $Q_e^{PV}(V)$. $J_{gen}$ can in principle be simulated if the excitation spectrum, power and all optical constants, i.e. the refractive indices and extinction coefficient of all layers, are known. However, accurately measuring these optical constants for very thin films is challenging, and they are often subject to uncertainties. Even without further knowledge besides $J_{extr}$ and $J_{rad}$, a qualitative understanding of the voltage dependence of $J_{non\text{-}rad}$ relative to $J_{rad}$ can still be achieved. I utilize the voltage-independent nature of $J_{gen}$ by determining numerically the derivative of $J_{rad}$ in dependence of $J_{non\text{-}rad}$ (Equation (4.1)),

$$\frac{\partial J_{rad}}{\partial J_{non-rad}} = \frac{-1}{\frac{\partial J_{extr}}{\partial J_{rad}} + 1}, \tag{4.9}$$

which only depends on $J_{extr}$ and $J_{rad}$. If this "slope" is constant one can deduce that the ratio of $J_{rad}/J_{non\text{-}rad}$ is constant over the voltage range. If the "slope" changes, the ratio changes as well, which can give important information about the non-radiative recombination source. Figure 3 shows $\partial J_{rad}/\partial J_{non\text{-}rad}$ for both the forward and the reverse scan directions. Due to the derivative and the small values of $J_{rad}$, the data points exhibit noticeable scattering. Nevertheless, the trend appears to increase linearly on the semi-logarithmic scale, suggesting exponential behavior. The slope varies with voltage, indicating that the dependence of non-radiative recombination on voltage differs from that of radiative recombination. Since $\partial J_{rad}/\partial J_{non\text{-}rad}$ is increasing with $V$, it follows that at SC there is relatively more non-radiative losses than at OC, with respect to the radiative recombination, in accordance with SRH recombination (compare Equations (4.3) and (4.4)). However, this conclusion is only a weak indication and does not rule out other recombination mechanisms apart from Auger recombination.

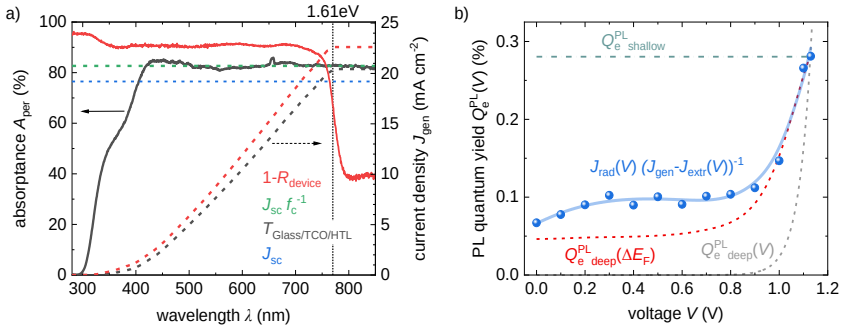


Figure 4.5 (a) Comparison of methods for calculating the generated current density $J_{gen}$. On the left axis (solid lines), the potential absorptance spectrum of the perovskite is shown, estimated either from the reflection of the complete device or the transmittance of the glass/TCO/HTL sample consisting of glass/ITO/$MoO_3$/TaTm. On the right axis (dashed lines), the integrated current densities corresponding to the spectra of the left axis. Additionally, $J_{gen} = J_{sc}\ f_c^{-1}$ is indicated, based on an ideality factor of $n_{id} = 1.4$, and the measured $J_{sc}$. (b) Voltage-dependent PLQY $Q_e^{PL}(V)$, as calculated from the experimental $J_{rad}$ and $J_{extr}$ and $J_{gen} = 20.75$ mA cm$^{-2}$, together with theoretical behaviors of a deep and a shallow trap, following Equations (4.3) - (4.5) and (4.8). The deep trap case was calculated once as a function of the QFLS $\Delta E_F$ and once as a function of the $V_{oc}$. The parameters used for the calculation are $p_e = 0.05$, $k_{rad} = 3\times10^{-11}$ cm$^3$ s$^{-1}$, $n_i = 8\times10^4$ cm$^{-3}$, $\tau_{SRH,p} + \tau_{SRH,n} = 7.3\times10^{-6}$ s for the deep trap, and for the shallow trap $\tau_{SRH,p}n_1 = 1.9\times10^9$ s cm$^{-3}$, obtained to match the value at OC conditions.

In an attempt to quantify $J_{non\text{-}rad}$ and $Q_e^{PL}(V)$, I employ three different approaches to estimate $J_{gen}$, as illustrated in Figure 4.5a. The first two methods are based on predicting the absorptance spectrum of the perovskite film in the device. In the first approach, I assume that no parasitic absorption occurs in the supporting layers. Under this circumstance, the reflectance spectrum of the device provides a direct measure of the perovskite absorption, as all photons not absorbed by the perovskite are reflected due to the reflective metal back contact. Using this assumption and considering 1-sun illumination, the estimated generation current is 22.6 mA cm$^{-2}$. However, the transmittance spectrum of the top layers (glass/ITO/$MoO_3$/TaTm) reveals that this assumption is at least partially wrong. Especially in the UV, these layers absorb a substantial amount of light. The second method is therefore based on this transmission spectrum, assuming that all the light that is transmitted by this sample is absorbed by the perovskite. The resulting $J_{gen}$ yields 20.4 mA cm$^{-2}$. However, this method also has limitations, since the optical response of a multilayer stack is not simply additive, meaning that the two different stacks cannot simply be compared. The reflection at the TaTm-air interface differs from that at the TaTm-perovskite interface due to the different refractive indices. Additionally, thin-film interference effects may alter the electromagnetic field distribution. Thus, the reliability of $J_{gen}$ estimated by this method is also limited. The third approach involves the voltage-dependent PL measurements. It was shown that the photocurrent collection efficiency $f_c$ at SC conditions can be calculated via the quenching of the PL intensity at SC $\phi_{sc}$ in comparison to the PL intensity at OC $\phi_{oc}$, [192]

$$f_c = \frac{J_{sc}}{J_{gen}} = 1 - \left(\frac{\phi_{sc}}{\phi_{oc}}\right)^{\frac{1}{n_{id}}}. \tag{4.10}$$

Using the $J_{sc}$ of 19.2 mA cm-2, the luminescence quenching of 0.0265, and the ideality factor of 1.4 (compare Figure 5.4b), this method gives a collection efficiency of $f_c$ = 92.5% and a generation current density of $J_{gen}$ = 20.75 mA cm$^{-2}$. I adopt this value in the subsequent analysis due to the identified limitations of the other two approaches. Additionally, this method ensures self-consistency within the framework of our measurements and calculations. Based on this estimation, we find that $J_{gen} \neq J_{sc}$ with 1.85 mA cm$^{-2}$ lost due to parasitic absorption (7.5% loss relative to SQ limit) and additional 1.55 mA cm$^{-2}$ lost due to recombination at SC conditions (6.2% relative loss). This answers the open question from Chapter 3 about the origin of the IQE losses.

I note that this $J_{sc}$ analysis was subsequently applied together with a colleague to an optically optimized MAPI solar cell with higher efficiency ($\eta$ = 20%). In this device, reflection losses were reduced to 0.53 mA cm$^{-2}$, and parasitic absorption losses were minimized to 0.50 mA cm$^{-2}$. However, electrical losses due to recombination remained the dominant contributor, accounting for 1.27 mA cm$^{-2}$, along with transmission losses at longer wavelengths, as that particular device had semitransparent electrodes on both sides.[149]

Furthermore, the knowledge of $J_{gen}$ enables the calculation of the voltage-dependent PLQY, as shown in Figure 4.5b. The PLQY decreases towards lower voltages, consistent with the observations from Figure 4.4 and expected for a solar cell where the recombination is dominated by a deep trap. To compare with theoretical predictions, the voltage dependence described by Equations (4.3) - (4.5) and (4.8) is plotted in Figure 4.5b for both deep-trap-dominated and shallow-trap-dominated recombination scenarios. These curves are scaled to match the $Q_e^{PL}$ at OC conditions. For the shallow trap case, where recombination scales in the same way as radiative recombination with charge carrier concentration, the PLQY remains constant. For the deep-trap scenario, as detailed in Equation (4.8), $Q_e^{PL}$ is calculated as a function of the QFLS but plotted against the voltage, where I use the relationship $\Delta E_F(V)$, established in Figure 4.3b. The experimental data deviates from the theoretical behavior with the PLQY at low voltages being higher than predicted. This discrepancy could arise from several factors, including the presence of traps with medium-depth, a combination of different traps, or mobile ions that alter the trap distribution during voltage-dependent PL measurement. Additionally, $Q_e^{PL}$ is plotted as a function of voltage to show the behavior expected for perfect transport, where $\Delta E_F = V$. In that case, the PLQY would decrease rapidly towards low voltages, increasing the PL quenching at SC even further and decreasing recombination losses.

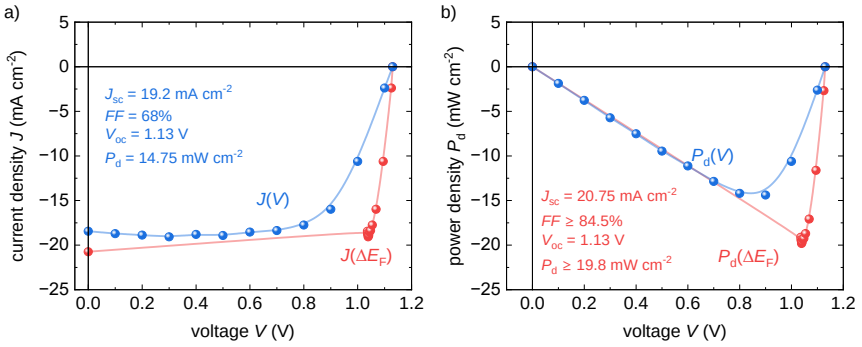


Figure 4.6 a) *JV* characteristics where the extracted current is plotted either as a function of the voltage $V$ or the QFLS $\Delta E_F$. For the $J(\Delta E_F)$ curve, the generated current density $J_{gen}$, as estimated above, is added at $V$ = 0 V. b) The power density $P_d$ corresponding to the *JV* curves in a).

Finally, using the established relation $\Delta E_F(V)$, the FF and PCE limits for the scenario with perfect charge transport can be quantified. Under ideal charge extraction conditions, the internally generated QFLS will always match the externally applied voltage, i.e. $\Delta E_F = V$. Figure 4.6a shows the extracted current as a function of both the voltage $J(V)$, representing the real *JV* curve of the device, and the QFLS $J(\Delta E_F)$, which defines the limit for perfect transport.[192] In the latter case, also $J_{sc} = J_{gen}$ is valid, so this point is added to the curve. Due to the limited range of $\Delta E_F$ on the JV curve, the resulting plot does not form a smooth curve, allowing only the determination of a minimum FF value. Nevertheless, the minimum FF for the transport-optimized solar cell represents with 84.5% a significant improvement over the measured FF of 68% (18.2% relative improvement to the SQ limit). Together with the $J_{sc}$ increase, the extracted power density improves from 14.5 to at least 19.8 mW cm$^{-2}$. Although these values are not determined under the AM1.5G spectrum at 100 mW cm$^{-2}$, I expect the improvement under the sun spectrum to behave similarly.

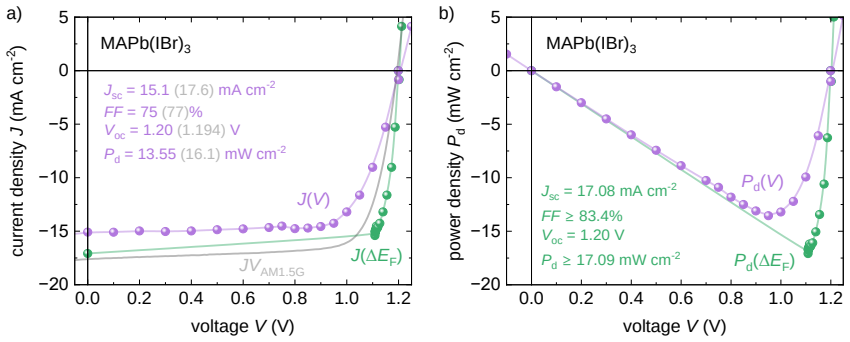


Figure 4.7 a) *JV* characteristics of a $MAPb(IBr)_3$ solar cell, where the extracted current is plotted either as a function of the voltage $V$ or the QFLS $\Delta E_F$. For the $J(\Delta E_F)$ curve, the generated current density $J_{gen}$, as estimated from the PL quenching following Equation (4.10), is added at $V = 0$ V. Additionally, the JV curve of the same solar cell, as measured under simulated AM1.5G illumination, is plotted. b) The power density $P_d$ corresponding to the *JV* curves in a).

The same analysis was conducted in a $MAPb(IBr)_3$ perovskite solar cell with a wider bandgap of $E_g$ = 1.68 eV for tandem applications, as shown in Figure 4.7. Here, we find that the $J_{sc}$ would be increased from 15.1 to 17.08 mA cm$^{-2}$ (8.5% improvement relative to the SQ limit of 23.06 mA cm$^{-2}$) and the *FF* from 75% to at least 83.4% (9.2% relative improvement), if the charge extraction could be optimized. This indicates that the *FF* suffered especially in the MAPI cell from internal transport issues. The remaining FF deficit could be caused by classical series and shunt resistances as well as pure recombination losses.

It should be noted that while this analysis successfully quantifies $J_{sc}$ and *FF* losses due to transport issues and recombination under the employed light source and slow scan speeds (required for PL measurements), direct comparison with standard *JV* parameters measured under simulated AM1.5G illumination is not straightforward. Figure 4.7a shows both *JV* curves, highlighting slight differences, particularly in $J_{sc}$, which affect the output power (also visible in the comparison of Figure 4.1a and b). These discrepancies stem from difficulties in setting the laser power calibration and additionally the prolonged scan duration, which may cause ion movement in the perovskite. Improved experimental procedures, including finer laser adjustments and the use of stable solar cells, could mitigate these issues.

## 4.3 Conclusion

In this chapter, I investigated the interplay of charge generation, recombination, and extraction in co-evaporated perovskite solar cells, with a focus on the origins of $J_{sc}$ and *FF* losses beyond reflection. By voltage-dependent PL measurements, calibrated to the absolute photon flux, I quantified the radiative and extracted current densities along the *JV* curve. The high QFLS even under all biases indicated that charge transport is not working efficiently, allowing the carriers to recombine before being extracted. The voltage-dependent PLQY suggested that the recombination is neither dominated completely by deep traps nor by shallow traps. Determining the generated current density in three different ways confirmed that in the investigated MAPI device $J_{sc} \neq J_{gen}$, with considerable 1.85 mA $cm^{-2}$ loss attributed to parasitic absorption and 1.55 mA $cm^{-2}$ loss due to recombination even under SC conditions. In an idealized scenario of perfect charge transport, the *FF* of the solar cell would improve substantially, as shown by a predicted *FF* of at least 84.5% compared to the measured value of 68%. I extended this methodology to $MAPb(IBr)_3$ solar cells with wider bandgap and found similar results demonstrating the universality of the findings.

# 5 Bulk and Interface Recombination

In the Chapters 3 and 4, we saw that the PLQY of the finished device is far below unity which causes non-radiative voltage losses. Now, I want to have a look at the spatial origin of these losses. This chapter is published in ref [193].

## 5.1 Introduction

Achieving very high efficiencies in perovskite solar cells requires minimizing $V_{oc}$ losses, which involves reducing non-radiative recombination of photogenerated charges. Non-radiative recombination can occur either inside the perovskite bulk material or at the interfaces with the CTLs, and it is often quantified by the PLQY. The PLQY is directly linked to the QFLS and indirectly to the $V_{oc}$, meaning that a reduction in radiative recombination implies a loss in QFLS or $V_{oc}$. To date, perovskite films with outstanding external PLQYs up to 66%, indicating internal PLQYs close to 100%, have been reported.[34,65–70] Such high PLQY values are obtained mostly for solution-processed films, the most widely-adopted perovskite absorbers, and highlight their potential to reach PCEs above 28%.[194] This is not completely surprising given that most defects in the bulk of perovskites lead to shallow trap states,[61,195] that induce minimal non-radiative charge carrier recombination. In addition, solution-processed perovskites often exhibit large micrometer-sized grains, hence they are less affected by recombination centers at the grain boundaries.[65,196–198] In view of the high PLQY values obtained for thin perovskite films, and the strong reduction observed after contacting to the CTLs, the consensus is that non-radiative recombination at the perovskite interfaces is the major loss factor. As a result, there has been a strong focus on understanding and suppressing interface recombination at the CTLs. Indeed, a prevailing strategy to improve device efficiency involves the screening of alternative CTLs and/or the introduction of passivating interlayers at the absorber surface.[37,96,191,194,199–207]

In spite of the predominance of solution-processed perovskites in research, thermal evaporation is achieving perovskites with promising properties with a higher potential for scalability and reproducibility.[208–213] Using sequential evaporation, solar cells with PCEs up to 26.21% certified have been reported recently.[214] Yet, in general, thermally evaporated perovskites are still poorly understood. As a result, only a few reports of perovskite solar cells using co-evaporation of the precursors show PCEs above 20%.[215,216] This opens the debate on the dominating recombination centers in co-evaporated perovskite solar cells. Indeed, they typically consist of small crystal grains, which leads to more grain boundaries and structural defects than their solution processed analogues.[209] Consequently, these films are expected to suffer from elevated recombination losses, which aligns with the short charge-carrier lifetimes frequently reported.[217]

Here, I study the origin of trap-assisted recombination in thermally co-evaporated solar cells based on the archetypal MAPI perovskite. First, I present the status quo of typical solar cells investigated in this thesis. To study the source of the voltage losses, I employ PLQY measurements, comparing the bare perovskite film with the complete device to isolate the bulk contribution. To ensure a meaningful comparison, surface recombination on the film sample must be excluded, which I verify exploring the impact of a multitude of different reported passivation agents and additionally by testing the surface recombination via TRPL measurements. Potential $V_{oc}$ improvements are simulated assuming either perfect bulk or interface passivation.

Unlike the behavior typically observed in solution-processed perovskites, we find that trap-assisted recombination in thermally co-evaporated solar cells is not predominantly associated with the interfaces to the CTLs. Instead, the bulk quality of co-evaporated perovskites is equally limiting the $V_{oc}$. Such a dual contribution, uncommon in state-of-the-art solution-processed perovskite solar cells, must be carefully considered prior to device optimization, as it results in minimal improvement of the *JV* curve when addressing non-radiative recombination in isolation. Consequently, the exclusive reliance on *JV* curve analysis, a common practice in optimization processes, is insufficient and may impede significant advancements in vacuum-processed perovskite solar cells. I recommend adopting a combined characterization strategy, incorporating PL measurements of both the perovskite film and the complete device, in addition to the *JV* curve. Such a dual characterization protocol provides a straightforward and accessible method for many laboratories to distinguish between bulk and interface recombination contributions, thus

enabling the detection of material improvements during device optimization. Importantly, this strategy is not limited to co-evaporated perovskites with moderate PCE but is equally relevant for all solar cell types once interfaces optimization has reached the perovskite bulk limit.

## 5.2 Results and Discussion

### 5.2.1 Status-Quo of co-evaporated perovskite solar cells

I investigate perovskite solar cells prepared by thermal evaporation using a planar *n-i-p* configuration, which consists of ITO/$SnO_2$/$C_{60}$ and TaTm/TPBi/$MoO_3$/Ag as electron- and hole- extraction contacts, as previously reported by our group and further explained in Chapter 2.1.[218]

Figure 5.1a provides the cross-sectional SEM image of a typical device. The MAPI film exhibits a heterogeneous morphology containing multiple crystal grain sizes, some column-like with a length of about 300 – 400 nm, others smaller than 100 nm. This implies that during extraction, charge carriers need to pass several grain boundaries in the vertical direction, increasing the probability of recombining at trap centers and causing losses.

An example of a typical *JV* curve of a co-evaporated MAPI solar cell is shown in Figure 5.1b (see the statistics of the parameters in Figure 5.4c). The $V_{oc}$ is with 1.13 V higher than the average reported value for solution-processed MAPI solar cells of 1.09 V, (extracted from the Perovskite Database, data from 01/2014 until 01/2021, PCE > 18 %),[215] where larger crystal grains are usually reported.[197,198] A $V_{oc}$ of 1.13 V is, however, significantly below than the radiative limit for a solar cell based on MAPI. It is therefore important to understand the origin of the $V_{oc}$ losses in co-evaporated perovskite cells and identify means to reduce them.

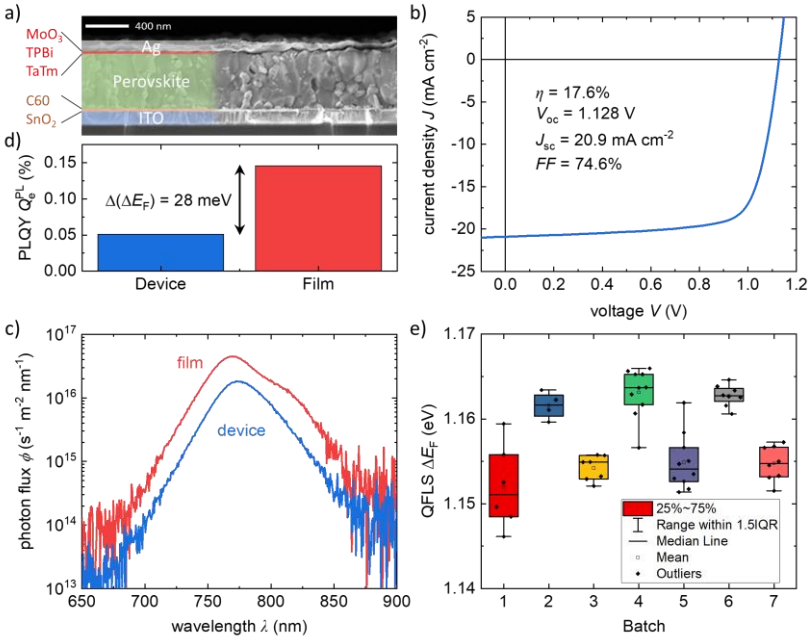


Figure 5.1 a) Cross-sectional SEM image of a typical co-evaporated *n-i-p* MAPI solar cell. b) *JV* curve of the solar cell with *JV* parameters. c) PL spectra, calibrated to absolute photon numbers, and d) PLQY comparison between a complete device and glass/perovskite film under 1-sun equivalent illumination. The corresponding difference in QFLS is indicated. e) In-batch and batch-to-batch variations of the QFLS of co-evaporated MAPI films on glass.

To investigate the sources of the $V_{oc}$ losses, I performed PLQY measurements as described in Chapter 2.3.2. The non-contact nature of this technique allows for the probing of either a single layer sample or a combination of layers, enabling selective inspection of potential recombination centers in a complete device. I performed a comparative analysis of the PLQY for the perovskite film deposited on glass and for the entire device. The prior represents the limiting case in which recombination is only happening in the perovskite bulk, considering that recombination at the interfaces with glass and $N_2$ can be neglected (later verified in section 5.2.2). To enhance readability, I will refer to the parameters measured on the film on glass with the subscript "film" and to the parameters measured on the complete device with the subscript "device". Note that the $V_{oc}$ is always measured on the complete device.

Assuming that the reciprocity relation is fulfilled,[219] the PLQY directly relates to the quasi-Fermi level splitting via Equation (1.36). The QFLS refers to the splitting of the quasi-Fermi levels of the electrons and holes in the perovskite bulk and corresponds to $qV_{oc}$ when measured on the complete device with aligned band energies.[191]

We first consider a MAPI film fabricated by thermal co-evaporation on top of a glass substrate and compare it to the film embedded in a complete device architecture. Figure 5.1c shows the PL spectra of both under 1 sun AM1.5G-equivalent illumination. From these, the PLQY was estimated, as detailed in Chapter 2.3.2 and illustrates in Figure 5.1d. Following Equation (1.36), a value of $Q_e^{PL}{}_{film} = 0.146\%$ corresponds to $\Delta E_{F,film} = 1.157$ eV, and $Q_e^{PL}{}_{device} = 0.051\%$ corresponds to $\Delta E_{F,device} = 1.130$ eV, with a reasonable agreement to the $V_{oc} = 1.128$ V. The reproducibility, influenced by the fabrication of MAPI films, the homogeneities of the films and the uncertainties of the measurement, are shown in Figure 5.1e.

According to the literature, the passivated free standing perovskite films (that is glass/perovskite film exposed to $N_2$) are generally more luminescent than the complete devices.[37,96,191,194,199–207] In that case, the $V_{oc}$ losses are indeed dominated by recombination at the CTLs interfaces. However, this is mostly reported for solution-processed perovskites. In our co-evaporated MAPI films, we observe only a slight difference in PLQY (factor of 3) between free-standing MAPI films and the completed solar cells. The observed difference would correspond to a small voltage reduction of about 0.028 V (see Figure 5.1c and d).

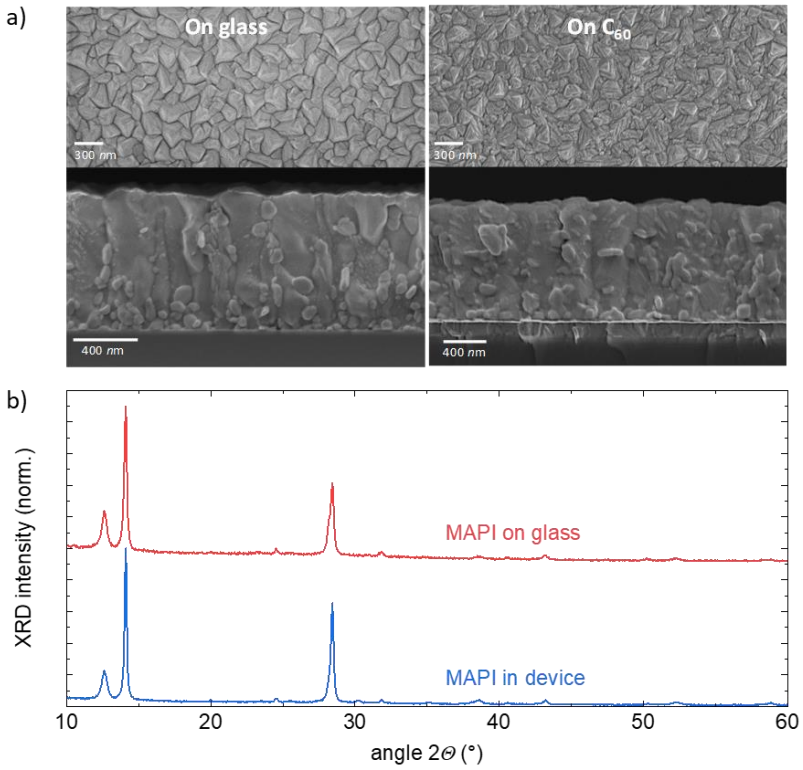


Figure 5.2 a) SEM images (top and cross-section) of MAPI films deposited on glass and ITO/$SnO_2$/$C_{60}$ substrates. b) XRD patterns of MAPI films deposited on glass and inside the device architecture.

Assuming that the $Q_e^{PL}{}_{film}$ can be seen as the limit of solely bulk recombination in the device, the small difference between $Q_e^{PL}{}_{film}$ and $Q_e^{PL}{}_{device}$ can indicate a bulk limitation of the $V_{oc,}$, assuming that the perovskite film morphology and crystallization is the same in both samples. I verified this by comparing the XRD patterns and film morphology via top- and cross-sectional SEM images, as shown in Figure 5.2.

However, $\Delta E_{F,film}$ may deviate from the actual bulk limit, if the perovskite-air interface contain undefined energy states, which differ from the interface states present in the completed solar cell. Given that high surface recombination velocities $S$ may reduce $Q_e^{PL}{}_{film}$, causing it to deviate from the bulk limit in the device, it is crucial to measure $Q_e^{PL}{}_{film}$ in a manner that minimizes the influence of surface recombination effects, allowing for a more accurate assessment of the bulk properties of the film material.

Table 5.1 List of the passivation agents used with abbreviation, full name, structural formula and reference. $D_P$ is the degree of polymerization of the polymer.

| **Abbreviation** | **Full name** | **Structural formula** | **Reference** |
|---|---|---|---|
| PEAI | Phenethylammonium iodide | $C_6H_5(CH_2)_2NH_3I$ | [207] |
| ChAI | Cyclohexylammonium iodide | $C_6H_{11}NH_3I$ | [220] |
| 4F-BzAI | 4-Fluoro-Benzylammonium iodide | $FC_6H_4CH_2NH_3I$ | [221] |
| ChMAI | Cyclohexylmethylammonium iodide | $C_6H_{11}CH_2NH_3I$ | [222] |
| BzAI | Benzylammonium iodide | $C_6H_5CH_2NH_3I$ | [223] |
| GuaI | Guanidinium iodide | $C(NH_2)_3I$ | [224] |
| 1,4-BzDAI | 1,4-Benzene diammonium iodide | $C_6H_4(NH_3)_2I_2$ | [225] |
| TP6 | Tetrabutylammonium hexafluorophosphate | $NC_{16}H_{36}PF_6$ | [226] |
| PEO4000 | Polyoxyethylene, $D_P$ = 4000 | $H(OCH_2CH_2)_{4000}OH$ | |
| TOPO | Trioctylphosphine oxide | $OP(C_8H_{17})_3$ | [34] |
| PEO10000 | Polyoxyethylene, $D_P$ = 100000 | $H(OCH_2CH_2)_{10000}OH$ | |
| PMMA | Poly(methyl methacrylate) | $(CH_2CCH_3COOCH_3)_n$ | [227] |
| OPA | Octylphosphonic acid | $CH_3(CH_2)_7PO_3H_2$ | [228] |
| PEO600k | Polyoxyethylene, $D_P$ = 600000 | $H(OCH_2CH_2)_{600000}OH$ | |
| PEO6M | Polyoxyethylene, $D_P$ = 6000000 | $H(OCH_2CH_2)_{6000000}OH$ | [229] |
| APTMS | (3-aminopropyl) trimethoxysilane | $H_2N(CH_2)_3Si(OCH_3)_3$ | [230] |
| $Al_2O_3$ | Aluminum oxide | $Al_2O_3$ | [231] |
| Hex | Hexane | $CH_3(CH2)_4CH_3$ | |
| tBOHTH | tert-butanol:Toluene:Hexane, 4:1:1 | $(CH_3)_3COH : C_6H_5CH_3 : CH_3(CH_2)_4CH_3$ | |
| CB | Chlorobenzene | $C_6H_5Cl$ | |

### 5.2.2 Analysis of surface recombination on the perovskite film on glass

Surface recombination of charge carriers is often minimized by coating the perovskite with wide-bandgap interlayers or passivating molecules. It has been shown that $Q_e^{PL}{}_{film}$ in solution-processed perovskites can improve by such a treatment with passivation agents (up to a $\Delta E_{F,film}$ increase of 86 meV).[194] We applied a series of frequently-used passivation

agents (see Table 5.1) on the pristine perovskite surface and measured the $Q_e^{PL}{}_{film}$ additionally to a non-treated sample as reference. The passivation agents range from cations enabling the formation of low-dimensional perovskites, to ionic liquids, metal oxides and Lewis bases. The experimental $Q_e^{PL}{}_{film}$ data were then used to calculate the $\Delta E_{F,film}$ via Equation (1.36), where the bandgap $E_g$ was assumed to be constant to evaluate only the PLQY. Figure 5.3a shows the $\Delta E_{F,film}$ improvement for the different glass/MAPI/passivation layer stacks, compared to the un-passivated MAPI film on glass. Note that 1,4BzDAI and $PEO_{6M}$ could not be properly dissolved, while APTMS destroyed the perovskite immediately. As shown, $\Delta E_{F,film}$ exhibits only marginal improvements even with the most effective passivating molecules. Indeed, when considering the measurement uncertainty given by batch-to-batch variations I feel these changes are almost negligible (Figure 5.1e). This lack of $\Delta E_{F,film}$ improvement indicates that the open perovskite surface plays a minor role in the total recombination of the film. We additionally tested the solvents that were used to coat some of the passivating molecules, which have a minor detrimental effect on $\Delta E_{F,film}$.

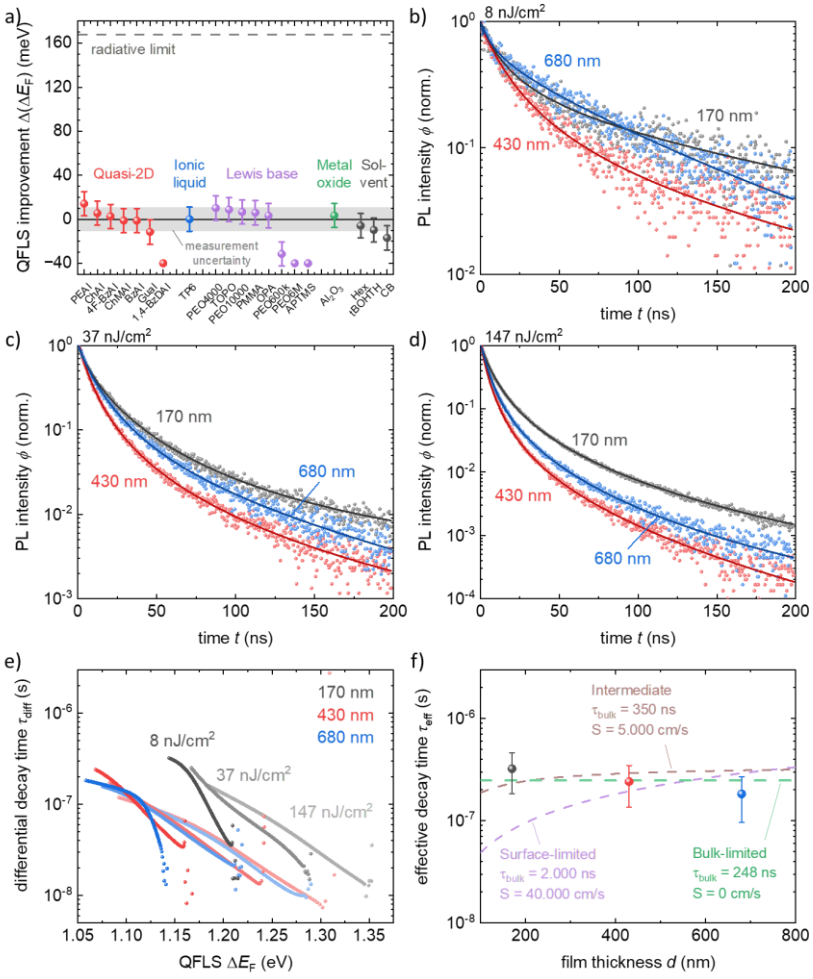


Figure 5.3 a) Overview of the improvement in QFLS $\Delta E_{F,film}$ in MAPI films on glass due to different passivation agents in comparison to the pristine MAPI film. The grey dashed line represents the improvement needed to reach the radiative limit. The colors indicate the material classes. The error is based on the measurement uncertainty given by spot-to-spot, sample-to-samples and batch-to-batch variations of the $Q_e^{PL}{}_{film}$. Dysfunctional agents are marked at -40 meV without error bars. The abbreviations are explained in Table 5.1. b)-d) TRPL transients of MAPI films of different thicknesses on quartz illuminated with laser fluences of b) 8 nJ cm$^{-2}$, c) 37 nJ cm$^{-2}$ and d) 147 nJ cm$^{-2}$. The light dots show the experimental data; the solid lines show the fits of 4$^{th}$-order rational functions done to reduce the noise to determine the differential decay time. e) The differential decay time, extracted from the fits, as a function of the QFLS of the three different thicknesses at the three

fluences. The upper envelope at the different fluences describes the recombination lifetime while the steep tails of each curve are influenced by drift and diffusion. f) Effective decay times of MAPI films extracted from e as the differential decay time at the lowest $\Delta E_{F,film}$ measurable. The lines show the theoretical behavior of Equation 2 with different bulk lifetimes and surface recombination velocities. The blue line is the fit of the experimental data indicating no surface recombination. The black line displays a behavior in the case of a film that is limited by surface recombination. The red dashed line represents an intermediate situation. The error bars are based on the error propagation of the measurement uncertainty of the ${Q_e}^{PL}{}_{film}$ and the fitting error of the TRPL decays.

Another experiment to test regarding surface recombination is TRPL on films with different film thicknesses. For weakly-doped materials such as perovskites,[31] the charge-carrier lifetime depends on the charge-carrier concentration inside the film, and thereby on $\Delta E_{F,film}$.[53,232] Shallow traps, radiative and Auger recombination lead to shorter lifetimes for higher $\Delta E_{F,film}$. Only if deep traps dominate the charge carrier recombination in a film, the effective PL decay time will be constant at low $\Delta E_{F,film}$, which is reached at long delay times after the excitation pulse, and a mono-exponential decay is observed. Using Equations (1.29) and (1.30) and assuming that the diffusion is not the limiting process, the lifetime can be expressed via[232]

$$\tau_{eff} = \frac{1}{\frac{1}{\tau_{bulk}} + \frac{S}{2d}}. \tag{5.1}$$

The effective lifetime has two contributions, one from the perovskite bulk with the bulk carrier lifetime $\tau_{bulk}$ and one from the recombination at the surfaces, which scales with the surface recombination velocity $S$ and the thickness of the film $d$. That means that, if the carrier recombination in the glass/perovskite sample is dominated by surface recombination, a thin film will have a shorter carrier lifetime than a thick film. In contrast, the lifetime of carriers will be constant if bulk recombination is dominant. To identify which situation occurs in the co-evaporated MAPI films, collaborateurs performed TRPL measurements with varying laser fluence. MAPI films of different thickness (170, 430 and 680 nm) deposited on glass substrates were fabricated (see Chapter 2.1) and measured by our collaborators. The resulting decay curves are shown in Figure 5.3c-d.

For the data analysis, rather than fitting the curves by a predefined decay function imposing a specific recombination model, I employed a 4$^{th}$-order rational function, offering sufficient flexibility to accurately represent the data. This approach was primarily intended to reduce

noise, as the subsequent calculation of differential decay times as a function of $\Delta E_{F,film}$ relies on the derivative of the data, where noise would be detrimental.[37] The $\Delta E_{F,film}$ directly after the excitation pulse is given by the laser fluence, and afterwards it decays with the logarithm of the relative PL intensity at the delay time $t$ in comparison to time zero, $\Delta E_F = kT \ln[\phi(t)/\phi(t=0)]$. The differential decay time can be obtained with the derivative of the decay curve via $\tau_{diff} = -2(d\ln(\phi)/dt)^{-1}$.

Figure 5.3e shows the $\tau_{diff}(\Delta E_{F,film})$ curves of all samples and all fluences overlayed. For each sample, the curves using different laser fluences should overlap for recombination mechanisms. However, at short times after the pulse, which corresponds to high $\Delta E_{F,film}$ of each curve, drift-diffusion effects shorten the differential decay time leading to tails in Figure 5.3e (as indicated in Figure 1.7b). To avoid these effects, the upper envelope of the curves (the highest $\tau_{diff}$ at a given $\Delta E_{F,film}$) must be taken into consideration. The differential decay time $\tau_{diff}$ decreases with rising $\Delta E_{F,film}$ as one would expect from radiative recombination, shallow traps or Auger recombination. At low $\Delta E_{F,film}$ values, $\tau_{diff}$ starts to exhibit a flatter behavior, indicating a deep trap, for which the lifetime $\tau_{eff}$ is defined by Equation (5.1). I note that the observable range of $\Delta E_{F,film}$ is limited by measurement noise, so that the differential decay time in Figure 5.3e does not yet fully saturate.

Therefore, I use the highest measurable decay time as $\tau_{eff}$ while pointing out that the real lifetimes are likely higher which might distort the data analysis. To check the influence of surface recombination on the samples, the extracted decay times are plotted as a function of the film thickness in Figure 5.3f. The dashed lines show the thickness-dependent behavior of $\tau_{eff}$ following Equation (5.1) under three cases, where different hypothetical $\tau_{bulk}$ and $S$ conditions are assumed for a surface: a bulk-limited and an intermediate case. The experimental values show the opposite behavior of what would be expected from a surface-recombination-dominated film, with 320, 241 and 182 ns for the 170, 430 and 680 nm thick films, respectively. While I cannot assert these values as definitive recombination lifetimes of a deep trap, the trend suggests that recombination in the bulk predominantly influences the decay process. This observation supports the conclusions drawn from the passivation study depicted in Figure 5.3a.

I can therefore conclude that trap-assisted surface recombination does not considerably quench the PL of co-evaporated free-standing perovskite films, which implies that the ${Q_e}^{PL}{}_{film}$ is limited by recombination processes in the bulk of the film. The similarity in the

obtained $Q_e^{PL}{}_{film}$ and $Q_e^{PL}{}_{device}$ (Figure 5.1d) suggests then that also the $V_{oc}$ of the device, which has different interfaces than the free-standing film, is at least partly limited by charge-carrier recombination in the bulk, and therefore, improvements due to interface passivation will likely be insignificant in $V_{oc}$.

### 5.2.3 Device simulations

To get further insight into the limitations of our co-evaporated MAPI films and their effect on device performance, I simulated how the *JV* curve would change with either perfect bulk or perfect interface passivation. I established a drift-diffusion device model by globally fitting the experimental *JV* curve together with pseudo-*JV* curves constructed from light-intensity dependent data, namely the Suns-$V_{oc}$ and the Suns-$\Delta E_{F,film}$ curve.[194]

The Suns-$V_{oc}$ curve can be obtained by measuring the $V_{oc}$ of the device at different light-intensities (see Figure 5.4b), converting the light intensity to the current density (where the 1-sun intensity corresponds to the short-circuit density $J_{sc}$ at 1 sun) and subtracting $J_{sc}$ under 1 sun to shift the curve into the fourth quadrant. Figure 5.4c shows the resulting pseudo-*JV* curve. Given that at OC conditions no charge is extracted, the *FF* of the pseudo-*JV* curves is only limited by non-radiative recombination and shunt resistance. Therefore, the difference between the measured *JV* curve and the Suns-$V_{oc}$ curve is attributed to substantial transport issues, which lead to an absolute PCE loss of 2.3% (Figure 5.4e). This method is similar to the one introduced in Chapter 4 of plotting $J_{extr}(\Delta E_{F,device})$, with minor differences. The Suns-$V_{oc}$ method does not account for current losses due to recombination under SC conditions and diverges from the method of Chapter 4 if the energy bands in the device are misaligned, such that $V_{oc} \neq \Delta E_{F,device}$. In this chapter, I am less concerned with transport properties and have established that $V_{oc} = \Delta E_{F,device}$. Therefore, I employ the Suns-$V_{oc}$ method due to its practical ease of measurement.

The Suns-$\Delta E_{F,film}$ curve can be obtained in a similar way as the Suns-$V_{oc}$ curve by determining the $\Delta E_{F,film}$ from the $Q_e^{PL}{}_{film}$ of the free-standing perovskite film at different light-intensities (see Figure 5.4a and b). The Suns-$\Delta E_{F,film}$ curve provides the efficiency potential in the absence of interface limitations with the CTLs, thus the bulk-recombination limit with perfect transport. Both pseudo-*JV* curves are rather similar to each other (see Figure 5.4c), and due to transport losses considerately better than the measured *JV* curves.

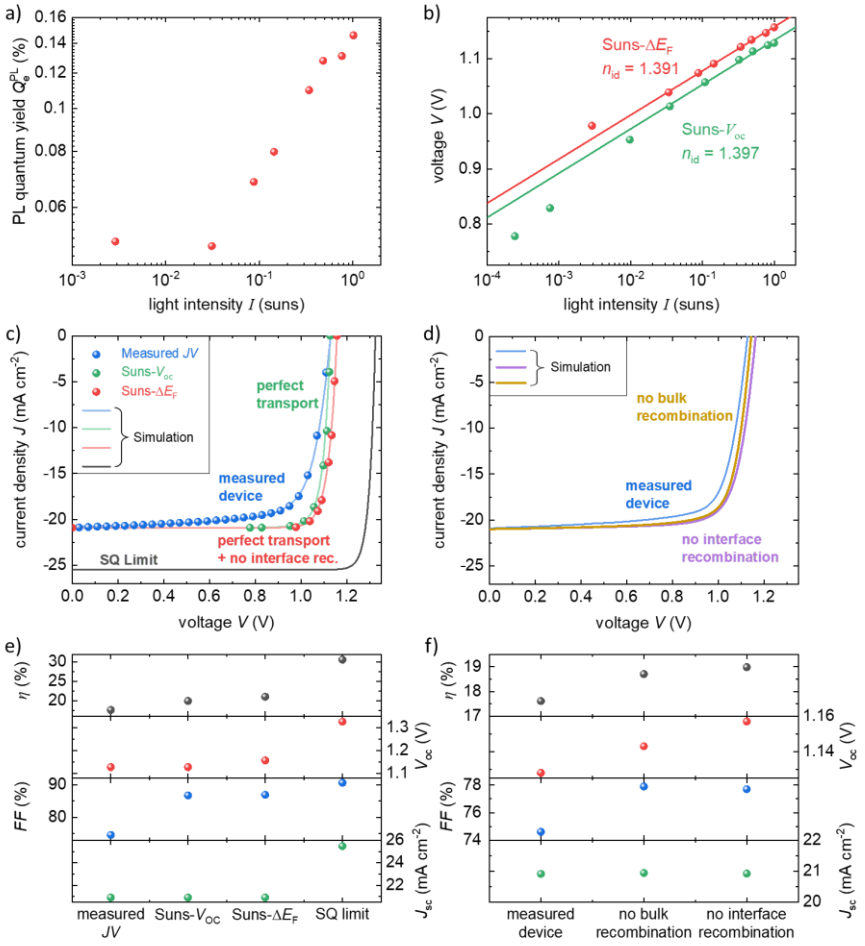


Figure 5.4 a) PLQY as a function of light intensity in suns. b) $\Delta E_{F,film}$, calculated from the data from a), and $V_{oc}$ as a function of light intensity in suns. The ideality factor $n_{id}$ was determined by fitting the part of high light intensities (above 0.03 suns). c) Measured *JV*, Suns-$V_{oc}$, and Suns- $\Delta E_{F,film}$ data obtained from MAPI devices and MAPI films deposited on glass are indicated by spheres. The solid lines represent the simulated global fits for each situation. d) Simulated curves for the measured *JV* (same as *measured device* in c)), as well as for the limits of absent bulk or absent interface recombination, while maintaining transport limitations. e)-f) Comparison of the photovoltaic parameters obtained e) from the curves in b), and f) from the curves in d).

From the above findings one could conclude that the interfaces with the CTLs introduce little additional recombination and that reducing the perovskite bulk traps might lead to high $V_{oc}$ values. To examine this, I created a device model using the 1D drift-diffusion

simulator SIMsalabim[125] by fitting the *JV* and pseudo-*JV* curves together with the SQ limit for a bandgap of 1.6 eV (see solid lines in Figure 5.4c). As starting point for the fitting procedure, the device model used well-known parameters for $MAPbI_3$ and the CTLs from the literature (see Table 5.2) to fit the SQ limit assuming perfect transport and zero non-radiative recombination.[27] The only parameter that was free for fitting was the radiative recombination constant $k_{rad}$ which resulted in a realistic value in comparison to literature.[124,233–235] To avoid charge transport problems, very thin CTLs with high doping concentrations were assumed. Having the model for the SQ limit enables to fit the Suns-$\Delta E_{F,film}$ curve which is shown in Figure 5.4c and represents the limit of perfect transport and only bulk recombination. Assuming that the main recombination source in the bulk was at the grain boundaries,[196,197] the number of grain boundaries and their trap density were fitted. The curve was also fitted once including bulk traps, but the resulting density was so low ($N_T$ = 2.8 x $10^{-4}$ $cm^{-3}$) that it was fixed to zero. The capture coefficients and trap energy level were shared parameters with the surface traps and were fitted in this step together with the doping density of the CTLs to ensure a good agreement with the pseudo-FF. At this point an asymmetry was introduced in the capture coefficients between electrons and holes as literature values suggest this imbalance.[236] After modeling the bulk recombination limit, it was proceeded to fit the Suns-$V_{oc}$ curve by adjusting the interface trap density, the band alignment, and the doping density of the CTLs, using the real CTLs thicknesses. The obtained values, listed in Table 5.2, gave a very good fit to the data points (Figure 5.4c), indicative of a good model adjustment. Moreover, the *JV* curve was additionally fitted with transport parameters close to literature values (cited in Table 5.2), which lead to a good fit of the experimental curve (solid gray line in Figure 5.4c).

I then used this model and parameter set to simulate *JV* curves, in which the recombination of either the bulk or the interfaces is removed (Figure 5.4d and f). These are limiting cases in which either the bulk or the interfaces were optimized experimentally. Note that the limit of only bulk recombination is different from the Suns-$\Delta E_{F,film}$ curve, as it still includes the transport limitations assumed in the model. Importantly, both simulated limits, bulk and interface recombination, are surprisingly similar, and closely resemble the experimental *JV* curve. While the $V_{oc}$ is slightly higher when only bulk recombination is present, the efficiency of both is nearly identical and only about 1.5% higher than the measured curve. These observations indicate that both the bulk and the interface recombination are equally limiting the devices, which implies that isolated improvements in one of them will be

difficult to detect as the resulting *JV* curves will be very similar. In other words, in a typical experiment involving the modification of either the CTLs or the perovskite bulk, even significant improvements will have minimal effects on the resulting *JV* curves. Besides, if the improvement is small, it might be hidden in measurement uncertainties, hampering any device optimization. This dual contribution, unusual in the current state of solution-processed perovskites, hinders advancement in co-evaporated perovskite solar cells.$\mu_n$

Table 5.2 Parameters for the simulation. For parameters without specified numerical values, those listed on the left-hand side are applied. When a value is attributed to both a fit and a reference, the reference served as the initial estimate. References [a] and [b] correspond to References [237] and [236] in the bibliography, respectively.

| **General** | | **SQ limit** | **source** | **Suns-$\Delta E_F$** | **source** | **Suns-$V_{oc}$** | **source** | **Full device** | **source** |
|---|---|---|---|---|---|---|---|---|---|
| Temperature | K | 295 | | | | | | | |
| device thickness | m | $5.02\times10^{-7}$ | | | | $5.22\times10^{-7}$ | | | |
| relative permittivity perovskite | | 24.1 | ref [a] | | | | | | |
| conduction band perovskite | eV | 3.84 | ref [b] | | | | | | |
| valence band perovskite | eV | 5.44 | ref [b] | | | | | | |
| density of state | $m^{-3}$ | $3.10\times10^{24}$ | ref [b] | | | | | | |
| **Mobilities** | | | | | | | | | |
| electron mobility perovskite | $m^2 V^{-1} s^{-1}$ | 1 | very high | | | | | $1.01\times10^{-4}$ | fit [b] |
| hole mobility perovskite | $m^2 V^{-1} s^{-1}$ | 1 | very high | | | | | $2.97\times10^{-4}$ | fit [b] |
| **Contacts** | | | | | | | | | |
| work function electrode HTL | eV | 3.84 | perfect alignment | | | 3.869 | fit | | |
| work function electrode ETL | eV | 5.44 | perfect alignment | | | 5.364 | fit | | |
| shunt resistance | Ω | -1 | infinite shunt | | | $1.07\times10^{8}$ | fit | 0.332 | fit |
| series resistance | Ω | 0 | no series resistance | | | | | $1.86\times10^{-4}$ | fit |
| **Transport** | | | | | | | | | |
| thickness C60 | m | $10^{-9}$ | very thin | | | $1.2\times10^{-8}$ | device stack | | |
| thickness TaTm | m | $10^{-9}$ | very thin | | | $1.0\times10^{-8}$ | device stack | | |
| p-doping density C60 | $m^{-3}$ | $-10^{25}$ | very high | $-3.69\times10^{25}$ | fit | $-7.24\times10^{24}$ | fit | | |
| p-doping density TaTm | $m^{-3}$ | $10^{25}$ | very high | $3.69\times10^{25}$ | fit | $2.54\times10^{23}$ | fit | | |
| mobility C60 | $m^2 V^{-1} s^{-1}$ | 1 | very high | | | | | $2.47\times10^{-6}$ | fit [b] |
| mobility TaTm | $m^2 V^{-1} s^{-1}$ | 1 | very high | | | | | $2.14\times10^{-7}$ | fit [b] |
| relative permittivity C60 | | 3.9 | ref [b] | | | | | | |
| relative permittivity TaTm | | 3 | ref [b] | | | | | | |
| conduction band C60 | eV | 3.84 | perfect alignment | | | 3.868 | fit | | |
| conduction band TaTm | eV | 2 | high blocking | | | 2.225 | $VB_{TaTm}$-3.14 | | |
| valence band C60 | eV | 7 | high blocking | | | 6.208 | $CB_{C60}$+2.34 | | |
| valence band TaTm | eV | 5.44 | perfect alignment | | | 5.365 | fit | | |
| **Generation** | | | | | | | | | |
| generation rate | $m^{-3} s^{-1}$ | $3.18\times10^{27}$ | calculated from Jsc = 25.47 mA/cm2 | | | | | | |
| fraction of absorbed light | | 1 | | 0.821 | fit | | | | |
| radiative recombination constant | $m^3 s^{-1}$ | $1.60\times10^{-17}$ | fit | | | | | | |
| **Trapping** | | | | | | | | | |
| bulk trap density | $m^{-3}$ | 0 | | 0 | fit | | | | |
| surface trap density C60 | $m^{-2}$ | 0 | | | | $8.23\times10^{14}$ | fit | | |
| surface trap density TaTm | $m^{-2}$ | 0 | | | | $6.21\times10^{8}$ | fit | | |
| number grain boundaries | | 0 | | 2 | fit | | | | |
| grain boundary trap density | $m^{-2}$ | 0 | | $1.29\times10^{13}$ | fit | | | | |
| capture coefficient electrons | $m^3 s^{-1}$ | 0 | | $2.02\times10^{-13}$ | fit [b] | | | | |
| capture coefficient holes | $m^3 s^{-1}$ | 0 | | $6.77\times10^{-14}$ | fit [b] | | | | |
| trap energy level | eV | 0 | | 4.64 | | | | | |

### 5.2.4 $V_{oc}$ optimization cycle

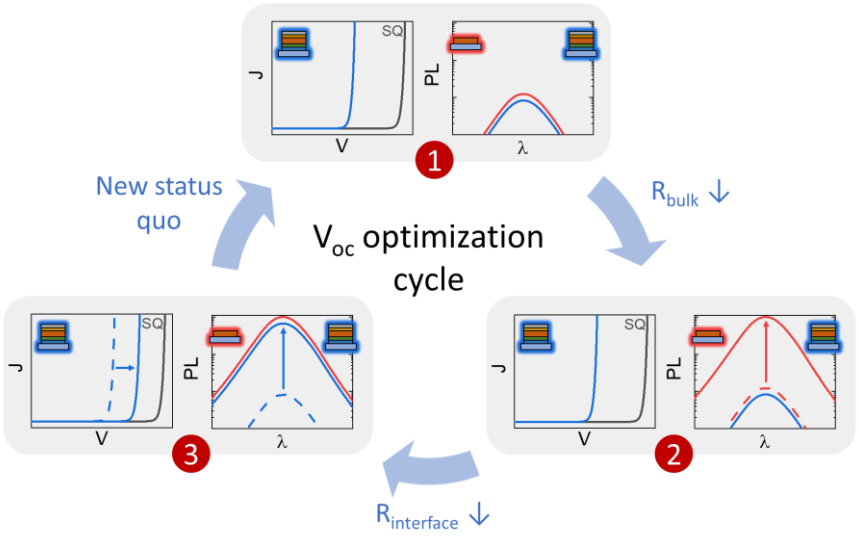


Figure 5.5 Proposed cycle for $V_{oc}$ optimization. 1) corresponds to a situation where the PLQY of the film is close to that of the device, hence the bulk of the film should be improved. This leads to situation 2) where $Q_e^{PL}{}_{film}$ is increased but the $V_{oc}$ of the device remains approximately constant. In step 3), the interface recombination is reduced leading to an increase in $Q_e^{PL}{}_{device}$ and $V_{oc}$. Situation 3) is an improved situation 1), from where the optimization cycle restarts.

To address this challenge, I propose a facile and accessible strategy for $V_{oc}$ optimization based on the combined PL and *JV* measurements using two samples, the perovskite film on glass and the corresponding complete device, incorporating that same film (as illustrated in Figure 5.5). This is a cycle in which any perovskite solar cell takes part, independent of the performance. A critical step, often overlooked in device-optimization literature, is comparing the PL of the perovskite film with that of the complete device. For the PL of the film sample, it is assumed that proper care is taken that the surface recombination of the film is minimized, so that the measurement represents the bulk limit.

I start illustrating this PL and *JV* cycle with the situation found here in the co-evaporated MAPI film and solar cell (1 in Figure 5.5): The device is so far optimized that it shows a diode-like rectification in the *JV* curve, and the PL peak of the perovskite film is only slightly more intense than the luminescence peak of the complete device. In this situation, bulk and interface recombination contribute equally to limiting the device $V_{oc}$. I propose

that the first step should be to focus on reducing the traps in the perovskite bulk to enhance the PLQY of the film (leading to 2 in Figure 5.5). Simultaneously, the *JV* of the device should be monitored to ensure that the electronic properties of the perovskite are not compromised. In this first optimization step, significant changes in $V_{oc}$ are not expected, as interface recombination likely remains constant and therefore now limiting. However, changes in bulk properties might indirectly affect interface recombination, leading to observable *JV* curve variations, including potential $V_{oc}$ increases or even reductions.

After a successful first optimization step, the film is considerably more luminescent than the device and the next step is to reduce the interface recombination. This is the current state in many solution-processed perovskites. In this situation, it is helpful to primarily identify the limiting interface of the device via PL measurements on half-stacks as discussed extensively before.[96] Once the limiting of the two interfaces is determined, the improvement of this interface will directly lead to a change in the *JV* curve, and thus to an increase in $V_{oc}$ (3 in Figure 5.5). When both interfaces are optimized to the point of little quenching, further enhancements become less noticeable, necessitating the restart of the cycle.

I want to point out that this iterative process can be applied at any stage of the solar cell optimization with the condition that the PL of both samples can be measured and that the device shows a diode-like *JV* curve. By systematically improving bulk and interface properties, this method enables targeted $V_{oc}$ enhancements and accelerates device optimization.

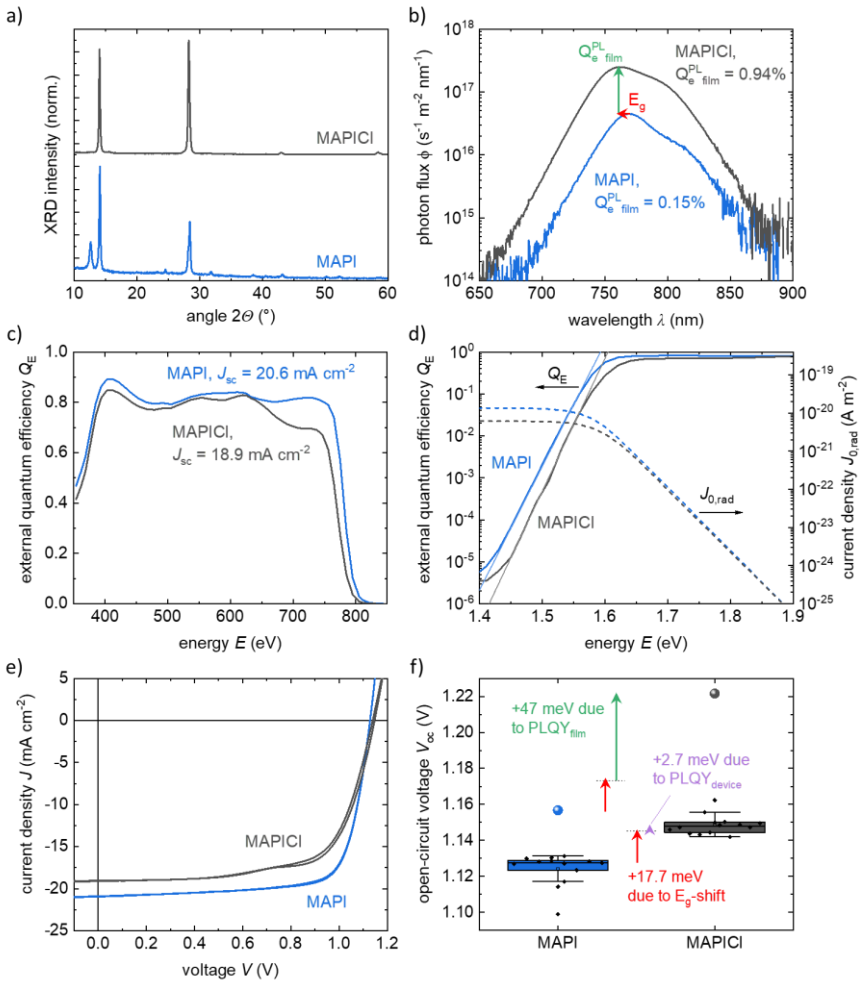


Figure 5.6 a) XRD of a MAPI film and a MAPICl film on glass. b) PL emission spectra of MAPI and MAPICl films on glass, showing a bandgap $E_g$ shift of 19 meV and a $Q_e^{PL}{}_{film}$ increase by a factor of 6.3 corresponding to a total $\Delta E_{F,film}$ increase of 65 meV. c) EQE of both devices in linear scale as function of the wavelength with integrated $J_{sc}$ values. d) The same EQE data in semi-logarithmic scale as function of the energy. The integrated dark saturation current density $J_{0,rad}$ for both devices is plotted on the right axis. e) Measured $JV$ curves of MAPI and MAPICl based solar cells. f) Comparison of the $V_{oc}$ between the devices. The arrows indicate the contribution of the bandgap shift, the $\Delta E_{F,film}$ improvement due to $Q_e^{PL}{}_{film}$ and the $\Delta E_{F,device}/V_{oc}$ improvement in the device due to $Q_e^{PL}{}_{device}$. The spheres correspond to the measured $\Delta E_{F,film}$.

I present an experimental example of Step 1) in the device optimization process. MACl is a material prevalently reported in the literature known to enhance the bulk properties of perovskite films by passivating deep-level traps at grain boundaries.[198,238] To evaluate its effect, MACl was incorporated into the co-evaporation process of MAPI as discussed in Chapter 2.1. This addition did not negatively impact film growth, as the resulting perovskite retained the tetragonal phase of MAPI (Figure 5.6a). The incorporation of MACl leads to a small increase in the bandgap of 19 meV, as can be observed from the PL peak and the external quantum efficiency spectrum in Figure 5.6b and Figure 5.6c, respectively. This shift in the bandgap is an inevitable effect of chloride incorporation into the crystal structure and leads to a shift in the $V_{oc,rad}(E_g)$.

Figure 5.6b shows the PL spectra, expressed in absolute values, obtained for the MAPI and MAPICl films. Notably, ${Q_e}^{PL}_{film}$ of the MAPICl film is significantly enhanced, being six times higher than that of the MAPI film. This improvement corresponds to a $\Delta E_{F,film}$ increase of 47 meV. Combined with the 19 meV bandgap increase, this results in a total $\Delta E_{F,film}$ increase of ~ 66 meV for MAPICl relative to MAPI.

However, the *JV* curve of MAPICl in Figure 5.6e reveals only a modest small improvement in $V_{oc}$ (20 mV, Figure 5.6f), which is much lower than the $\Delta E_{F,film}$ increase and is mainly caused by the shift in bandgap. This discrepancy, wherein substantial bulk recombination reduction yields only a minor impact on $V_{oc}$, aligns well with our simulations for MAPI-based solar cells. From this point, ideally further bulk optimization would be pursued, or attention could shift to interface analysis. A detailed investigation of interface contributions, however, lies beyond the scope of this work.

## 5.3 Conclusion

In summary, with the aid of PL measurements, pseudo-*JV*, *JV* curves and device simulations I have demonstrated that in co-evaporated MAPI perovskite solar cells the interface and bulk charge carrier recombination are both limiting the $V_{oc}$. When this is the case, the typical characterization of the solar cell solely based on *JV* curves may conceal improvements in material quality, which plausibly hinders device optimization. To advance in these circumstances, I emphasize the use of PL comparisons between film and device, additionally to *JV* measurements, as basic characterization protocol, opening new possibilities for performance improvements. I demonstrate our predictions and a first step

of the procedure for co-evaporated MAPI films that include a small amount of MACl, which leads to significant increases in the $Q_e^{PL}{}_{film}$ but to a small increase in the $V_{oc}$ of the device. Importantly, our methodology is applicable (and should be applied) to any perovskite optimization process, as it also applies for non-optimal perovskite compositions/ novel fabrication methods (limited by both bulk and interface recombination), or even for those works using highly efficient cells once the interfaces are sufficiently improved, and the $V_{oc}$ of the device approaches the QFLS of the film.

# 6 Conclusions

The aim of this thesis was to identify the key loss mechanisms in co-evaporated perovskite solar cells, which lack fundamental characterization compared to solution-processed counterparts. In a comprehensive analysis, I began from a broad investigation in Chapter 3 and progressively delved into more detailed studies in Chapters 4 and 5.

In **Chapter 3**, I analyzed efficiency losses in co-evaporated perovskite solar cells by dissecting the *JV* parameters $V_{oc}$, $J_{sc}$, and *FF*. I found for four different perovskite formulations, that all three parameters contributed equally to performance losses, indicating the need for a thorough analysis of each. Using sensitive EQE measurements, I decomposed the $V_{oc}$ losses relative to the Shockley-Queisser limit into short-circuit voltage losses $\Delta V_{oc,sc}$, radiative voltage losses $\Delta V_{oc,rad}$, and non-radiative voltage losses $\Delta V_{oc,non\text{-}rad}$. The small values of $\Delta V_{oc,sc}$ and $\Delta V_{oc,rad}$ effectively canceled each other out, indicating that voltage losses are entirely caused by non-radiative recombination. In accordance with literature, I observed that non-radiative voltage losses increased with higher bandgaps, corresponding to higher bromide concentrations, but note that they show no correlation with the Urbach energy. This suggests that the structural disorder causing the Urbach tail is not responsible for the non-radiative voltage losses. Furthermore, EQE measurements indicated that $J_{sc}$ losses were partly optical, which is well-understood, and partly electrical, which is less frequently considered but also impacts the *FF*. This interconnection between $J_{sc}$ and *FF* losses suggests the presence of electrical losses that extend beyond classical series or shunt resistances.

In **Chapter 4**, I introduced therefore voltage-dependent PL measurements as a diagnostic tool to probe recombination losses during charge extraction. The PL shows a maximum at OC conditions as expected but is not fully quenched at SC conditions. This behavior, resulting in high QFLS at all bias points, suggests non-ideal charge extraction. Having quantified the current losses during extraction due to recombination, I predict significant $J_{sc}$ and *FF* improvements, expected when perfect charge transport would prevent the

recombination, highlighting a potential avenue for device configuration improvements. Furthermore, the voltage-dependent PLQY points towards more complicated recombination sources than simple deep or shallow defects.

In **Chapter 5**, I delved deeper into the position of these non-radiative recombination sources inside the device, by investigating the $V_{oc}$ losses using PL measurements on both the perovskite films and complete devices. I determined the bulk limit of the $V_{oc}$ by the QFLS of the freestanding film, where I excluded the potentially distorting surface recombination by testing various passivation molecules and performing TRPL measurements on a series of perovskite films with different thicknesses. Pseudo-*JV* curves and drift-diffusion simulations revealed that in the device both the interfaces and the bulk equally constrain the $V_{oc}$, complicating the optimization process. This dual limitation emphasizes the critical importance of improving the bulk quality of the perovskite material before interfaces. I advocate for a combined characterization protocol employing both PL and *JV* measurements to effectively uncover and address the concealed limitations within the device.

In conclusion, co-evaporated perovskite solar cells are currently in a unique position as they are challenged by the absence of a single dominant loss mechanism. Instead, a combination of various loss processes collectively limits their performance. This complexity results in only incremental gains in efficiency upon mitigation of one loss channel, thereby slowing the pace of device optimization. This thesis has presented methods and strategies for disentangling the complexity and monitoring hidden and open improvements which ultimately is the only way to realize PCE enhancements in a systematic manner.

# 7 Resumen en Castellano

## 7.1 Introducción

### 7.1.1 Necesidad de tecnologías fotovoltaicas y células solares de perovskita

El cambio climático, impulsado por el aumento de las emisiones de $CO_2$, exige soluciones urgentes a medida que las necesidades energéticas globales continúan creciendo (Figure 1.1a). Las tecnologías de energía renovable, particularmente la solar y la eólica, ofrecen alternativas sostenibles, con costos decrecientes que las hacen más económicas que los combustibles fósiles (Figure 1.1c). Entre las tecnologías fotovoltaicas existentes, el silicio (Si) domina el mercado debido a la abundancia del material y su madurez tecnológica, pero presenta ciertas limitaciones como alta demanda energética en la producción y restricciones de eficiencia. Otras tecnologías, como el arseniuro de galio (GaAs), alcanzan eficiencias récord (29.1%, Figure 1.2) pero el material es caro y escaso, mientras que las tecnologías de películas delgadas (CIGS, CdTe, Si:H) ofrecen flexibilidad, aunque enfrentan desafíos como menores eficiencias y sensibilidad ambiental.

Las células solares de perovskita son tecnologías emergentes que combinan bajo costo con rápidas mejoras en eficiencia, siendo hoy en día comparables a los niveles del silicio (Figure 1.2). Estas células permiten configuraciones tándem que superan el límite de Shockley-Queisser, ofreciendo gran potencial transformador. Sin embargo, persisten desafíos relacionados con la escalabilidad, estabilidad y toxicidad, que deben abordarse. Este trabajo examina las propiedades físicas y las limitaciones de las células solares de perovskita fabricadas mediante una técnica de deposición libre de disolventes y escalable, llamada co-evaporación, para avanzar en su comercialización y mejorar del rendimiento energético.

### 7.1.2 Principio de funcionamiento de las células solares

El proceso fotovoltaico en una célula solar se describe en tres etapas (Figure 1.3): un fotón con energía $E_{ph}$ mayor que el ancho de banda prohibida $E_g$ del material absorbente, $E_{ph} >$

$E_g$, excita un electrón de la banda de valencia a la banda de conducción, creando un par electrón-hueco. Posteriormente, estos portadores de carga son separados y extraídos a través de contactos selectivos, generando una diferencia de energía $qV$ entre el ánodo y el cátodo.

El comportamiento corriente-voltaje ($JV$) de una unión p-n ideal sigue la ecuación del diodo de Shockley, incorporando la corriente fotogenerada $J_{gen}$ y la corriente de saturación $J_0$ (Equation (1.1)). Las pérdidas por recombinación, divididas en la componente radiativa y no-radiativa, determinan $J_0$, donde solo las pérdidas radiativas son inevitables (Equation (1.2)). Bajo iluminación, la curva $JV$ define parámetros clave del rendimiento fotovoltaico de la celda: la densidad de corriente de cortocircuito $J_{sc}$, el voltaje de circuito abierto $V_{oc}$ y el factor de llenado $FF$, siendo la eficiencia de conversión de potencia (PCE) $\eta$ el resultado de su producto y normalizada por la densidad de potencia incidente (Equation (1.3), Figure 1.4).

El modelo de Shockley-Queisser (SQ) establece los límites teóricos de eficiencia fotovoltaica para una célula solar de unión simple (Figure 1.5), asumiendo absorción perfecta, recombinación únicamente radiativa, y contactos ideales. Los límites para $J_{sc}$, $V_{oc}$, $FF$ y $\eta$ dependen únicamente de $E_g$ del material absorbente (Equations (1.8)–(1.12)). Así, $J_{sc}$ disminuye con un aumento de $E_g$, mientras que $V_{oc}$ aumenta casi linealmente. Este equilibrio conduce a un rango óptimo de $E_g$ entre 1.1 y 1.4 eV, alcanzando una eficiencia teórica del 33.6%.

Aunque el límite SQ proporciona una referencia teórica, las células solares reales se desvían debido a la presencia de fenómenos no ideales como reflexión, absorción parasitaria, recombinación no-radiativa y efectos resistivos. En una primera aproximación, el $J_{sc}$ se reduce por óptica imperfecta, el $V_{oc}$ por recombinación no-radiativa, y el $FF$ por pérdidas resistivas (Equation (1.7)). En esta tesis, exploraremos, por un lado, el origen y la cuantía de estas pérdidas aplicadas a células solares de perovskita co-evaporadas (Capítulo 7.3); por otro lado, discutiremos las pérdidas adicionales de $J_{sc}$ y $FF$ (Capítulo 7.4); y, finalmente, determinaremos el origen espacial de las pérdidas de $V_{oc}$ (Capítulo 7.5).

### 7.1.3 Dinámica de portadores de carga

Este capítulo se centra en los procesos físicos internos en semiconductores, incluyendo la dinámica de portadores de carga, los mecanismos de recombinación y su conexión con parámetros externos del dispositivo, como corriente y voltaje. Comenzamos con el equilibrio térmico y electroquímico en oscuridad, donde las concentraciones de portadores

en las bandas de conducción y valencia están determinadas por la distribución de Fermi-Dirac y la densidad efectiva de estados (Equations (1.13)-(1.15)). Para un semiconductor intrínseco, la concentración intrínseca de portadores $n_i$ depende de $E_g$ y la densidad de estados (Equation (1.16)).

Bajo iluminación, los portadores excedentes son generados por absorción de luz, gobernada por la ley de Lambert-Beer (Equation (1.17)). Esto genera una distribución no uniforme de portadores de carga, la cual se homogeniza mediante los efectos de movimiento por deriva y difusión. En perovskitas de haluros de plomo débilmente dopadas, la concentración de portadores excedentes $\Delta n$ domina, y la concentración total $n$ puede aproximarse a $\Delta n$ (Equations (1.18)-(1.19)). La separación del nivel de Fermi en niveles cuasi-Fermi para electrones y huecos define la separación de niveles cuasi-Fermi (QFLS), que representa el voltaje de circuito abierto máximo alcanzable, $V_{oc}$ (Equation (1.20)).

Los procesos de recombinación de carga devuelven el semiconductor al equilibrio y se clasifican en tipos radiativos y no radiativos. La recombinación radiativa, gobernada por el coeficiente $k_{rad}$, es inevitable y está incluida en el límite SQ (Equations (1.21)-(1.22)). Los mecanismos de recombinación no-radiativa incluyen la recombinación Auger, que escala con el cubo de la concentración de portadores, y la recombinación Shockley-Read-Hall (SRH), a través de estados trampa, dependiente de los tiempos de vida de atrapamiento y las profundidades de los estados (Equations (1.23)-(1.27)). La recombinación en las interfaces se caracteriza por las velocidades de recombinación superficial $S$, que deben minimizarse para dispositivos eficientes (Equations (1.28)-(1.29)).

La tasa total de recombinación $R_{tot}$ combina todos estos procesos y define el tiempo de vida efectivo de los portadores de carga $\tau_{eff}$ (Equation (1.30)). Este tiempo conecta las dinámicas internas con la densidad de corriente externa a través de la ecuación del diodo (Equation (1.31)).

La recombinación radiativa y el QFLS son medibles mediante espectroscopía de fotoluminiscencia (PL). La intensidad de PL proporciona información sobre el producto $np$ y el QFLS, con la ley generalizada de Planck estableciendo una conexión directa con el espectro de emisión (Equations (1.32)-(1.34)). El rendimiento cuántico de fotoluminiscencia (PLQY) es el número de fotones emitidos en comparación con el número de fotones de excitación y cuantifica las perdidas no-radiativas (Equations (1.35)-(1.36)).

Los estudios de fotoluminiscencia resuelta en el tiempo (TRPL) permiten medir los tiempos de vida transitorios de los portadores, capturando efectos dinámicos como atrapamiento, desatrapamiento, deriva y difusión. El tiempo de decaimiento diferencial $\tau_{diff}$ revela las rutas de recombinación dominantes a lo largo del tiempo, pasando de mecanismos rápidos, como la difusión, a procesos de recombinación más lentos (Equation (1.37)).

### 7.1.4 Células solares de perovskita

En esta tesis nos centramos exclusivamente en células solares de perovskita de haluro metálico. Las perovskitas, descubiertas por primera vez como un mineral en 1839, son materiales con la fórmula general $ABX_3$ (Figure 1.8a), donde A es un catión monovalente, B es un catión bivalente (comúnmente plomo o estaño) y X es un ion haluro (yoduro, bromuro o cloruro). Las perovskitas ofrecen anchos de banda prohibida ajustables mediante la variación de su composición, lo que las hace adecuadas para aplicaciones como LEDs y células fotovoltaicas (Figure 1.8b).

La primera célula solar de perovskita, fabricada en 2009, utilizó $MAPbI_3$ (MAPI) y $MAPbBr_3$ como materiales absorbentes incorporados en células sensibilizadas por colorante, logrando un PCE del 3.8%. Investigaciones posteriores demostraron que estos materiales poseen excelentes propiedades de transporte de carga, eliminando la necesidad de usar películas mesoporosas. Desde entonces, las eficiencias han aumentado rápidamente, alcanzando recientemente 26.7% (Figure 1.2).

Las perovskitas son materiales absorbentes ideales para células solares debido a sus propiedades físicas únicas. Exhiben coeficientes de absorción excepcionalmente altos cerca del $E_g$, permitiendo la absorción completa de la luz solar incluso con películas delgadas (Figure 1.8c). Esto simplifica su diseño, ya que permite alcanzar altos valores de $J_{sc}$ sin la necesidad de implementar mecanismos complejos de atrapamiento de luz. Además, muchas perovskitas muestran bajas energías de Urbach (12–20 meV), lo que indica un mínimo desorden térmico o estructural, reduciendo pérdidas de $V_{oc}$.

Los mecanismos de recombinación desempeñan un papel crucial en el rendimiento de las células de perovskitas. Entre ellas, la recombinación Auger es despreciable debido a la rápida desexcitación radiativa a altas densidades de portadores. Aunque la recombinación mediada por defectos, descrita por la teoría de Shockley-Read-Hall (SRH), es limitante, resulta menor en comparación con otros semiconductores de calidad similar. Ello se debe a que muchos defectos puntuales en la estructura cristalina de perovskita crean estados

trampa cerca del límite de la banda de valencia/conducción, en lugar de crear estados más profundos en la banda prohibida. Como consecuencia, es posible obtener películas muy eficientes procesadas en condiciones de baja temperatura, en las que altas densidades de defectos no impiden propiedades electrónicas favorables. Sin embargo, minimizar los estados trampa dentro de la banda prohibida sigue siendo un desafío clave de ingeniería.

La baja energía de enlace del excitón, inferior a la energía térmica a temperatura ambiente, facilita la separación inmediata en portadores libres en estas perovskitas, evitando los problemas de recombinación asociados a excitones fuertemente ligados. Una vez separados, los portadores de carga muestran movilidades suficientemente altas, lo que da lugar a longitudes de difusión mayores que el espesor típico de las películas de perovskita. Esto asegura un transporte eficiente de portadores sin depender de campos eléctricos internos, que a menudo son apantallados por iones móviles.

La asimetría necesaria para la separación y extracción de cargas se logra utilizando capas de transporte de electrones y huecos (ETLs y HTLs) que envuelven la capa de perovskita. Estas capas de transporte (TLs) deben tener alta movilidad de portadores mayoritarios, un alineamiento de bandas favorable y bloquear los portadores minoritarios (Figure 1.9).

Las técnicas de fabricación influyen significativamente en la calidad de las películas y el rendimiento de los dispositivos. Mientras que el procesado por disolución, como spin-coating, domina los estudios de investigación debido a su simplicidad, la co-evaporación ofrece un control estequiométrico preciso, la fabricación de películas densas y gran potencial de escalabilidad, ideal para aplicaciones de gran superficie. Esta tesis investiga exclusivamente películas de perovskita fabricadas por co-evaporación, las cuales, aunque menos investigadas, ofrecen alta reproducibilidad y superficies lisas y libres de imperfecciones, abordando muchas de las limitaciones asociadas a las películas procesadas por disolución.

### 7.1.5 Objetivo de la tesis

Aunque el PCE de las células solares de perovskita ha experimentado el progreso más rápido jamás visto entre las tecnologías solares hasta la fecha, su tasa de mejora ha comenzado recientemente a estabilizarse. En consecuencia, es esencial explorar en profundidad los mecanismos subyacentes que continúan limitando el PCE. A pesar de que las perovskitas procesadas en disolución se han estudiado ampliamente debido a su uso predominante, las características de las perovskitas depositadas al vacío, que exhiben

propiedades de crecimiento e interfaz distintivas, requieren una investigación más extensa. El objetivo de esta tesis es por tanto identificar los factores responsables de las pérdidas de rendimiento en células solares de perovskita co-evaporada.

• Con este fin, el Capítulo 7.3 brinda una descripción general de los parámetros limitantes del dispositivo en términos de $V_{oc}$, $J_{sc}$ y *FF*. Para ello se han estudiado cuatro tipos de células solares de perovskita co-evaporadas, con $E_g$ desde 1.52 a 1.88 eV. Estos parámetros se han evaluado en comparación con sus límites teóricos para cuantificar su contribución a las pérdidas generales de PCE. Además, se han analizado los orígenes de las pérdidas de $V_{oc}$, en relación a contribuciones de las pérdidas de $J_{sc}$, recombinación radiativa y recombinación no-radiativa, estudiadas mediante mediciones sensibles de EQE. Se ha abordado la influencia de la cola de absorción y la energía de Urbach, y se han relacionado las pérdidas de *FF* con las pérdidas de $J_{sc}$.

• En el Capítulo 7.4, el enfoque se ha desplazado hacia un examen más detallado de las pérdidas de *FF* y $J_{sc}$. Se presentan mediciones de PL dependientes del voltaje como una herramienta para caracterizar las pérdidas de recombinación durante la extracción de carga, lo que indica pérdidas de corriente. Se ha determinado el PLQY dependiente del voltaje en cada punto de polarización, y se ha analizado la curva *JV* esperada en el límite del transporte de carga perfecto.

• Finalmente, en el Capítulo 7.5 se investiga la fuente de las pérdidas de $V_{oc}$ no-radiativas en las células solares de perovskita co-evaporadas. La recombinación puede ocurrir en el seno de la capa de perovskita o en las interfaces con las capas de transporte. Identificar el sitio primario de recombinación es fundamental para optimizar el rendimiento del dispositivo, ya que esto determina la fuente dominante de pérdidas de $V_{oc,}$ la cual debe reducirse. La investigación se ha llevado a cabo mediante una combinación de mediciones de *JV*, mediciones de PL (tanto en la película de perovskita como en el dispositivo completo), y simulaciones de difusión por deriva. Además, se ha explorado la recombinación en la superficie de la película de perovskita primitiva, sin contacto con otros materiales, mediante mediciones de PL empleando una multitud de materiales de pasivación y mediciones de TRPL.

## 7.2 Técnicas experimentales

### 7.2.1 Preparación de muestras

La fabricación de las células solares estudiadas en esta tesis fue llevada a cabo por compañeros en el grupo de investigación, a quienes el autor extiende su gratitud. Aunque el enfoque principal de este trabajo radica en la caracterización, los métodos de fabricación se introducen brevemente.

Las técnicas de deposición de películas delgadas se clasifican en métodos basados en solución (por ejemplo, spin-coating) y métodos basados en vapor (por ejemplo, evaporación térmica). En esta tesis, todas las capas se depositaron mediante evaporación térmica, excepto las capas de pasivación en el Capítulo 7.5, que se aplicaron mediante spin-coating.

Todas las películas de perovskita fueron fabricadas en un ambiente de sala limpia. Los sustratos se limpiaron mediante baño de ultrasonidos, seguidos de un tratamiento con radiación UV-ozono. Para las células solares p-i-n (Capítulos 7.3 y 7.4), las capas $MoO_3$, TaTm, perovskita, $C_{60}$ y BCP se evaporaron secuencialmente, seguidas de un contacto metálico de plata (Ag). Para los dispositivos n-i-p (Capítulos 7.3 y 7.5), las capas de transporte de electrones, $SnO_2$ y $C_{60}$, se depositaron antes de la evaporación de la perovskita, mientras que las capas de transporte de huecos, TaTm, TPBi y $MoO_3$, así como los contactos metálicos, se agregaron posteriormente. Las películas de perovskita se co-evaporaron bajo condiciones de vacío, con tasas específicas de múltiple precursores, calibradas mediante microbalanzas de cristal de cuarzo (QCMs). Para las películas de MAPI, se utilizó un método de deposición con dos fuentes, el cual fue ajustado y mejorado a lo largo de la tesis. Las estequiometrías más complejas, como FAMAPI, FACsPbIBr y CsPbIBr, requirieron una co-evaporación coordinada de hasta cuatro fuentes. Finalmente, todos los dispositivos fueron encapsulados con óxido de aluminio mediante deposición de capas atómicas (ALD) para garantizar su estabilidad.

### 7.2.2 Análisis estructural

La estructura cristalina de las películas fue estudiada mediante cristalografía de difracción de rayos X (XRD). Esta técnica hace incidir rayos X a una muestra, registrando los ángulos e intensidades de los haces difractados como resultado de la disposición de los átomos dentro de la red cristalina.

La microscopía electrónica de barrido (SEM), se utilizó para capturar imágenes de alta resolución de las películas de perovskita y de los dispositivos completos, en disposición tanto transversal como superficial, con el fin de estudiar la morfología y el tamaño de los granos de la capa.

El grosor de las películas se midió con un perfilómetro mecánico. Para ello, se eliminó parte de las capas mediante rayado de la superficie con un objeto afilado. El perfilómetro registra la topografía de una muestra en una línea al mover un cantiléver sobre la superficie mientras aplica una fuerza descendente. De esta manera, el grosor de las películas puede determinarse mediante la altura del escalón creada en la zona rayada.

### 7.2.3 Análisis óptico

#### Espectroscopia UV-Vis

La espectroscopía UV-Vis se utilizó para medir la transmitancia y la reflectancia de películas individuales y de películas apiladas. En el Capítulo 7.4, las mediciones de transmitancia de la estructura glass/ITO/$MoO_3$/TaTm se realizaron para estimar la corriente total generada en la perovskita, tras considerar las pérdidas ópticas. Una fuente de luz de deuterio-halógeno se dirigió a la superficie de la muestra a través de fibras ópticas en una caja de guantes llena de $N_2$. La luz transmitida se recolectó y analizó mediante un espectrómetro. La calibración se llevó a cabo realizando una medición en blanco para fijar la transmitancia al 100%.

Los datos de reflectancia del sustrato de vidrio como de la célula solar completa se presentaron en los Capítulos 7.3 y 7.4 para estimar las pérdidas ópticas. Las mediciones emplearon la misma fuente de luz y espectrómetro, pero se utilizó una esfera integradora para recolectar la luz reflejada. La esfera integradora tiene una apertura donde se coloca la muestra, de modo que solo la luz reflejada (tanto especular como difusa) es recolectada, mientras que la luz transmitida se pierde. Para garantizar una calibración precisa, se utilizó una placa de referencia cubierta con el mismo material que la esfera integradora.

#### Fotoluminiscencia

La espectroscopía de PL se utilizó extensivamente en esta tesis para medir la recombinación radiativa y el QFLS en películas de perovskita. Se emplearon dos configuraciones principales de PL: un sistema de PL dependiente del voltaje (Capítulo 7.4) y una caja de PL

personalizada para caracterización de alto rendimiento, desarrollada durante el curso de esta tesis (Capítulo 7.5).

El sistema de PL dependiente del voltaje (Figure 2.2) permitió medir simultáneamente la corriente y la PL bajo diferentes voltajes en células solares completas. Las muestras se montaron en un soporte personalizado con contactos eléctricos de cuatro terminales y se cubrieron con una máscara reflectante con una apertura de 0.06 $cm^2$. El dispositivo fue iluminado con un láser de diodo de 522 nm a través de una esfera integradora, garantizando una recolección uniforme de luz en toda la muestra. La PL emitida fue recolectada a través de un deflector, filtrada para eliminar la luz de excitación y analizada con un espectrómetro. La calibración con una lámpara halógena rastreable por NIST aseguró precisión espectral, lo que permitió calcular la densidad de corriente radiativa $J_{rad}$. Se realizaron escaneos de voltaje en direcciones directa e inversa, registrando señales de PL y corriente a lo largo del tiempo para capturar efectos transitorios. Los espectros de PL se integraron entre 1.47 eV y 1.8 eV para cuantificar $J_{rad}$, mientras que $J_{extr}$ se calculó a partir de la señal eléctrica promedio.

Debido a las limitaciones de la esfera integradora, como contaminación, baja eficiencia de recolección de luz y mantenimiento engorroso, se diseñó una caja de PL compacta y personalizada (Figure 2.3). Este sistema, impreso en 3D y optimizado para uso en cajas de guantes, incluye una lente colimadora para la excitación, un soporte de muestra intercambiable y un sistema de recolección de alta eficiencia con una lente doblete acromática y un colimador de fibra. La eficiencia de recolección mejoró en un factor de 170 en comparación con la esfera integradora, como se muestra en Figure 2.4a. La calibración se realizó con una lámpara halógena con un perfil de emisión lambertiano, asumiendo un comportamiento de emisión similar para las estructuras estudiadas depositadas sobre sustratos de vidrio. La validación contra el $V_{oc}$ de una célula solar p-i-n MAPI confirmó la precisión del sistema, presentando diferencias entre $\Delta E_F$ y $V_{oc}$ de solo 2 meV. En general, atribuimos un error de ± 10 meV a la determinación de QFLS debido a las incertidumbres de la calibración y a las inhomogeneidades locales de las muestras (Figure 5.1e).

Además, se desarrolló un software en MATLAB para el análisis automatizado de datos de PL, permitiendo calcular parámetros como PLQY y el QFLS. El software ofrece funcionalidades flexibles, incluyendo el ajuste de la cola de alta energía de los espectros de PL y la determinación de $E_g$ y el PLQY. Este sistema fue fundamental para el análisis de

las películas de MAPI en el Capítulo 7.5, donde los valores de PLQY y QFLS se extrajeron con alta precisión, demostrando la robustez de las configuraciones desarrolladas.

Fotoluminiscencia resuelta en el tiempo

La TRPL se utilizó en el Capítulo 7.5 para investigar los procesos de recombinación y la recombinación superficial en películas de perovskita sin encapsular. Las mediciones se realizaron en la Universidad Rey Abdullah de Ciencia y Tecnología (KAUST) utilizando un láser pulsado en el rango de nanosegundos (532 nm) y una cámara streak para la detección.

El análisis de los datos consistió en ajustar la curva de decaimiento de la intensidad con una función racional de cuarto grado para calcular el tiempo de decaimiento efectivo $\tau_{eff}$ y el QFLS en varios puntos temporales.

En tiempos iniciales, el QFLS se calculó utilizando la fluencia absorbida del láser y la densidad de portadores intrínsecos ($n_i$ = 8.05 × $10^4$ $cm^{-3}$ para MAPI). En tiempos posteriores, se empleó la relación exponencial entre el flujo de PL y el QFLS, lo que permitió el seguimiento dinámico de los procesos de recombinación y extracción de portadores.

### 7.2.4 Análisis optoelectrónico

Las curvas *JV* se emplearon para extraer el PCE y los parámetros clave de rendimiento ($J_{sc}$, $V_{oc}$ y *FF*). Las mediciones se realizaron utilizando una unidad de medida de fuente. Un simulador solar de LED proporcionó la iluminación para mediciones bajo iluminación simulada de 1 sol, calibrado con un diodo de referencia equipado con un filtro de corte infrarrojo. El diseño de la célula solar evaluada presentaba cuatro áreas iguales (0.0651 $cm^2$) con una apertura de 0.06 $cm^2$ definida por una máscara de sombreado. Para las mediciones de $V_{oc}$ dependientes de la intensidad (Suns-$V_{oc}$), se aplicaron filtros de densidad neutra con transmisiones medidas.

Los espectros de eficiencia cuántica externa (EQE) se registraron para evaluar las pérdidas de corriente dependientes de la longitud de onda, así como su influencia tanto en la corriente de saturación en oscuridad como en el $V_{oc}$ en el límite radiativo (Figure 2.6). Una lámpara de cuarzo-tungsteno-halógeno proporcionó luz monocromática mediante una rueda de filtros y un monocromador. La luz fue modulada con un chopper óptico, y la corriente del dispositivo se midió con un amplificador lock-in, mejorando la relación señal-ruido al

excluir el ruido de fuentes eléctricas externas. Dos fotodiodos calibrados se utilizaron para la calibración del sistema en diferentes rangos de energía. La estabilidad del sistema fue confirmada mediante calibraciones periódicas. Durante la tesis realizamos modificaciones al sistema de EQE para mejorar la sensibilidad y permitir mediciones absolutas de EQE. Un par de lentes colimadoras enfocaron la luz en un punto de haz más pequeño, aumentando la densidad de potencia y la precisión de las mediciones. Las mediciones sensibles cerca de $E_g$ requirieron múltiples ejecuciones con diferentes ganancias, constantes de tiempo y filtros de paso largo para alcanzar un rango dinámico de hasta cinco órdenes de magnitud y niveles de ruido tan bajos como $10^{-7}$. Estas mediciones individuales se combinaron para producir espectros completos de EQE, como se muestra en Figure 2.6.

### 7.2.5 Simulación de deriva-difusión

En el Capítulo 7.5, se realizaron simulaciones de dispositivos utilizando SIMsalabim (Versión 3.77), un simulador de deriva-difusión para dispositivos semiconductores disponible en https://github.com/kostergroup/SIMsalabim. Este software resuelve las ecuaciones de continuidad para procesos como recombinación, deriva, difusión y transferencia de carga, utilizando parámetros de entrada como niveles de energía, permitividad, movilidades y estados atrapados.

El simulador se empleó para ajustar curvas pseudo-*JV* derivadas de mediciones de PL y *JV* bajo diferentes intensidades de luz. Estas curvas se compararon con límites teóricos, incorporando progresivamente mecanismos de pérdida desde el seno del material hasta la interfaz, lo que permitió desarrollar un modelo integral del dispositivo. Los parámetros iniciales para MAPI y las capas de transporte de carga (CTLs) se tomaron de la literatura, ajustando la constante de recombinación radiativa ($k_{rad}$) para coincidir con el límite SQ. La recombinación en el seno del material se modeló considerando la recombinación en los límites de grano, ajustando la densidad de estados trampa y los niveles de dopaje para reproducir los datos de Suns-$\Delta E_{F,film}$. Los parámetros de recombinación en las interfaces se optimizaron para ajustar la curva Suns-$V_{oc}$ y los de transporte para ajustar la curva *JV*, proporcionando información sobre posibles mejoras en el dispositivo (Figure 5.4).

## 7.3 Orígenes de la pérdida de eficiencia en los parámetros de la *JV*

### 7.3.1 Introducción

Como se ha comentado en la introducción, la curva *JV* es el método básico de caracterización de las células solares. La curva proporciona acceso directo al PCE, pero los parámetros $V_{oc}$, $J_{sc}$ y *FF* también permiten una primera estimación de los diferentes mecanismos de pérdida, en comparación con sus límites teóricos. En este capítulo se ha examinado una multitud de estructuras de células solares, con diferentes composiciones de perovskita, para cuantificar los mecanismos de pérdida existentes en células solares de perovskita co-evaporada y encontrar tendencias comunes.

### 7.3.2 Resultados

Se han analizado espectros sensibles de EQE para cuatro composiciones principales de perovskita, con variaciones en las capas de transporte de carga (CTLs), la configuración (*n-i-p* frente a *p-i-n*) y el espesor de la perovskita. Figure 3.1 muestra los espectros de EQE agrupados por composición. Los dispositivos de MAPI y CsPbIBr presentan variaciones menores debido al proceso de fabricación, mientras que FAMAPI y FACsPbIBr incorporan ajustes composicionales para optimizar $E_g$. La EQE decae exponencialmente por debajo de $E_g$. Destaca que CsPbIBr muestra una EQE sub-banda prohibida aumentada, posiblemente causada por estados de transferencia de carga entre CsPbIBr y $C_{60}$ (Figure 3.1d).

Se han extraído los parámetros clave de energía de Urbach $E_U$, ancho de banda prohibida $E_g$ y el límite de voltaje radiativo $V_{oc,rad}$ como se muestra en Figure 3.2. La $E_U$ se determinó a partir del decaimiento exponencial de la EQE, mientras que $E_g$ se identificó como el pico en la derivada de la curva EQE. La corriente de saturación radiativa en oscuridad $J_{0,rad}$ se obtuvo con el fin de calcular $V_{oc,rad}$ a partir del espectro de electroluminiscencia calculado, el cual depende fuertemente de la cola de la banda de EQE. En Figure 3.2c se aprecia menor señal de electroluminiscencia en FACsPbIBr debido al bajo valor de EQE cerca de $E_g$, mientras que CsPbIBr exhibe una señal extendida asociada a la mayor absorción sub-banda.

Las pérdidas de $V_{oc}$ se pueden descomponer en pérdidas de absorción ($\Delta V_{oc,sc}$), pérdidas radiativas ($\Delta V_{oc,rad}$) y pérdidas no-radiativas ($\Delta V_{oc,non\text{-}rad}$). Figure 3.3 muestra que $V_{oc,rad}$, el cual incluye $\Delta V_{oc,sc}$ y $\Delta V_{oc,rad}$, se aproxima al límite SQ, mientras que $\Delta V_{oc,non\text{-}rad}$ refleja

pérdidas significativas que aumentan en las perovskitas de $E_g$ ancha, probablemente impulsadas por la mala alineación de las CTLs y la recombinación en las interfaces.

En Figure 3.4a, las pérdidas de voltaje no-radiativas se correlacionan con $E_g$ e implican valores bajos de PLQY, sugiriendo así un margen considerable para la mejora. Las energías de Urbach son mínimas (12–23 meV) en todas las perovskitas, aunque más variables en FACsPbIBr y CsPbIBr (Figure 3.4b). El impacto de las energías de Urbach sobre $\Delta V_{oc,rad}$ se ilustra en Figure 3.4c, con mínimas mejoras en $V_{oc}$ debido a la reducción de $J_{0,rad}$ para algunas perovskitas, ocasionada por pérdidas de absorción. En general, las pérdidas de voltaje radiativo son despreciables, dado que los valores de $E_U$ permanecen por debajo de la energía térmica *kT*.

Figure 3.5 cuantifica las pérdidas de $V_{oc}$, $J_{sc}$ y *FF* en relación con sus límites radiativos, mostrando que los tres factores contribuyen en igual medida a las pérdidas de PCE. Para CsPbIBr, las pérdidas son más pronunciadas posiblemente debido a la segregación de haluros, a una alineación de bandas deficiente, y a la recombinación en las interfaces con las CTLs.

Para identificar las pérdidas en $J_{sc}$, Figure 3.6a compara la EQE y la eficiencia cuántica interna (IQE). Las pérdidas por reflexión representan aproximadamente un 10% del EQE, y se observan reducciones adicionales en el IQE, relacionadas con la existencia de absorción parasitaria y recombinación. Las pérdidas eléctricas causadas por extracción de carga ineficiente son evidentes en Figure 3.6b, donde los datos experimentales se desvían de las tendencias simuladas basadas únicamente en resistencias serie y shunt. Por lo tanto, las pérdidas en $J_{sc}$ y *FF* se atribuyen a problemas de recombinación e ineficiencias de extracción, requiriendo una optimización adicional, como se discute en el Capítulo 7.4.

### 7.3.3 Conclusión

En este estudio, se han analizado las pérdidas de eficiencia en células solares de perovskita co-evaporadas, centrándonos en las contribuciones de $V_{oc}$, $J_{sc}$ y *FF* al rendimiento general. Según los resultados experimentales, los tres parámetros *JV* contribuyen por igual a las pérdidas de eficiencia. Utilizando mediciones EQE de alto rango dinámico en varias composiciones de perovskita, hemos cuantificado las pérdidas de voltaje en las componentes absorbente, radiativa y no-radiativa. Nuestros hallazgos confirman que la recombinación no-radiativa domina las pérdidas de voltaje, siendo las pérdidas radiativas insignificantes debido a las bajas energías de Urbach de los materiales estudiados. Es por

tanto necesario conocer el origen espacial de la recombinación no-radiativa para poder optimizar la eficiencia del dispositivo. Esto puede suceder dentro de la capa absorbente o en las interfaces con los CTL, lo que se investigarán en el Capítulo 7.5. Hemos evaluado además el IQE, identificando ineficiencias de absorción parásita y de recolección como posibles contribuyentes a las pérdidas de $J_{sc}$. Al analizar la interacción entre $J_{sc}$ y *FF*, hemos aislado los efectos de las pérdidas ópticas y eléctricas, concluyendo que los impulsores de las pérdidas en *FF* y $J_{sc}$ son problemas de recombinación y extracción. En el capítulo 7.4, exploraremos un método para investigar estas pérdidas de recombinación durante la extracción.

## 7.4 Pérdidas por recombinación durante la extracción

### 7.4.1 Introducción

En el Capítulo7.3, demostramos que las células solares de perovskita co-evaporada exhiben una correlación entre las pérdidas de $J_{sc}$ y *FF*, atribuidas principalmente a pérdidas eléctricas que no pueden describirse completamente mediante resistencias en serie y en shunt constantes. En este capítulo, profundizamos en los orígenes de estas pérdidas. Aquí y en el Capítulo 7.5, nos centramos específicamente en las células solares MAPI, ya que este sistema de perovskita se beneficia de un proceso de fabricación de referencia bien establecido y exhibió las pérdidas relativas más pequeñas en el análisis anterior. Este capítulo se basa en la referencia [159].

### 7.4.2 Resultados

Realizamos mediciones *JV* y PL en una célula solar *p-i-n* de MAPI, depositada al vacío (arquitectura: ITO/$MoO_3$/TaTm/MAPI/$C_{60}$/BCP/Ag). Estas mediciones, realizadas con una esfera integradora bajo iluminación láser de 522 nm y a una velocidad de barrido lenta, arrojaron valores de $V_{oc}$ = 1.13 V, $J_{sc}$ = 19.2 mA cm$^{-2}$ y *FF* = 68%. Esto es similar a la curva *JV* bajo iluminación simulada AM1.5G y alta velocidad de barrido, que alcanzó $V_{oc}$ = 1.11 V, $J_{sc}$ = 18.0 mA cm$^{-2}$, *FF* = 70% y $\eta$ = 14.0% (Figure 4.1a frente a Figure 4.1b).

En cada punto de voltaje, la corriente generada $J_{gen}$, asociada a los fotones absorbidos, puede dividirse en corriente de recombinación $J_{rec}$ y corriente extraída $J_{extr}$. La corriente de recombinación incluye componentes radiativos $J_{rad}$ y no radiativos $J_{non\text{-}rad}$, con un comportamiento dependiente del voltaje descrito en las Equations (4.1)-(4.6).

A $V = 0$, la extracción ideal supone que $J_{sc} = J_{gen}$. Sin embargo, la luminiscencia medida indica pérdidas radiativas incluso en condiciones de cortocircuito (SC), lo que sugiere una extracción de carga imperfecta (Figure 4.2). En condiciones de circuito abierto (OC), $J_{rec}$ compensa a $J_{gen}$, donde una PLQY baja cuantifica la fracción radiativa. El QFLS $\Delta E_F$ en $V_{oc}$, estimado a partir de los espectros de PL, coincide con el $V_{oc}$ medido eléctricamente (1.13 eV), validando la configuración experimental (Figure 4.3). A voltajes más bajos, $\Delta E_F$ se satura en ~1.035 eV, indicando una alta densidad de portadores dentro de la perovskita.

Para estimar $J_{gen}$, se compararon tres enfoques (Figure 4.5a): Primero, la absortancia basada en reflexión, la cual resultó en $J_{gen}$ = 22.6 mA cm$^{-2}$; segundo, la absortancia basada en transmisión, que proporcionó un valor de 20.4 mA cm$^{-2}$; Finalmente, la reducción de PL en condiciones de cortocircuito, que dio $J_{gen}$ = 20.75 mA cm$^{-2}$, adoptado como el resultado más fiable. Este análisis de pérdidas revela que 1.85 mA cm$^{-2}$ se pierden por absorción parasitaria (7.5% relativos del límite SQ), y 1.55 mA cm$^{-2}$ debido a recombinación en condiciones de SC (6.2%).

Se ha definido la dependencia de PLQY con el voltaje, el cual disminuye a voltajes más bajos, indicativo generalmente de una recombinación dominada por trampas profundas (Figure 4.5b). Las desviaciones respecto a las predicciones teóricas sugieren la presencia de trampas medianamente profundas o efectos iónicos.

Además, se han estimado las condiciones de transporte ideales asumiendo que $\Delta E_F = qV$, mostrando que una extracción de carga optimizada podría aumentar el *FF* al 84.5% (mejora relativa del 18.2%) y el $J_{sc}$ hasta $J_{gen}$, incrementando la densidad de potencia a 19.8 mW cm$^{-2}$ (Figure 4.6).

Este análisis se extendió a MAPb(IBr)$_3$ ($E_g$ = 1.68 eV), revelando un potencial de mejora en $J_{sc}$ de 15.1 a 17.08 mA cm$^{-2}$ y en *FF* del 75% al 83.4% (Figure 4.7).

### 7.4.3 Conclusión

En este capítulo, se ha investigado la interacción de la generación, recombinación y extracción de carga en células solares de perovskita co-evaporadas, con un enfoque en los orígenes de las pérdidas de $J_{sc}$ y *FF* más allá de la reflexión. Mediante mediciones de PL dependientes del voltaje, calibradas en valor absoluto de flujo de fotones, se han cuantificado las densidades de corriente radiativa y extraída a lo largo de la curva *JV*. El alto valor de QFLS, obtenido incluso bajo condiciones de corto circuito, indica que el

transporte de carga no está funcionando de manera eficiente, lo que permite que los portadores se recombinen antes de ser extraídos. El PLQY dependiente del voltaje también sugiere que la recombinación no está dominada completamente por trampas profundas ni por trampas superficiales. La determinación de la densidad de corriente generada de tres formas diferentes confirmó que en el dispositivo MAPI investigado $J_{sc} \neq J_{gen}$, con una pérdida considerable de 1.85 mA $cm^{-2}$ atribuida a la absorción parásita y una pérdida de 1.55 mA $cm^{-2}$ debido a la recombinación incluso en condiciones SC. En un escenario idealizado de transporte de carga perfecto, la *FF* de la célula solar mejoraría sustancialmente, como lo demuestra una *FF* prevista de al menos el 84.5 % en comparación con el valor medido del 68 %. Extendimos esta metodología a células solares $MAPb(IBr)_3$ con $E_g$ más amplia y obtuvimos resultados similares que demuestran la universalidad de los hallazgos.

## 7.5 Recombinación en el Volumen e Interfaces

### 7.5.1 Introducción

En los capítulos 7.3 y 7.4, vimos que el PLQY del dispositivo terminado es muy inferior a 1, lo que provoca pérdidas de voltaje no-radiativas. Ahora, queremos estudiar al origen espacial de estas pérdidas. Este capítulo se basa en la referencia [193].

### 7.5.2 Resultados

Las células solares de perovskita co-evaporadas investigadas en este capítulo emplean una configuración *n-i-p* con ITO/$SnO_2$/$C_{60}$ y TaTm/TPBi/$MoO_3$/Ag como capas de extracción de electrones y huecos, respectivamente (Figure 5.1a). Las películas de MAPI presentan morfologías heterogéneas con tamaños de grano cristalino que varían entre 100 y 400 nm. Esta morfología sugiere que los portadores de carga encuentran múltiples límites de grano durante la extracción, aumentando la probabilidad de recombinación en sitios de trampa.

Una curva típica *JV* para dispositivos de MAPI co-evaporado muestra un $V_{oc}$ de 1.13 V (Figure 5.1b), superior al promedio de los dispositivos procesados en solución (1.09 V), pero inferior al límite radiativo. Para investigar las pérdidas de $V_{oc}$, se realizaron mediciones de PLQY en películas independientes y dispositivos completos. Bajo iluminación equivalente a AM1.5G, el PLQY fue 0.146% para la película y 0.051% para el dispositivo, correspondientes a valores de $\Delta E_F$ de 1.157 eV y 1.130 eV, respectivamente, coincidiendo

estrechamente con el $V_{oc}$ (Figure 5.1c-e). Esta diferencia mínima contrasta con las perovskitas procesadas en solución, donde las muestras de película suelen mostrar valores altos de PLQY.

Para descartar los efectos de recombinación superficial en las películas independientes, los cuales podrían distorsionar el PLQY respecto al límite en el volumen, se ha realizado un análisis de PL incorporando varios agentes de pasivación. Como se muestra en Figure 5.3a, la mejora en $\Delta E_{F,film}$ fue insignificante, indicando así que la recombinación superficial contribuye mínimamente a la recombinación en la muestra de película. Mediciones de TRPL en películas de diferentes espesores (170 - 680 nm) confirmaron esta observación. El tiempo de vida de los portadores disminuye con el espesor (Figure 5.3f), lo que es inconsistente con la dominancia de la recombinación superficial, respaldando la conclusión de que la recombinación en el volumen gobierna los tiempos de vida de los portadores en estas películas.

Para evaluar la recombinación en las interfaces en el dispositivo completo, se realizaron simulaciones utilizando un modelo de deriva-difusión, las cuales indicaron que las pérdidas por recombinación contribuyen de manera similar tanto en el seno de la película como en las interfaces (Figure 5.4). Las curvas *JV* simuladas con propiedades ideales en el seno del material o en las interfaces mostraron solo mejoras menores en la eficiencia (~1.5%). Esta doble limitación del $V_{oc}$ dificulta la detección experimental de mejoras aisladas en el seno o en las interfaces, lo que complica la optimización del dispositivo.

Para abordar el problema, se propone una estrategia iterativa de optimización que combina mediciones de PL y *JV* en películas y dispositivos (Figure 5.5). El proceso implica mejorar en primer lugar las propiedades del seno de la película (Paso 1), y acto seguido optimizar las interfaces (Paso 2). Para ilustrarlo se ha mostrado un ejemplo empleando MACl como agente de pasivación del seno del material, lo que aumentó $\Delta E_{F,film}$ en 66 meV (Figure 5.6b), aunque $V_{oc}$ solo mejoró en 20 mV (Figure 5.6e-f) y en gran parte debido al desplazamiento de $E_g$. Esto destaca la necesidad de un procedimiento de optimización sistemática, como el sugerido en esta tesis, para lograr mayores mejoras en el rendimiento.

### 7.5.3 Conclusión

En resumen, con la ayuda de medidas de PL, pseudo-*JV*, curvas *JV* y simulaciones de dispositivos hemos demostrado que, en las células solares de perovskita MAPI co-evaporadas, la recombinación en la interfaz y en el seno del material limitan

equiparablemente el $V_{oc}$. En esa situación, la caracterización típicamente realizada en células solares, basada únicamente en curvas *JV*, resulta insuficiente, al ser difícilmente detectables mejoras individualizadas en la calidad del material, lo que puede obstaculizar la optimización del dispositivo. Para avanzar en esta problemática, se enfatiza la necesidad de realizar comparaciones de PL entre película y dispositivo como protocolo básico de caracterización, junto a medidas de *JV* , lo que abre nuevas posibilidades hacia la detección de mejoras de rendimiento. Como prueba de concepto, se ha corroborado dicha problemática sobre sistemas reales MAPI co-evaporadas, y se ha aplicado el primer paso del procedimiento propuesto co-evaporando MAPI con pasivante MACl. Ello conduce a un aumento significativo en el PLQY de la película, pero mínimo aumento en el $V_{oc}$ del dispositivo, en concordancia con nuestra predicción. Es importante destacar que la metodología propuesta es aplicable (y debe aplicarse) a cualquier estado de optimización de la célula solar: en composiciones de perovskita no óptimas, en métodos de fabricación novedosos (limitados tanto por la recombinación en el seno como en la interfaz), o incluso en aquellos trabajos que utilizan células altamente eficientes con interfaces suficientemente mejoradas, en las que el $V_{oc}$ del dispositivo se acerca al QFLS de la película.

## 7.6 Conclusiones

El objetivo de esta tesis ha sido identificar los mecanismos clave de pérdida de eficiencia en las células solares de perovskita co-evaporada, que carecen de una caracterización fundamental en comparación con sus análogos procesados en solución. En un análisis exhaustivo, se ha comenzado con una amplia investigación en el Capítulo 3 y se ha ido profundizando progresivamente en estudios más detallados en los Capítulos 4 y 5.

En el Capítulo 3, se ha analizado las pérdidas de eficiencia en las células solares de perovskita co-evaporada mediante la disección de los parámetros *JV* $V_{oc}$, $J_{sc}$ y *FF*. Descubrimos para cuatro formulaciones de perovskita diferentes, que los tres parámetros contribuyen por igual a las pérdidas de rendimiento, haciendo necesario realizar un análisis exhaustivo de cada uno. Utilizando mediciones EQE sensibles, las pérdidas de $V_{oc}$ respecto al límite de Shockley-Queisser se han podido desglosar en $\Delta V_{oc,sc}$, $\Delta V_{oc,rad}$ y $\Delta V_{oc,non\text{-}rad}$. Los pequeños valores de $\Delta V_{oc,sc}$ y $\Delta V_{oc,rad}$ se cancelaron entre sí de manera efectiva, lo que indica pérdidas causadas en su totalidad por recombinación no-radiativa. Tal como se muestra en la literatura, observamos que las pérdidas de voltaje no-radiativas aumentaron en

composiciones con mayor $E_g$, correspondientes a concentraciones de bromuro más altas, pero sin mostrar correlación con la energía de Urbach. Esto sugiere que el desorden estructural que causa la cola de Urbach no es responsable de las pérdidas de voltaje no-radiativas. Además, las mediciones de EQE indican que las pérdidas de $J_{sc}$ son en parte ópticas, lo que es habitual, pero también eléctricas, lo impacta negativamente en el valor de *FF*. Esta interconexión entre las pérdidas de $J_{sc}$ y *FF* sugiere la presencia de pérdidas eléctricas que se extienden más allá de las resistencias clásicas en serie o shunt.

En el Capítulo 4, se han propuesto mediciones de PL dependientes del voltaje como una herramienta de diagnóstico para investigar las pérdidas de recombinación durante la extracción de carga. El PL muestra un valor máximo en condiciones OC, como es de esperar, pero no se extingue por completo en condiciones SC. Este comportamiento, que da como resultado un valor QFLS alto en todos los puntos de polarización, sugiere una extracción de carga no ideal. Habiendo cuantificado las pérdidas de corriente debido a la recombinación durante la extracción, predecimos mejoras significativas de $J_{sc}$ y *FF*, anticipadas solo ante un transporte de carga perfecto, destacando una vía potencial para mejoras en la configuración del dispositivo. Además, el PLQY dependiente del voltaje apunta hacia fuentes de recombinación más complicadas que simples defectos profundos o superficiales.

En el Capítulo 5, profundizamos en la posición de estas fuentes de recombinación no-radiativa dentro del dispositivo, investigando las pérdidas de $V_{oc}$ utilizando mediciones de PL tanto en las películas de perovskita como en dispositivos completos. Determinamos el límite de volumen del $V_{oc}$ por el QFLS de la película independiente, donde excluimos la recombinación de superficie potencialmente distorsionante, probando varias moléculas de pasivación y realizando mediciones de TRPL en una serie de películas de perovskita con diferentes espesores. Las curvas pseudo-*JV* y las simulaciones de difusión de deriva revelaron que en el dispositivo tanto las interfaces como el volumen restringen por igual el $V_{oc}$, lo que complica el proceso de optimización. Esta doble limitación pone de relieve la importancia crítica de mejorar la calidad del seno del material de perovskita antes de las interfaces. Abogamos por un protocolo de caracterización combinado que emplee mediciones de PL y *JV* para descubrir y abordar de manera efectiva las limitaciones ocultas dentro del dispositivo.

En conclusión, las células solares de perovskita co-evaporada se encuentran actualmente en una posición especial, ya que se enfrentan al desafío de la ausencia de un único mecanismo de pérdida dominante. Por el contrario, la combinación de varios procesos de pérdida limita colectivamente su rendimiento. Esta complejidad establece barreras a la detección de posibles ganancias en la eficiencia tras la mitigación de solo un canal de pérdida, lo que ralentiza el ritmo de optimización del dispositivo. Esta tesis ha presentado métodos y estrategias para desentrañar esta complejidad y monitorear las mejoras ocultas y visibles, que en última instancia permiten lograr mejoras de PCE de manera sistemática.

# 8 Bibliography


1 P. Würfel, *Physics of Solar Cells*, Wiley, 2005.

2 J. Nelson, *The Physics of Solar Cells*, published by Imperial College Press and distributed by World Scientific Publishing Co., 2003.

3 S. M. Sze and K. K. Ng, *Physics of Semiconductor Devices*, John Wiley & Sons, Inc., 2006.

4 J. Bisquert, *The Physics of Solar Cells*, CRC Press, Boca Raton, FL : CRC Press, Taylor & Francis Group, [2018], 2017.

5 S. Arrhenius, XXXI. On the influence of carbonic acid in the air upon the temperature of the ground, *The London, Edinburgh, and Dublin Philosophical Magazine and Journal of Science*, 1896, **41**, 237–276.

6 G. Supran, S. Rahmstorf and N. Oreskes, Assessing ExxonMobil's global warming projections, *Science (1979)*, 2023, **379**, eabk0063.

7 BP, Statistical Review of World Energy | Energy economics | Home, https://www.bp.com/en/global/corporate/energy-economics/statistical-review-of-world-energy.html, (accessed 3 February 2023).

8 Lazard.com | Levelized Cost Of Energy, Levelized Cost Of Storage, and Levelized Cost Of Hydrogen, https://www.lazard.com/perspective/levelized-cost-of-energy-levelized-cost-of-storage-and-levelized-cost-of-hydrogen/, (accessed 3 February 2023).

9 S. T. Huber and K. Steininger, Critical sustainability issues in the production of wind and solar electricity generation as well as storage facilities and possible solutions, *J Clean Prod*, 2022, **339**, 130720.

10 D. Serrano, A. Margalida, J. M. Pérez-García, J. Juste, J. Traba, F. Valera, M. Carrete, J. Aihartza, J. Real, S. Mañosa, C. Flaquer, I. Garin, M. B. Morales, J. T. Alcalde, B. Arroyo, J. A. Sánchez-Zapata, G. Blanco, J. J. Negro, J. L. Tella, C. Ibañez, J. L. Tellería, F. Hiraldo and J. A. Donázar, Renewables in Spain threaten biodiversity, *Science (1979)*, 2020, **370**, 1182–1183.

11 V. J. S. Jr., S. R. Gephard and S. M. Pescitelli, Effects of Multiple Low-Head Dams on Fish, Macroinvertebrates, Habitat, and Water Quality in the Fox River, Illinois, *Wiley*, 2011, **25**, 975–992.

12 M. Perez and R. Perez, Update 2022 – A fundamental look at supply side energy reserves for the planet, *Solar Energy Advances*, 2022, **2**, 100014.

13 Photovoltaics Report - Fraunhofer ISE, https://www.ise.fraunhofer.de/en/publications/studies/photovoltaics-report.html, (accessed 4 February 2023).

14 W. Palz, Ed., *Power for the World*, Jenny Stanford Publishing, 2010.

15 J. R. Rumble, Ed., in *CRC Handbook of Chemistry and Physics (Internet Version)*, CRC Press/Taylor & Francis, Boca Raton, FL, 2022, vol. 103rd Edition.

16 S. Bhattacharya and S. John, Beyond 30% Conversion Efficiency in Silicon Solar Cells: A Numerical Demonstration, *Scientific Reports 2019 9:1*, 2019, **9**, 1–15.

17 J. Jean, P. R. Brown, R. L. Jaffe, T. Buonassisi and V. Bulović, Pathways for solar photovoltaics, *Energy Environ Sci*, 2015, **8**, 1200–1219.

18 National Renewable Energy Laboratory, NREL. PV Research Cell Record Efficiency Chart.

19 D. Feldman, J. Zuboy, K. Dummit, D. Stright, M. Heine, S. Grossman and R. Margolis, *Spring 2024 Solar Industry Update*, Golden, CO (United States), 2024.

20 L. A. Zafoschnig, S. Nold and J. C. Goldschmidt, The Race for Lowest Costs of Electricity Production: Techno-Economic Analysis of Silicon, Perovskite and Tandem Solar Cells, *IEEE J Photovolt*, 2020, **10**, 1632–1641.

21 E. Chodos, April 25, 1954: Bell Labs Demonstrates the First Practical Silicon Solar Cell, https://www.aps.org/publications/apsnews/200904/physicshistory.cfm, (accessed 5 February 2023).

22 B. J. Blank, Forschungszentrum Jülich, 2019.

23 W. Shockley, The Theory of p-n Junctions in Semiconductors and p-n Junction Transistors, *Bell System Technical Journal*, 1949, **28**, 435–489.

24 F. A. Lindholm, J. G. Fossum and E. L. Burgess, Application of the Superposition Principle to Solar-Cell Analysis, *IEEE Trans Electron Devices*, 1979, **26**, 165–171.

25 G. Kirchhoff, Ueber das Verhältniss zwischen dem Emissionsvermögen und dem Absorptionsvermögen der Körper für Wärme und Licht, *Ann Phys*, 1860, **185**, 275–301.

26 D. R. Myers, S. R. Kurtz, K. Emery, C. Whitaker and T. Townsend, Outdoor meteorological broadband and spectral conditions for evaluating photovoltaic modules, *Conference Record of the IEEE Photovoltaic Specialists Conference*, 2000, **2000-January**, 1202–1205.

27 W. Shockley and H. J. Queisser, Detailed balance limit of efficiency of p-n junction solar cells, *J Appl Phys*, 1961, **32**, 510–519.

28 S. Rühle, Tabulated values of the Shockley-Queisser limit for single junction solar cells, *Solar Energy*, 2016, **130**, 139–147.

29 T. Trupke, M. A. Green and P. Würfel, Improving solar cell efficiencies by down-conversion of high-energy photons, *J Appl Phys*, 2002, **92**, 1668.

30 M. A. Green, Solar cell fill factors: General graph and empirical expressions, *Solid State Electron*, 1981, **24**, 788–789.

31 F. Peña-Camargo, J. Thiesbrummel, H. Hempel, A. Musiienko, V. M. Le Corre, J. Diekmann, J. Warby, T. Unold, F. Lang, D. Neher and M. Stolterfoht, Revealing the doping density in perovskite solar cells and its impact on device performance, *Appl Phys Rev*, 2022, **9**, 021409.

32 W. Van Roosbroeck and W. Shockley, Photon-Radiative Recombination of Electrons and Holes in Germanium, *Physical Review*, 1954, **94**, 1558.

33 A. Richter, S. W. Glunz, F. Werner, J. Schmidt and A. Cuevas, Improved quantitative description of Auger recombination in crystalline silicon, *Phys Rev B Condens Matter Mater Phys*, 2012, **86**, 165202.

34 I. L. Braly, D. W. Dequilettes, L. M. Pazos-Outón, S. Burke, M. E. Ziffer, D. S. Ginger and H. W. Hillhouse, Hybrid perovskite films approaching the radiative limit with over 90% photoluminescence quantum efficiency, *Nature Photonics 2018 12:6*, 2018, **12**, 355–361.

35 W. Shockley and W. T. Read, Statistics of the Recombinations of Holes and Electrons, *Physical Review*, 1952, **87**, 835.

36 P. Würfel and W. Ruppel, The chemical potential of luminescent radiation, *J Lumin*, 1981, **24–25**, 925–928.

37 L. Krückemeier, B. Krogmeier, Z. Liu, U. Rau and T. Kirchartz, Understanding Transient Photoluminescence in Halide Perovskite Layer Stacks and Solar Cells, *Adv Energy Mater*, 2021, **11**, 2003489.

38 'Rose, Gustav: De novis quibusdam fossilibus quae in montibus Uraliis inveniuntur', Image 1 of 12 | MDZ, https://www.digitale-sammlungen.de/en/view/bsb10978561?page=,1, (accessed 21 February 2023).

39 P. Szuromi and B. Grocholski, Natural and engineered perovskites, *Science (1979)*, 2017, **358**, 732–733.

40 K. Hirose, R. Sinmyo and J. Hernlund, Perovskite in Earth's deep interior, *Science (1979)*, 2017, **358**, 734–738.

41 J. Hwang, R. R. Rao, L. Giordano, Y. Katayama, Y. Yu and Y. Shao-Horn, Perovskites in catalysis and electrocatalysis, *Science (1979)*, 2017, **358**, 751–756.

42 O. D. I. Moseley, T. A. S. Doherty, R. Parmee, M. Anaya and S. D. Stranks, Halide perovskites scintillators: unique promise and current limitations, *J Mater Chem C Mater*, 2021, **9**, 11588–11604.

43 S. Hikami and Y. Matsuda, High Tc Superconductors of the Perovskite Structure Oxides, *Jpn J Appl Phys*, 1987, **26**, 1027–1028.

44 V. M. Goldschmidt, Die Gesetze der Krystallochemie, *Naturwissenschaften*, 1926, **14**, 477–485.

45 A. K. Jena, A. Kulkarni and T. Miyasaka, Halide Perovskite Photovoltaics: Background, Status, and Future Prospects, *Chem Rev*, 2019, **119**, 3036–3103.

46 G. Grancini and M. K. Nazeeruddin, Dimensional tailoring of hybrid perovskites for photovoltaics, *Nature Reviews Materials 2018 4:1*, 2018, **4**, 4–22.

47 A. Kojima, K. Teshima, Y. Shirai and T. Miyasaka, Organometal halide perovskites as visible-light sensitizers for photovoltaic cells., *J Am Chem Soc*, 2009, **131**, 6050–1.

48 M. M. Lee, J. Teuscher, T. Miyasaka, T. N. Murakami and H. J. Snaith, Efficient hybrid solar cells based on meso-superstructured organometal halide perovskites, *Science (1979)*, 2012, **338**, 643–647.

49 H. S. Kim, C. R. Lee, J. H. Im, K. B. Lee, T. Moehl, A. Marchioro, S. J. Moon, R. Humphry-Baker, J. H. Yum, J. E. Moser, M. Grätzel and N. G. Park, Lead Iodide Perovskite Sensitized All-Solid-State Submicron Thin Film Mesoscopic Solar Cell with Efficiency Exceeding 9%, *Scientific Reports 2012 2:1*, 2012, **2**, 1–7.

50 M. A. Green, A. Ho-Baillie and H. J. Snaith, The emergence of perovskite solar cells, *Nature Photonics 2014 8:7*, 2014, **8**, 506–514.

51 S. Tao, I. Schmidt, G. Brocks, J. Jiang, I. Tranca, K. Meerholz and S. Olthof, Absolute energy level positions in tin- and lead-based halide perovskites, *Nature Communications 2019 10:1*, 2019, **10**, 1–10.

52 S. De Wolf, J. Holovsky, S. J. Moon, P. Löper, B. Niesen, M. Ledinsky, F. J. Haug, J. H. Yum and C. Ballif, Organometallic halide perovskites: Sharp optical absorption edge and its relation to photovoltaic performance, *Journal of Physical Chemistry Letters*, 2014, **5**, 1035–1039.

53 E. Aydin, M. De Bastiani and S. De Wolf, Defect and Contact Passivation for Perovskite Solar Cells, *Advanced Materials*, 2019, **31**, 1900428.

54 E. Ugur, M. Ledinský, T. G. Allen, J. Holovský, A. Vlk and S. De Wolf, Life on the Urbach Edge., *J Phys Chem Lett*, 2022, **13**, 7702–7711.

55 C. Gehrmann and D. A. Egger, Dynamic shortening of disorder potentials in anharmonic halide perovskites, *Nature Communications 2019 10:1*, 2019, **10**, 1–9.

56 J. Chantana, Y. Kawano, T. Nishimura, A. Mavlonov and T. Minemoto, Impact of Urbach energy on open-circuit voltage deficit of thin-film solar cells, *Solar Energy Materials and Solar Cells*, 2020, **210**, 110502.

57 B. Subedi, C. Li, C. Chen, D. Liu, M. M. Junda, Z. Song, Y. Yan and N. J. Podraza, Urbach Energy and Open-Circuit Voltage Deficit for Mixed Anion–Cation Perovskite Solar Cells, *ACS Appl Mater Interfaces*, 2022, **14**, 7796–7804.

58 A. Richter, M. Hermle and S. W. Glunz, Reassessment of the limiting efficiency for crystalline silicon solar cells, *IEEE J Photovolt*, 2013, **3**, 1184–1191.

59 T. Tiedje, E. Yablonovitch, G. D. Cody and B. G. Brooks, Limiting Efficiency of Silicon Solar Cells, *IEEE Trans Electron Devices*, 1984, **31**, 711–716.

60 T. Kirchartz, L. Krückemeier and E. L. Unger, Research Update: Recombination and open-circuit voltage in lead-halide perovskites, *APL Mater*, 2018, **6**, 100702.

61 W.-J. Yin, T. Shi and Y. Yan, Unusual defect physics in $CH_3NH_3PbI_3$ perovskite solar cell absorber, *Appl Phys Lett*, 2014, **104**, 063903.

62 J. Kang and L. W. Wang, High Defect Tolerance in Lead Halide Perovskite CsPbBr3, *Journal of Physical Chemistry Letters*, 2017, **8**, 489–493.

63 K. X. Steirer, P. Schulz, G. Teeter, V. Stevanovic, M. Yang, K. Zhu and J. J. Berry, Defect Tolerance in Methylammonium Lead Triiodide Perovskite, *ACS Energy Lett*, 2016, **1**, 360–366.

64 D. Meggiolaro, S. G. Motti, E. Mosconi, A. J. Barker, J. Ball, C. Andrea Riccardo Perini, F. Deschler, A. Petrozza and F. de Angelis, Iodine chemistry determines the defect tolerance of lead-halide perovskites, *Energy Environ Sci*, 2018, **11**, 702–713.

65 E. Gutierrez-Partida, H. Hempel, S. Caicedo-Dávila, M. Raoufi, F. Peña-Camargo, M. Grischek, R. Gunder, J. Diekmann, P. Caprioglio, K. O. Brinkmann, H. Köbler, S. Albrecht, T. Riedl, A. Abate, D. Abou-Ras, T. Unold, D. Neher and M. Stolterfoht, Large-Grain Double Cation Perovskites with 18 μs Lifetime and High Luminescence Yield for Efficient Inverted Perovskite Solar Cells, *ACS Energy Lett*, 2021, **6**, 1045–1054.

66 Z. Liu, L. Krückemeier, B. Krogmeier, B. Klingebiel, J. A. Márquez, S. Levcenko, S. Öz, S. Mathur, U. Rau, T. Unold and T. Kirchartz, Open-Circuit Voltages Exceeding 1.26 v in Planar Methylammonium Lead Iodide Perovskite Solar Cells, *ACS Energy Lett*, 2019, **4**, 110–117.

67 M. Abdi-Jalebi, M. Pazoki, B. Philippe, M. I. Dar, M. Alsari, A. Sadhanala, G. Divitini, R. Imani, S. Lilliu, J. Kullgren, H. Rensmo, M. Grätzel and R. H. Friend, Dedoping of Lead Halide Perovskites Incorporating Monovalent Cations, *ACS Nano*, 2018, **12**, 7301–7311.

68 D. W. deQuilettes, S. Koch, S. Burke, R. K. Paranji, A. J. Shropshire, M. E. Ziffer and D. S. Ginger, Photoluminescence Lifetimes Exceeding 8 μs and Quantum Yields Exceeding 30% in Hybrid Perovskite Thin Films by Ligand Passivation, *ACS Energy Lett*, 2016, **1**, 438–444.

69 M. Abdi-Jalebi, M. Ibrahim Dar, S. P. Senanayak, A. Sadhanala, Z. Andaji-Garmaroudi, L. M. Pazos-Outón, J. M. Richter, A. J. Pearson, H. Sirringhaus, M. Grätzel and R. H. Friend, Charge extraction via graded doping of hole transport layers gives highly luminescent and stable metal halide perovskite devices, *Sci Adv*, DOI:10.1126/sciadv.aav2012.

70 M. Abdi-Jalebi, Z. Andaji-Garmaroudi, S. Cacovich, C. Stavrakas, B. Philippe, J. M. Richter, M. Alsari, E. P. Booker, E. M. Hutter, A. J. Pearson, S. Lilliu, T. J. Savenije, H. Rensmo, G. Divitini, C. Ducati, R. H. Friend and S. D. Stranks, Maximizing and stabilizing luminescence from halide perovskites with potassium passivation, *Nature*, 2018, **555**, 497–501.

71 L. Qiao, W. H. Fang, R. Long and O. V. Prezhdo, Extending Carrier Lifetimes in Lead Halide Perovskites with Alkali Metals by Passivating and Eliminating Halide Interstitial Defects, *Angewandte Chemie - International Edition*, 2020, **59**, 4684–4690.

72 J. Tong, Z. Song, D. H. Kim, X. Chen, C. Chen, A. F. Palmstrom, P. F. Ndione, M. O. Reese, S. P. Dunfield, O. G. Reid, J. Liu, F. Zhang, S. P. Harvey, Z. Li, S. T. Christensen, G. Teeter,

D. Zhao and M. M. Al-jassim, Carrier lifetimes of >1 m s in Sn-Pb perovskites enable efficient all-perovskite tandem solar cells, 2019, **479**, 475–479.

73 M. Baranowski and P. Plochocka, Excitons in Metal-Halide Perovskites, *Adv Energy Mater*, DOI:10.1002/aenm.201903659.

74 D. Marongiu, M. Saba, F. Quochi, A. Mura and G. Bongiovanni, The role of excitons in 3D and 2D lead halide perovskites, *J Mater Chem C Mater*, 2019, **7**, 12006–12018.

75 T. M. Brenner, D. A. Egger, L. Kronik, G. Hodes and D. Cahen, Hybrid organic—inorganic perovskites: low-cost semiconductors with intriguing charge-transport properties, *Nature Reviews Materials 2016 1:1*, 2016, **1**, 1–16.

76 S. Albrecht, J. R. Tumbleston, S. Janietz, I. Dumsch, S. Allard, U. Scherf, H. Ade and D. Neher, Quantifying charge extraction in organic solar cells: The case of fluorinated PCPDTBT, *Journal of Physical Chemistry Letters*, 2014, **5**, 1131–1138.

77 M. M. Mandoc, L. J. A. Koster and P. W. M. Blom, Optimum charge carrier mobility in organic solar cells, *Appl Phys Lett*, 2007, **90**, 133504.

78 S. Akel, A. Kulkarni, U. Rau and T. Kirchartz, Relevance of Long Diffusion Lengths for Efficient Halide Perovskite Solar Cells, *PRX Energy*, 2023, **2**, 013004.

79 P. Calado, A. M. Telford, D. Bryant, X. Li, J. Nelson, B. C. O'Regan and P. R. F. Barnes, Evidence for ion migration in hybrid perovskite solar cells with minimal hysteresis, *Nature Communications 2016 7:1*, 2016, **7**, 1–10.

80 N. Tessler and Y. Vaynzof, Insights from Device Modeling of Perovskite Solar Cells, *ACS Energy Lett*, 2020, **5**, 1260–1270.

81 B. Das, Z. Liu, I. Aguilera, U. Rau and T. Kirchartz, Defect tolerant device geometries for lead-halide perovskites, *Mater Adv*, 2021, **2**, 3655–3670.

82 D. Moia, I. Gelmetti, P. Calado, Y. Hu, X. Li, P. Docampo, J. De Mello, J. Maier, J. Nelson and P. R. F. Barnes, Dynamics of Internal Electric Field Screening in Hybrid Perovskite Solar Cells Probed Using Electroabsorption, *Phys Rev Appl*, 2022, **18**, 044056.

83 N. Wu, D. Walter, A. Fell, Y. Wu and K. Weber, The Impact of Mobile Ions on the Steady-State Performance of Perovskite Solar Cells, *Journal of Physical Chemistry C*, 2020, **124**, 219–229.

84 J. Thiesbrummel, S. Shah, E. Gutierrez-Partida, F. Zu, F. Peña-Camargo, S. Zeiske, J. Diekmann, F. Ye, K. P. Peters, K. O. Brinkmann, P. Caprioglio, A. Dasgupta, S. Seo, F. A. Adeleye, J. Warby, Q. Jeangros, F. Lang, S. Zhang, S. Albrecht, T. Riedl, A. Armin, D. Neher, N. Koch, Y. Wu, V. M. Le Corre, H. Snaith and M. Stolterfoht, Ion-induced field screening as a dominant factor in perovskite solar cell operational stability, *Nat Energy*, 2024, **9**, 664–676.

85 D. Di Girolamo, N. Phung, F. U. Kosasih, F. Di Giacomo, F. Matteocci, J. A. Smith, M. A. Flatken, H. Köbler, S. H. Turren Cruz, A. Mattoni, L. Cinà, B. Rech, A. Latini, G. Divitini, C. Ducati, A. Di Carlo, D. Dini and A. Abate, Ion Migration-Induced Amorphization and

Phase Segregation as a Degradation Mechanism in Planar Perovskite Solar Cells, *Adv Energy Mater*, DOI:10.1002/aenm.202000310.

86 H. Back, G. Kim, J. Kim, J. Kong, T. K. Kim, H. Kang, H. Kim, J. Lee, S. Lee and K. Lee, Achieving long-term stable perovskite solar cells via ion neutralization, *Energy Environ Sci*, 2016, **9**, 1258–1263.

87 Y. Zhao, W. Zhou, Z. Han, D. Yu and Q. Zhao, Effects of ion migration and improvement strategies for the operational stability of perovskite solar cells, *Physical Chemistry Chemical Physics*, 2021, **23**, 94–106.

88 D. Walter, A. Fell, Y. Wu, T. Duong, C. Barugkin, N. Wu, T. White and K. Weber, Transient photovoltage in perovskite solar cells: Interaction of trap-mediated recombination and migration of multiple ionic species, *Journal of Physical Chemistry C*, 2018, **122**, 11270–11281.

89 D. A. Jacobs, Y. Wu, H. Shen, C. Barugkin, F. J. Beck, T. P. White, K. Weber and K. R. Catchpole, Hysteresis phenomena in perovskite solar cells: the many and varied effects of ionic accumulation, *Physical Chemistry Chemical Physics*, 2017, **19**, 3094–3103.

90 D. A. Jacobs, H. Shen, F. Pfeffer, J. Peng, T. P. White, F. J. Beck and K. R. Catchpole, The two faces of capacitance: New interpretations for electrical impedance measurements of perovskite solar cells and their relation to hysteresis, *J Appl Phys*, 2018, **124**, 225702.

91 J. Xing, Q. Wang, Q. Dong, Y. Yuan, Y. Fang and J. Huang, Ultrafast ion migration in hybrid perovskite polycrystalline thin films under light and suppression in single crystals, *Physical Chemistry Chemical Physics*, 2016, **18**, 30484–30490.

92 C. Eames, J. M. Frost, P. R. F. Barnes, B. C. O'Regan, A. Walsh and M. S. Islam, Ionic transport in hybrid lead iodide perovskite solar cells, *Nature Communications 2015 6:1*, 2015, **6**, 1–8.

93 E. Mosconi and F. De Angelis, Mobile Ions in Organohalide Perovskites: Interplay of Electronic Structure and Dynamics, *ACS Energy Lett*, 2016, **1**, 182–188.

94 A. Rajagopal, K. Yao and A. K. Y. Jen, Toward Perovskite Solar Cell Commercialization: A Perspective and Research Roadmap Based on Interfacial Engineering, *Advanced Materials*, 2018, **30**, 1800455.

95 X. Zhao, H. Shen, Y. Zhang, X. Li, X. Zhao, M. Tai, J. Li, J. Li, X. Li and H. Lin, Aluminum-Doped Zinc Oxide as Highly Stable Electron Collection Layer for Perovskite Solar Cells, *ACS Appl Mater Interfaces*, 2016, **8**, 7826–7833.

96 C. M. Wolff, P. Caprioglio, M. Stolterfoht and D. Neher, Nonradiative Recombination in Perovskite Solar Cells: The Role of Interfaces, *Advanced Materials*, 2019, **31**, 1902762.

97 C. Zhang and N.-G. Park, Materials and methods for cost-effective fabrication of perovskite photovoltaic devices, *Commun Mater*, 2024, **5**, 194.

98 T. Abzieher, D. T. Moore, M. Roß, S. Albrecht, J. Silvia, H. Tan, Q. Jeangros, C. Ballif, M. T. Hoerantner, B.-S. Kim, H. J. Bolink, P. Pistor, J. C. Goldschmidt, Y.-H. Chiang, S. D.

Stranks, J. Borchert, M. D. McGehee, M. Morales-Masis, J. B. Patel, A. Bruno and U. W. Paetzold, Vapor phase deposition of perovskite photovoltaics: short track to commercialization?, *Energy Environ Sci*, 2024, **17**, 1645–1663.

99 F. Palazon, D. Pérez-del-Rey, B. Dänekamp, C. Dreessen, M. Sessolo, P. P. Boix and H. J. Bolink, Room-Temperature Cubic Phase Crystallization and High Stability of Vacuum-Deposited Methylammonium Lead Triiodide Thin Films for High-Efficiency Solar Cells, *Advanced Materials*, 2019, **1902692**, 1902692.

100 V. S. Chirvony, K. S. Sekerbayev, D. Pérez-Del-Rey, J. P. Martínez-Pastor, F. Palazon, P. P. Boix, T. I. Taurbayev, M. Sessolo and H. J. Bolink, Short Photoluminescence Lifetimes in Vacuum-Deposited CH3NH3PbI3 Perovskite Thin Films as a Result of Fast Diffusion of Photogenerated Charge Carriers, *Journal of Physical Chemistry Letters*, 2019, **10**, 5167–5172.

101 Y. Vaynzof, The Future of Perovskite Photovoltaics—Thermal Evaporation or Solution Processing?, *Adv Energy Mater*, DOI:10.1002/aenm.202003073.

102 J. Borchert, R. L. Milot, J. B. Patel, C. L. Davies, A. D. Wright, L. Martínez Maestro, H. J. Snaith, L. M. Herz and M. B. Johnston, Large-Area, Highly Uniform Evaporated Formamidinium Lead Triiodide Thin Films for Solar Cells, *ACS Energy Lett*, 2017, **2**, 2799–2804.

103 J. M. Ball, L. Buizza, H. C. Sansom, M. D. Farrar, M. T. Klug, J. Borchert, J. Patel, L. M. Herz, M. B. Johnston and H. J. Snaith, Dual-Source Coevaporation of Low-Bandgap $FA_{1-x}Cs_xSn_{1-y}Pb_yI_3$ Perovskites for Photovoltaics, *ACS Energy Lett*, 2019, **4**, 2748–2756.

104 C. Wehrenfennig, M. Liu, H. J. Snaith, M. B. Johnston and L. M. Herz, Charge-carrier dynamics in vapour-deposited films of the organolead halide perovskite $CH_3NH_3PbI_{3-x}Cl_x$, *Energy Environ. Sci.*, 2014, **7**, 2269–2275.

105 H. A. Dewi, J. Li, H. Wang, B. Chaudhary, N. Mathews, S. Mhaisalkar and A. Bruno, Excellent Intrinsic Long-Term Thermal Stability of Co-Evaporated $MAPbI_3$ Solar Cells at 85 °C, *Adv Funct Mater*, DOI:10.1002/adfm.202100557.

106 H. Li, M. Liu, M. Li, H. Park, N. Mathews, Y. Qi, X. Zhang, H. J. Bolink, K. Leo, M. Graetzel and C. Yi, Applications of vacuum vapor deposition for perovskite solar cells: A progress review, *iEnergy*, 2022, **1**, 434–452.

107 K. Seshan and D. Schepis, Eds., *Handbook of Thin Film Deposition*, Elsevier, Fourth Edition., 2018.

108 P. Du, L. Wang, J. Li, J. Luo, Y. Ma, J. Tang and T. Zhai, Thermal Evaporation for Halide Perovskite Optoelectronics: Fundamentals, Progress, and Outlook, *Adv Opt Mater*, DOI:10.1002/adom.202101770.

109 L. Gil-Escrig, C. Dreessen, F. Palazon, Z. Hawash, E. Moons, S. Albrecht, M. Sessolo and H. J. Bolink, Efficient Wide-Bandgap Mixed-Cation and Mixed-Halide Perovskite Solar Cells by Vacuum Deposition, *ACS Energy Lett*, 2021, **6**, 827–836.

110 A. M. Igual-Muñoz, A. Castillo, C. Dreessen, P. P. Boix and H. J. Bolink, Vacuum-Deposited Multication Tin-Lead Perovskite Solar Cells, *ACS Appl Energy Mater*, 2020, **3**, 2755–2761.

111 K. P. S. Zanoni, L. Martínez-Goyeneche, C. Dreessen, M. Sessolo and H. J. Bolink, Photovoltaic Devices Using Sublimed Methylammonium Lead Iodide Perovskites: Long-Term Reproducible Processing, *Solar RRL*, 2023, **7**, 2201073.

112 L. Zheng, D. Zhang, Y. Ma, Z. Lu, Z. Chen, S. Wang, L. Xiao and Q. Gong, Morphology control of the perovskite films for efficient solar cells, *Dalton Transactions*, 2015, **44**, 10582–10593.

113 L. Mardegan, A. Paliwal, K. P. S. Zanoni, D. Tordera and H. J. Bolink, Transparent Light-Emitting Electrochemical Cells, *Adv Opt Mater*, 2022, **10**, 2201953.

114 I. C. Kaya, K. P. S. Zanoni, F. Palazon, M. Sessolo, H. Akyildiz, S. Sonmezoglu and H. J. Bolink, Crystal Reorientation and Amorphization Induced by Stressing Efficient and Stable P–I–N Vacuum-Processed MAPbI3 Perovskite Solar Cells, *Advanced Energy and Sustainability Research*, 2021, **2**, 2000065.

115 DS-Acc-Integrating-Spheres-200702-1, https://www.avantes.com/support/downloads/accessories-2/, (accessed 1 December 2024).

116 Y. Cao, N. Wang, H. Tian, J. Guo, Y. Wei, H. Chen, Y. Miao, W. Zou, K. Pan, Y. He, H. Cao, Y. Ke, M. Xu, Y. Wang, M. Yang, K. Du, Z. Fu, D. Kong, D. Dai, Y. Jin, G. Li, H. Li, Q. Peng, J. Wang and W. Huang, Perovskite light-emitting diodes based on spontaneously formed submicrometre-scale structures, *Nature*, 2018, **562**, 249–253.

117 S.-H. Jeong, J. Park, T.-H. Han, F. Zhang, K. Zhu, J. S. Kim, M.-H. Park, M. O. Reese, S. Yoo and T.-W. Lee, Characterizing the Efficiency of Perovskite Solar Cells and Light-Emitting Diodes, *Joule*, 2020, **4**, 1206–1235.

118 W. Zhu, T. Xiao, G. Zhai, J. Yu, G. Shi, G. Chen and B. Wei, A facile method to enhance out-coupling efficiency in organic light-emitting diodes via a random-pyramids textured layer, *J Phys D Appl Phys*, 2016, **49**, 385103.

119 M. Stolterfoht, V. M. Le Corre, M. Feuerstein, P. Caprioglio, L. J. A. Koster and D. Neher, Voltage-Dependent Photoluminescence and How It Correlates with the Fill Factor and Open-Circuit Voltage in Perovskite Solar Cells, *ACS Energy Lett*, 2019, **4**, 2887–2892.

120 S. Akel, Y. Wang, G. Yan, U. Rau and T. Kirchartz, Charge Carrier Collection Losses in Lead-Halide Perovskite Solar Cells, *Adv Energy Mater*, DOI:10.1002/aenm.202401800.

121 M. Daboczi, I. Hamilton, S. Xu, J. Luke, S. Limbu, J. Lee, M. A. McLachlan, K. Lee, J. R. Durrant, I. D. Baikie and J.-S. Kim, Origin of Open-Circuit Voltage Losses in Perovskite Solar Cells Investigated by Surface Photovoltage Measurement, *ACS Appl Mater Interfaces*, 2019, **11**, 46808–46817.

122 J. Jiménez-López and E. Palomares, Interfacial recombination kinetics in aged perovskite solar cells measured using transient photovoltage techniques, *Nanoscale*, 2019, **11**, 20024–20029.

123 F. Van Van Breugel, J. N. Kutz and B. W. Brunton, Numerical Differentiation of Noisy Data: A Unifying Multi-Objective Optimization Framework, *IEEE Access*, 2020, **8**, 196865–196877.

124 F. Staub, H. Hempel, J. C. Hebig, J. Mock, U. W. Paetzold, U. Rau, T. Unold and T. Kirchartz, Beyond Bulk Lifetimes: Insights into Lead Halide Perovskite Films from Time-Resolved Photoluminescence, *Phys Rev Appl*, 2016, **6**, 1–13.

125 M. Koopmans, V. M. Le Corre and L. J. A. Koster, `SIMsalabim`: An open-source drift-diffusion simulator for semiconductor devices, *J Open Source Softw*, 2022, **7**, 3727.

126 F. Urbach, The Long-Wavelength Edge of Photographic Sensitivity and of the Electronic Absorption of Solids, *Physical Review*, 1953, **92**, 1324–1324.

127 C. Kaiser, O. J. Sandberg, N. Zarrabi, W. Li, P. Meredith and A. Armin, A universal Urbach rule for disordered organic semiconductors, *Nat Commun*, 2021, **12**, 3988.

128 U. Rau, B. Blank, T. C. M. Müller and T. Kirchartz, Efficiency Potential of Photovoltaic Materials and Devices Unveiled by Detailed-Balance Analysis, *Phys Rev Appl*, 2017, **7**, 044016.

129 J. Yao, T. Kirchartz, M. S. Vezie, M. A. Faist, W. Gong, Z. He, H. Wu, J. Troughton, T. Watson, D. Bryant and J. Nelson, Quantifying losses in open-circuit voltage in solution-processable solar cells, *Phys Rev Appl*, 2015, **4**, 1–10.

130 K. Vandewal, K. Tvingstedt, A. Gadisa, O. Inganäs and J. V. Manca, On the origin of the open-circuit voltage of polymer-fullerene solar cells, *Nat Mater*, 2009, **8**, 904–909.

131 A. D. Wright, R. L. Milot, G. E. Eperon, H. J. Snaith, M. B. Johnston and L. M. Herz, Band-Tail Recombination in Hybrid Lead Iodide Perovskite, *Adv Funct Mater*, DOI:10.1002/adfm.201700860.

132 C. M. Sutter-Fella, D. W. Miller, Q. P. Ngo, E. T. Roe, F. M. Toma, I. D. Sharp, M. C. Lonergan and A. Javey, Band Tailing and Deep Defect States in CH3NH3Pb(I1-xBrx)3Perovskites As Revealed by Sub-Bandgap Photocurrent, *ACS Energy Lett*, 2017, **2**, 709–715.

133 J. Wu, J. Luke, H. K. H. Lee, P. Shakya Tuladhar, H. Cha, S.-Y. Jang, W. C. Tsoi, M. Heeney, H. Kang, K. Lee, T. Kirchartz, J.-S. Kim and J. R. Durrant, Tail state limited photocurrent collection of thick photoactive layers in organic solar cells, *Nat Commun*, 2019, **10**, 5159.

134 S. D. Collins, C. M. Proctor, N. A. Ran and T. Nguyen, Understanding Open-Circuit Voltage Loss through the Density of States in Organic Bulk Heterojunction Solar Cells, *Adv Energy Mater*, DOI:10.1002/aenm.201501721.

135 P. Hartnagel, S. Ravishankar, B. Klingebiel, O. Thimm and T. Kirchartz, Comparing Methods of Characterizing Energetic Disorder in Organic Solar Cells, *Adv Energy Mater*, DOI:10.1002/aenm.202300329.

136 K. Vandewal, A. Gadisa, W. D. Oosterbaan, S. Bertho, F. Banishoeib, I. Van Severen, L. Lutsen, T. J. Cleij, D. Vanderzande and J. V. Manca, The Relation Between Open-Circuit

Voltage and the Onset of Photocurrent Generation by Charge-Transfer Absorption in Polymer : Fullerene Bulk Heterojunction Solar Cells, *Adv Funct Mater*, 2008, **18**, 2064–2070.

137 G. J. W. Aalbers, T. P. A. van der Pol, K. Datta, W. H. M. Remmerswaal, M. M. Wienk and R. A. J. Janssen, Effect of sub-bandgap defects on radiative and non-radiative open-circuit voltage losses in perovskite solar cells, *Nat Commun*, 2024, **15**, 1276.

138 B. T. van Gorkom, T. P. A. van der Pol, K. Datta, M. M. Wienk and R. A. J. Janssen, Revealing defective interfaces in perovskite solar cells from highly sensitive sub-bandgap photocurrent spectroscopy using optical cavities, *Nat Commun*, 2022, **13**, 349.

139 E. L. Unger, L. Kegelmann, K. Suchan, D. Sörell, L. Korte and S. Albrecht, Roadmap and roadblocks for the band gap tunability of metal halide perovskites, *J Mater Chem A Mater*, 2017, **5**, 11401–11409.

140 J.-P. Correa-Baena, M. Saliba, T. Buonassisi, M. Grätzel, A. Abate, W. Tress and A. Hagfeldt, Promises and challenges of perovskite solar cells., *Science*, 2017, **358**, 739–744.

141 L. Gil-Escrig, C. Dreessen, I. C. Kaya, B. S. Kim, F. Palazon, M. Sessolo and H. J. Bolink, Efficient vacuum-deposited perovskite solar cells with stable cubic FA1- xMAxPbI3, *ACS Energy Lett*, 2020, **5**, 3053–3061.

142 A. M. Igual-Muñoz, J. Navarro-Alapont, C. Dreessen, F. Palazon, M. Sessolo and H. J. Bolink, Room-Temperature Vacuum Deposition of CsPbI2Br Perovskite Films from Multiple Sources and Mixed Halide Precursors, *Chemistry of Materials*, 2020, **32**, 8641–8652.

143 D. Pérez-del-Rey, C. Dreessen, A. M. Igual-Muñoz, L. van den Hengel, M. C. Gélvez-Rueda, T. J. Savenije, F. C. Grozema, C. Zimmermann and H. J. Bolink, Perovskite Solar Cells: Stable under Space Conditions, *Solar RRL*, 2020, **4**, 2000447.

144 S. Zeiske, C. Kaiser, P. Meredith and A. Armin, Sensitivity of Sub-Bandgap External Quantum Efficiency Measurements of Solar Cells under Electrical and Light Bias, *ACS Photonics*, 2020, **7**, 256–264.

145 M. Grischek, P. Caprioglio, J. Zhang, F. Peña-Camargo, K. Sveinbjörnsson, F. Zu, D. Menzel, J. H. Warby, J. Li, N. Koch, E. Unger, L. Korte, D. Neher, M. Stolterfoht and S. Albrecht, Efficiency Potential and Voltage Loss of Inorganic $CsPbI_2Br$ Perovskite Solar Cells, *Solar RRL*, DOI:10.1002/solr.202200690.

146 E. T. Hoke, D. J. Slotcavage, E. R. Dohner, A. R. Bowring, H. I. Karunadasa and M. D. McGehee, Reversible photo-induced trap formation in mixed-halide hybrid perovskites for photovoltaics, *Chem Sci*, 2015, **6**, 613–617.

147 P. Caprioglio, J. A. Smith, R. D. J. Oliver, A. Dasgupta, S. Choudhary, M. D. Farrar, A. J. Ramadan, Y.-H. Lin, M. G. Christoforo, J. M. Ball, J. Diekmann, J. Thiesbrummel, K.-A. Zaininger, X. Shen, M. B. Johnston, D. Neher, M. Stolterfoht and H. J. Snaith, Open-circuit

and short-circuit loss management in wide-gap perovskite p-i-n solar cells, *Nat Commun*, 2023, **14**, 932.

148 M. H. Wolter, R. Carron, E. Avancini, B. Bissig, T. P. Weiss, S. Nishiwaki, T. Feurer, S. Buecheler, P. Jackson, W. Witte and S. Siebentritt, How band tail recombination influences the open-circuit voltage of solar cells, *Progress in Photovoltaics: Research and Applications*, 2022, **30**, 702–712.

149 N. Rodkey, K. P. S. Zanoni, M. Piot, C. Dreessen, R. Grote, P. Carroy, J. E. Sebastian Alonso, A. Paliwal, D. Muñoz and H. J. Bolink, Efficient Micrometer Thick Bifacial Perovskite Solar Cells, *Adv Energy Mater*, 2024, **14**, 202400058.

150 M. Jošt, S. Albrecht, L. Kegelmann, C. M. Wolff, F. Lang, B. Lipovšek, J. Krč, L. Korte, D. Neher, B. Rech and M. Topič, Efficient Light Management by Textured Nanoimprinted Layers for Perovskite Solar Cells, *ACS Photonics*, 2017, **4**, 1232–1239.

151 G. Martínez-Denegri, S. Colodrero, Q. Liu, J. Toudert, G. Kozyreff and J. Martorell, Ergodic Light Propagation in a Half-Cylinder Photonic Plate for Optimal Absorption in Perovskite Solar Cells, *Adv Opt Mater*, DOI:10.1002/adom.201900018.

152 M. M. Tavakoli, K. H. Tsui, Q. Zhang, J. He, Y. Yao, D. Li and Z. Fan, Highly Efficient Flexible Perovskite Solar Cells with Antireflection and Self-Cleaning Nanostructures, *ACS Nano*, 2015, **9**, 10287–10295.

153 U. W. Paetzold, W. Qiu, F. Finger, J. Poortmans and D. Cheyns, Nanophotonic front electrodes for perovskite solar cells, *Appl Phys Lett*, DOI:10.1063/1.4918751.

154 P. A. Basore, in *Conference Record of the Twenty Third IEEE Photovoltaic Specialists Conference - 1993 (Cat. No.93CH3283-9)*, IEEE, pp. 147–152.

155 D. Hinken, K. Bothe, K. Ramspeck, S. Herlufsen and R. Brendel, Determination of the effective diffusion length of silicon solar cells from photoluminescence, *J Appl Phys*, DOI:10.1063/1.3130408.

156 Q. Yang, K. Bittkau, A. Eberst, U. Rau and K. Ding, The impact of interface recombination on the external quantum efficiency of silicon solar cells, *Solar Energy Materials and Solar Cells*, 2024, **273**, 112953.

157 D. Glowienka and Y. Galagan, Light Intensity Analysis of Photovoltaic Parameters for Perovskite Solar Cells, *Advanced Materials*, DOI:10.1002/adma.202105920.

158 E. Raoult, R. Bodeux, S. Jutteau, S. Rives, A. Yaiche, A. Blaizot, D. Coutancier, J. Rousset and S. Collin, Iterative method for optical modelling of perovskite-based tandem solar cells, *Opt Express*, 2022, **30**, 9604.

159 C. Dreessen, D. Pérez-del-Rey, P. P. Boix and H. J. Bolink, Radiative and non-radiative losses by voltage-dependent in-situ photoluminescence in perovskite solar cell current-voltage curves, *J Lumin*, 2020, **222**, 117106.

160 M. Green, Accuracy of analytical expressions for solar cell fill factors, 1983, **7**, 337–340.

161 W. Tress, Perovskite Solar Cells on the Way to Their Radiative Efficiency Limit – Insights Into a Success Story of High Open-Circuit Voltage and Low Recombination, *Adv Energy Mater*, DOI:10.1002/aenm.201602358.

162 O. Almora, M. García-Batlle and G. Garcia-Belmonte, Utilization of Temperature-Sweeping Capacitive Techniques to Evaluate Band Gap Defect Densities in Photovoltaic Perovskites, *J Phys Chem Lett*, 2019, **10**, 3661–3669.

163 J. R. Harwell, T. K. Baikie, I. D. Baikie, J. L. Payne, C. Ni, J. T. S. Irvine, G. A. Turnbull and I. D. W. Samuel, Probing the energy levels of perovskite solar cells via Kelvin probe and UV ambient pressure photoemission spectroscopy, *Physical Chemistry Chemical Physics*, 2016, **18**, 19738–19745.

164 D. W. DeQuilettes, S. M. Vorpahl, S. D. Stranks, H. Nagaoka, G. E. Eperon, M. E. Ziffer, H. J. Snaith and D. S. Ginger, Impact of microstructure on local carrier lifetime in perovskite solar cells, *Science (1979)*, 2015, **348**, 683–686.

165 N. Yantara, S. Bhaumik, F. Yan, D. Sabba, H. A. Dewi, N. Mathews, P. P. Boix, H. V. Demir and S. Mhaisalkar, Inorganic Halide Perovskites for Efficient Light-Emitting Diodes, *Journal of Physical Chemistry Letters*, 2015, **6**, 4360–4364.

166 Q. Jiang, L. Zhang, H. Wang, X. Yang, J. Meng, H. Liu, Z. Yin, J. Wu, X. Zhang and J. You, Enhanced electron extraction using SnO2 for high-efficiency planar-structure HC(NH2)2 PbI3-based perovskite solar cells, *Nat Energy*, DOI:10.1038/nenergy.2016.177.

167 I. L. Braly and H. W. Hillhouse, Optoelectronic Quality and Stability of Hybrid Perovskites from MAPbI3to MAPbI2Br Using Composition Spread Libraries, *Journal of Physical Chemistry C*, 2016, **120**, 893–902.

168 I. L. Braly, D. W. DeQuilettes, L. M. Pazos-Outón, S. Burke, M. E. Ziffer, D. S. Ginger and H. W. Hillhouse, Hybrid perovskite films approaching the radiative limit with over 90% photoluminescence quantum efficiency, *Nat Photonics*, 2018, **12**, 355–361.

169 M. Stolterfoht, C. M. Wolff, J. A. Márquez, S. Zhang, C. J. Hages, D. Rothhardt, S. Albrecht, P. L. Burn, P. Meredith, T. Unold and D. Neher, Visualization and suppression of interfacial recombination for high-efficiency large-area pin perovskite solar cells - Supplementary Information, *Nat Energy*, DOI:10.1038/s41560-018-0219-8.

170 M. Stolterfoht, P. Caprioglio, C. M. Wolff, J. A. Márquez, J. Nordmann, S. Zhang, D. Rothhardt, U. Hörmann, Y. Amir, A. Redinger, L. Kegelmann, F. Zu, S. Albrecht, N. Koch, T. Kirchartz, M. Saliba, T. Unold and D. Neher, The impact of energy alignment and interfacial recombination on the internal and external open-circuit voltage of perovskite solar cells, *Energy Environ Sci*, 2019, **12**, 2778–2788.

171 G. El-Hajje, C. Momblona, L. Gil-Escrig, J. Ávila, T. Guillemot, J. F. Guillemoles, M. Sessolo, H. J. Bolink and L. Lombez, Quantification of spatial inhomogeneity in perovskite solar cells by hyperspectral luminescence imaging, *Energy Environ Sci*, 2016, **9**, 2286–2294.

172 P. Caprioglio, M. Stolterfoht, C. M. Wolff, T. Unold, B. Rech, S. Albrecht and D. Neher, On the Relation between the Open-Circuit Voltage and Quasi-Fermi Level Splitting in Efficient Perovskite Solar Cells, *Adv Energy Mater*, 2019, **1901631**, 1901631.

173 U. Rau, Reciprocity relation between photovoltaic quantum efficiency and electroluminescent emission of solar cells, *Phys Rev B Condens Matter Mater Phys*, 2007, **76**, 1–8.

174 K. Tvingstedt, O. Malinkiewicz, A. Baumann, C. Deibel, H. J. Snaith, V. Dyakonov and H. J. Bolink, Radiative efficiency of lead iodide based perovskite solar cells, *Sci Rep*, 2014, **4**, 1–7.

175 T. Du, W. Xu, M. Daboczi, J. Kim, S. Xu, C.-T. Lin, H. Kang, K. Lee, M. Heeney, J.-S. Kim, M. McLachlan and J. Durrant, P-Doping of Organic Hole Transport Layers in P-I-N Perovskite Solar Cells: Correlating Open-Circuit Voltage and Photoluminescence Quenching, *J Mater Chem A Mater*, DOI:10.1039/C9TA03896E.

176 H. Haug, Ø. Nordseth, E. V. Monakhov and E. S. Marstein, Photoluminescence imaging under applied bias for characterization of Si surface passivation layers, *Solar Energy Materials and Solar Cells*, 2012, **106**, 60–65.

177 W. Tress, B. Beyer, N. Ashari Astani, F. Gao, S. Meloni and U. Rothlisberger, Extended Intermolecular Interactions Governing Photocurrent-Voltage Relations in Ternary Organic Solar Cells, *Journal of Physical Chemistry Letters*, 2016, **7**, 3936–3944.

178 B. Dänekamp, N. Droseros, D. Tsokkou, V. Brehm, P. P. Boix, M. Sessolo, N. Banerji and H. J. Bolink, Influence of hole transport material ionization energy on the performance of perovskite solar cells, *J Mater Chem C Mater*, 2019, **7**, 523–527.

179 D. Pérez-del-Rey, L. Gil-Escrig, K. P. S. Zanoni, C. Dreessen, M. Sessolo, P. P. Boix and H. J. Bolink, Molecular Passivation of MoO3: Band Alignment and Protection of Charge Transport Layers in Vacuum-Deposited Perovskite Solar Cells, *Chemistry of Materials*, 2019, acs.chemmater.9b01396.

180 V. D'Innocenzo, G. Grancini, M. J. P. Alcocer, A. R. S. Kandada, S. D. Stranks, M. M. Lee, G. Lanzani, H. J. Snaith and A. Petrozza, Excitons versus free charges in organo-lead tri-halide perovskites., *Nat Commun*, 2014, **5**, 3586.

181 L. M. Pazos-Outón, T. P. Xiao and E. Yablonovitch, Fundamental Efficiency Limit of Lead Iodide Perovskite Solar Cells, *Journal of Physical Chemistry Letters*, 2018, **9**, 1703–1711.

182 I. L. Braly, D. W. Dequilettes, L. M. Pazos-Outón, S. Burke, M. E. Ziffer, D. S. Ginger and H. W. Hillhouse, Hybrid perovskite films approaching the radiative limit with over 90% photoluminescence quantum efficiency, *Nat Photonics*, 2018, **12**, 355–361.

183 T. Kirchartz and U. Rau, What Makes a Good Solar Cell ?, DOI:10.1002/aenm.201703385.

184 S. Zhang, S. M. Hosseini, R. Gunder, A. Petsiuk, P. Caprioglio, C. M. Wolff, S. Shoaee, P. Meredith, S. Schorr, T. Unold, P. L. Burn, D. Neher and M. Stolterfoht, The Role of Bulk

and Interface Recombination in High-Efficiency Low-Dimensional Perovskite Solar Cells, 2019, **1901090**, 1–11.

185 P. Caprioglio, F. Zu, C. M. Wolff, J. A. Márquez Prieto, M. Stolterfoht, P. Becker, N. Koch, T. Unold, B. Rech, S. Albrecht and D. Neher, High open circuit voltages in pin-type perovskite solar cells through strontium addition, *Sustain Energy Fuels*, 2019, **3**, 550–563.

186 C. M. Wolff, P. Caprioglio, M. Stolterfoht and D. Neher, Nonradiative Recombination in Perovskite Solar Cells: The Role of Interfaces, *Advanced Materials*, DOI:10.1002/adma.201902762.

187 T. Kirchartz and J. Nelson, Meaning of reaction orders in polymer:fullerene solar cells, *Phys Rev B Condens Matter Mater Phys*, 2012, **86**, 1–12.

188 T. M. Brenner, D. A. Egger, A. M. Rappe, L. Kronik, G. Hodes and D. Cahen, Are Mobilities in Hybrid Organic–Inorganic Halide Perovskites Actually "High"?, *J Phys Chem Lett*, 2015, **6**, 4754–4757.

189 I. Zarazua, G. Han, P. P. Boix, S. Mhaisalkar, F. Fabregat-Santiago, I. Mora-Seró, J. Bisquert and G. Garcia-Belmonte, Surface Recombination and Collection Efficiency in Perovskite Solar Cells from Impedance Analysis, *J Phys Chem Lett*, 2016, **7**, 5105–5113.

190 G. H. Bauer, R. Brüggemann, S. Tardon, S. Vignoli and R. Kniese, Quasi-Fermi level splitting and identification of recombination losses from room temperature luminescence in Cu(In1-xGax)Se2thin films versus optical band gap, *Thin Solid Films*, 2005, **480–481**, 410–414.

191 M. Stolterfoht, P. Caprioglio, C. M. Wolff, J. A. Márquez, J. Nordmann, S. Zhang, D. Rothhardt, U. Hörmann, Y. Amir, A. Redinger, L. Kegelmann, F. Zu, S. Albrecht, N. Koch, T. Kirchartz, M. Saliba, T. Unold and D. Neher, The impact of energy alignment and interfacial recombination on the internal and external open-circuit voltage of perovskite solar cells, *Energy Environ Sci*, 2019, **12**, 2778–2788.

192 U. Rau, V. Huhn and B. E. Pieters, Luminescence Analysis of Charge-Carrier Separation and Internal Series-Resistance Losses in Cu (In,Ga)Se2 Solar Cells, *Phys Rev Appl*, 2020, **14**, 1–13.

193 C. Dreessen, K. P. S. Zanoni, L. Gil-Escrig, N. Rodkey, J. I. Khan, F. Laquai, M. Sessolo, C. Roldán-Carmona and H. J. Bolink, When JV Curves Conceal Material Improvements: The Relevance of Photoluminescence Measurements in the Optimization of Perovskite Solar Cells, *Adv Opt Mater*, 2024, **12**, 202301019.

194 M. Stolterfoht, M. Grischek, P. Caprioglio, C. M. Wolff, E. Gutierrez-Partida, F. Peña-Camargo, D. Rothhardt, S. Zhang, M. Raoufi, J. Wolansky, M. Abdi-Jalebi, S. D. Stranks, S. Albrecht, T. Kirchartz and D. Neher, How To Quantify the Efficiency Potential of Neat Perovskite Films: Perovskite Semiconductors with an Implied Efficiency Exceeding 28%, *Advanced Materials*, 2020, **32**, 2000080.

195 W.-J. Yin, T. Shi and Y. Yan, Unique Properties of Halide Perovskites as Possible Origins of the Superior Solar Cell Performance, *Advanced Materials*, 2014, **26**, 4653–4658.

196 Z. Ni, S. Xu, H. Jiao, H. Gu, C. Fei and J. Huang, High grain boundary recombination velocity in polycrystalline metal halide perovskites, *Sci Adv*, 2022, **8**, 8345.

197 Q. An, F. Paulus, D. Becker-Koch, C. Cho, Q. Sun, A. Weu, S. Bitton, N. Tessler and Y. Vaynzof, Small grains as recombination hot spots in perovskite solar cells, *Matter*, 2021, **4**, 1683–1701.

198 A. Peter Amalathas, L. Landová, Z. Hájková, L. Horák, M. Ledinsky and J. Holovský, Controlled Growth of Large Grains in $CH_3NH_3PbI_3$ Perovskite Films Mediated by an Intermediate Liquid Phase without an Antisolvent for Efficient Solar Cells, *ACS Appl Energy Mater*, 2020, **3**, 12484–12493.

199 H. Min, D. Y. Lee, J. Kim, G. Kim, K. S. Lee, J. Kim, M. J. Paik, Y. K. Kim, K. S. Kim, M. G. Kim, T. J. Shin and S. Il Seok, Perovskite solar cells with atomically coherent interlayers on SnO2 electrodes, *Nature 2021 598:7881*, 2021, **598**, 444–450.

200 Z. Li, B. Li, X. Wu, S. A. Sheppard, S. Zhang, D. Gao, N. J. Long and Z. Zhu, Organometallic-functionalized interfaces for highly efficient inverted perovskite solar cells, *Science (1979)*, 2022, **376**, 416–420.

201 C. M. Wolff, F. Zu, A. Paulke, L. P. Toro, N. Koch and D. Neher, Reduced Interface-Mediated Recombination for High Open-Circuit Voltages in $CH_3NH_3PbI_3$ Solar Cells, *Advanced Materials*, 2017, **29**, 1700159.

202 J. P. Correa-Baena, W. Tress, K. Domanski, E. H. Anaraki, S. H. Turren-Cruz, B. Roose, P. P. Boix, M. Grätzel, M. Saliba, A. Abate and A. Hagfeldt, Identifying and suppressing interfacial recombination to achieve high open-circuit voltage in perovskite solar cells, *Energy Environ Sci*, 2017, **10**, 1207–1212.

203 S. Mahesh, J. M. Ball, R. D. J. Oliver, D. P. McMeekin, P. K. Nayak, M. B. Johnston and H. J. Snaith, Revealing the origin of voltage loss in mixed-halide perovskite solar cells, *Energy Environ Sci*, 2020, **13**, 258–267.

204 J. Haddad, B. Krogmeier, B. Klingebiel, L. Krückemeier, S. Melhem, Z. Liu, J. Hüpkes, S. Mathur and T. Kirchartz, Analyzing Interface Recombination in Lead-Halide Perovskite Solar Cells with Organic and Inorganic Hole-Transport Layers, *Adv Mater Interfaces*, 2020, **7**, 2000366.

205 J. Chen and N. G. Park, Causes and Solutions of Recombination in Perovskite Solar Cells, *Advanced Materials*, 2019, **31**, 1803019.

206 M. Stolterfoht, C. M. Wolff, J. A. Márquez, S. Zhang, C. J. Hages, D. Rothhardt, S. Albrecht, P. L. Burn, P. Meredith, T. Unold and D. Neher, Visualization and suppression of interfacial recombination for high-efficiency large-area pin perovskite solar cells, *Nat Energy*, DOI:10.1038/s41560-018-0219-8.

207 Q. Jiang, Y. Zhao, X. Zhang, X. Yang, Y. Chen, Z. Chu, Q. Ye, X. Li, Z. Yin and J. You, Surface passivation of perovskite film for efficient solar cells, *Nature Photonics 2019 13:7*, 2019, **13**, 460–466.

208 J. Li, H. Wang, X. Y. Chin, H. A. Dewi, K. Vergeer, T. W. Goh, J. W. M. Lim, J. H. Lew, K. P. Loh, C. Soci, T. C. Sum, H. J. Bolink, N. Mathews, S. Mhaisalkar and A. Bruno, Highly Efficient Thermally Co-evaporated Perovskite Solar Cells and Mini-modules, *Joule*, 2020, **4**, 1035–1053.

209 J. Ávila, C. Momblona, P. P. Boix, M. Sessolo and H. J. Bolink, Vapor-Deposited Perovskites: The Route to High-Performance Solar Cell Production?, *Joule*, 2017, **1**, 431–442.

210 M. Liu, M. B. Johnston and H. J. Snaith, Efficient planar heterojunction perovskite solar cells by vapour deposition, *Nature*, 2013, **501**, 395–398.

211 I. Susic, L. Gil-Escrig, F. Palazon, M. Sessolo and H. J. Bolink, Quadruple-Cation Wide-Bandgap Perovskite Solar Cells with Enhanced Thermal Stability Enabled by Vacuum Deposition, *ACS Energy Lett*, 2022, **7**, 1355–1363.

212 B.-S. Kim, L. Gil-Escrig, M. Sessolo and H. J. Bolink, Deposition Kinetics and Compositional Control of Vacuum-Processed $CH_3NH_3PbI_3$ Perovskite, *J Phys Chem Lett*, 2020, **11**, 6852–6859.

213 E. Pérez-Gutiérrez, M. J. Percino, P. Santos, M. Cerón, P. Ceballos, D. M. Montoya, O. Barbosa-García and S. Thamotharan, Compositional study of mixed halide perovskite films CH3NH3Pb(I1-Br )3 and CH3NH3Pb(I1-Cl )3 prepared by close space sublimation, *Mater Today Commun*, 2020, **25**, 101384.

214 J. Zhou, L. Tan, Y. Liu, H. Li, X. Liu, M. Li, S. Wang, Y. Zhang, C. Jiang, R. Hua, W. Tress, S. Meloni and C. Yi, Highly efficient and stable perovskite solar cells via a multifunctional hole transporting material, *Joule*, 2024, **8**, 1691–1706.

215 T. J. Jacobsson, A. Hultqvist, A. García-Fernández, A. Anand, A. Al-Ashouri, A. Hagfeldt, A. Crovetto, A. Abate, A. G. Ricciardulli, A. Vijayan, A. Kulkarni, A. Y. Anderson, B. P. Darwich, B. Yang, B. L. Coles, C. A. R. Perini, C. Rehermann, D. Ramirez, D. Fairen-Jimenez, D. Di Girolamo, D. Jia, E. Avila, E. J. Juarez-Perez, F. Baumann, F. Mathies, G. S. A. González, G. Boschloo, G. Nasti, G. Paramasivam, G. Martínez-Denegri, H. Näsström, H. Michaels, H. Köbler, H. Wu, I. Benesperi, M. I. Dar, I. Bayrak Pehlivan, I. E. Gould, J. N. Vagott, J. Dagar, J. Kettle, J. Yang, J. Li, J. A. Smith, J. Pascual, J. J. Jerónimo-Rendón, J. F. Montoya, J. P. Correa-Baena, J. Qiu, J. Wang, K. Sveinbjörnsson, K. Hirselandt, K. Dey, K. Frohna, L. Mathies, L. A. Castriotta, M. H. Aldamasy, M. Vasquez-Montoya, M. A. Ruiz-Preciado, M. A. Flatken, M. V. Khenkin, M. Grischek, M. Kedia, M. Saliba, M. Anaya, M. Veldhoen, N. Arora, O. Shargaieva, O. Maus, O. S. Game, O. Yudilevich, P. Fassl, Q. Zhou, R. Betancur, R. Munir, R. Patidar, S. D. Stranks, S. Alam, S. Kar, T. Unold, T. Abzieher, T. Edvinsson, T. W. David, U. W. Paetzold, W. Zia, W. Fu, W. Zuo, V. R. F.

Schröder, W. Tress, X. Zhang, Y. H. Chiang, Z. Iqbal, Z. Xie and E. Unger, An open-access database and analysis tool for perovskite solar cells based on the FAIR data principles, *Nature Energy 2021 7:1*, 2021, **7**, 107–115.

216 F. U. Kosasih, E. Erdenebileg, N. Mathews, S. G. Mhaisalkar and A. Bruno, Thermal evaporation and hybrid deposition of perovskite solar cells and mini-modules, *Joule*, 2022, **6**, 2692–2734.

217 I. Levine, S. Gupta, A. Bera, D. Ceratti, G. Hodes, D. Cahen, D. Guo, T. J. Savenije, J. Ávila, H. J. Bolink, O. Millo, D. Azulay and I. Balberg, Can we use time-resolved measurements to get steady-state transport data for halide perovskites?, *J Appl Phys*, 2018, **124**, 103103.

218 D. Pérez-Del-Rey, L. Gil-Escrig, K. P. S. Zanoni, C. Dreessen, M. Sessolo, P. P. Boix and H. J. Bolink, Molecular Passivation of MoO3: Band Alignment and Protection of Charge Transport Layers in Vacuum-Deposited Perovskite Solar Cells, *Chemistry of Materials*, 2019, **31**, 6945–6949.

219 U. Rau, Reciprocity relation between photovoltaic quantum efficiency and electroluminescent emission of solar cells, *Phys Rev B Condens Matter Mater Phys*, 2007, **76**, 085303.

220 S. Jeong, S. Seo, H. Yang, H. Park, S. Shin, H. Ahn, D. Lee, J. H. Park, N. Park and H. Shin, Cyclohexylammonium-Based 2D/3D Perovskite Heterojunction with Funnel-Like Energy Band Alignment for Efficient Solar Cells (23.91%), *Adv Energy Mater*, DOI:10.1002/aenm.202102236.

221 L. Zhao, N. Rolston, K. M. Lee, X. Zhao, M. A. Reyes-Martinez, N. L. Tran, Y. Yeh, N. Yao, G. D. Scholes, Y. Loo, A. Selloni, R. H. Dauskardt and B. P. Rand, Influence of Bulky Organo-Ammonium Halide Additive Choice on the Flexibility and Efficiency of Perovskite Light-Emitting Devices, *Adv Funct Mater*, 2018, **28**, 1802060.

222 W. Sun, J. Zou, X. Wang, S. Wang, Y. Du, F. Cao, L. Zhang, J. Wu and P. Gao, Enhanced photovoltage and stability of perovskite photovoltaics enabled by a cyclohexylmethylammonium iodide-based 2D perovskite passivation layer, *Nanoscale*, 2021, **13**, 14915–14924.

223 A. Q. Alanazi, M. H. Almalki, A. Mishra, D. J. Kubicki, Z. Wang, L. Merten, F. T. Eickemeyer, H. Zhang, D. Ren, A. Y. Alyamani, H. Albrithen, A. Albadri, M. H. Alotaibi, A. Hinderhofer, S. M. Zakeeruddin, F. Schreiber, A. Hagfeldt, L. Emsley, J. V. Milić and M. Graetzel, Benzylammonium-Mediated Formamidinium Lead Iodide Perovskite Phase Stabilization for Photovoltaics, *Adv Funct Mater*, 2021, **31**, 2101163.

224 A. S. Yerramilli, Y. Chen and T. L. Alford, Passivation of triple cation perovskites using guanidinium iodide in inverted solar cells for improved open-circuit voltage and stability, *Sustain Energy Fuels*, 2021, **5**, 2486–2493.

225 C. Ma, D. Shen, B. Huang, X. Li, W.-C. Chen, M.-F. Lo, P. Wang, M. Hon-Wah Lam, Y. Lu, B. Ma and C.-S. Lee, High performance low-dimensional perovskite solar cells based on a one dimensional lead iodide perovskite, *J Mater Chem A Mater*, 2019, **7**, 8811–8817.

226 C. Zhang, X. Ren, X. He, Y. Zhang, Y. Liu, J. Feng, F. Gao, N. Yuan, J. Ding and S. (Frank) Liu, Post-treatment by an ionic tetrabutylammonium hexafluorophosphate for improved efficiency and stability of perovskite solar cells, *Journal of Energy Chemistry*, 2022, **64**, 8–15.

227 P. Ferdowsi, E. Ochoa-Martinez, S. S. Alonso, U. Steiner and M. Saliba, Ultrathin polymeric films for interfacial passivation in wide band-gap perovskite solar cells, *Scientific Reports 2020 10:1*, 2020, **10**, 1–10.

228 A. A. M. Brown, T. J. N. Hooper, S. A. Veldhuis, X. Y. Chin, A. Bruno, P. Vashishtha, J. N. Tey, L. Jiang, B. Damodaran, S. H. Pu, S. G. Mhaisalkar and N. Mathews, Self-assembly of a robust hydrogen-bonded octylphosphonate network on cesium lead bromide perovskite nanocrystals for light-emitting diodes, *Nanoscale*, 2019, **11**, 12370–12380.

229 S. G. Motti, D. Meggiolaro, A. J. Barker, E. Mosconi, C. A. R. Perini, J. M. Ball, M. Gandini, M. Kim, F. De Angelis and A. Petrozza, Controlling competing photochemical reactions stabilizes perovskite solar cells, *Nature Photonics 2019 13:8*, 2019, **13**, 532–539.

230 S. Jariwala, S. Burke, S. Dunfield, R. C. Shallcross, M. Taddei, J. Wang, G. E. Eperon, N. R. Armstrong, J. J. Berry and D. S. Ginger, Reducing Surface Recombination Velocity of Methylammonium-Free Mixed-Cation Mixed-Halide Perovskites via Surface Passivation, *Chemistry of Materials*, 2021, **33**, 5035–5044.

231 R. Zhao, K. Zhang, J. Zhu, S. Xiao, W. Xiong, J. Wang, T. Liu, G. Xing, K. Wang, S. Yang and X. Wang, Surface passivation of organometal halide perovskites by atomic layer deposition: an investigation of the mechanism of efficient inverted planar solar cells, *Nanoscale Adv*, 2021, **3**, 2305–2315.

232 T. Kirchartz, J. A. Márquez, M. Stolterfoht and T. Unold, Photoluminescence-Based Characterization of Halide Perovskites for Photovoltaics, *Adv Energy Mater*, 2020, **10**, 1904134.

233 T. W. Crothers, R. L. Milot, J. B. Patel, E. S. Parrott, J. Schlipf, P. Müller-Buschbaum, M. B. Johnston and L. M. Herz, Photon Reabsorption Masks Intrinsic Bimolecular Charge-Carrier Recombination in CH3NH3PbI3 Perovskite, *Nano Lett*, 2017, **17**, 5782–5789.

234 X. Zhang, J.-X. Shen, W. Wang and C. G. Van de Walle, First-Principles Analysis of Radiative Recombination in Lead-Halide Perovskites, *ACS Energy Lett*, 2018, **3**, 2329–2334.

235 J. M. Richter, M. Abdi-Jalebi, A. Sadhanala, M. Tabachnyk, J. P. H. Rivett, L. M. Pazos-Outón, K. C. Gödel, M. Price, F. Deschler and R. H. Friend, Enhancing photoluminescence yields in lead halide perovskites by photon recycling and light out-coupling, *Nat Commun*, 2016, **7**, 13941.

236 T. S. Sherkar, C. Momblona, L. Gil-Escrig, J. Ávila, M. Sessolo, H. J. Bolink and L. J. A. Koster, Recombination in Perovskite Solar Cells: Significance of Grain Boundaries, Interface Traps, and Defect Ions, *ACS Energy Lett*, 2017, **2**, 1214–1222.

237 F. Brivio, K. T. Butler, A. Walsh and M. Van Schilfgaarde, Relativistic quasiparticle self-consistent electronic structure of hybrid halide perovskite photovoltaic absorbers, *Phys Rev B Condens Matter Mater Phys*, 2014, **89**, 1–6.

238 K. Odysseas Kosmatos, L. Theofylaktos, E. Giannakaki, D. Deligiannis, M. Konstantakou and T. Stergiopoulos, Methylammonium Chloride: A Key Additive for Highly Efficient, Stable, and Up-Scalable Perovskite Solar Cells, *Energy & Environmental Materials*, 2019, **2**, 79–92.

# 9 Index of Figures

# 10 Index of Tables

# 11 Abbreviations and Symbols

| Symbol | Abbreviation | Full name |
|---|---|---|
| $A$ | | absorptance |
| $b$ | | energy-independent factor for EQE calculation |
| $c$ | | speed of light |
| $C_n$ | | electron-electron-hole Auger coefficient |
| $C_p$ | | electron-hole-hole Auger coefficient |
| $c_{PL}$ | | calibration spectra |
| $d$ | | layer thickness |
| $D$ | | diffusion coefficient |
| $D_P$ | | degree of the polymerisation of a polymer |
| $E$ | | energy |
| $E_C$ | | conduction band energy |
| $E_F$ | | Fermi level energy |
| $E_{F,n}$ | | electron quasi-Fermi level in the conduction band |
| $E_{F,p}$ | | hole quasi-Fermi level in the valence band |
| $E_g$ | | bandgap |
| $E_{ph}$ | | photon energy |
| $E_T$ | | trap energy |
| $E_U$ | | Urbach energy |
| $E_V$ | | valence band energy |
| $E_{vac}$ | | vacuum level energy |
| $f$ | | focal length |
| $f_c$ | | photocurrent collection efficiency |
| $FF$ | | fill factor |
| $f_{FD}$ | | Fermi-Dirac occupation statistics |
| $FF_{SQ}$ | | fill factor in SQ limit |
| $G$ | | charge carrier generation rate |

| | |
|---|---|
| $h$ | Planck constant |
| $I$ | light intensity |
| $I_0$ | incoming light intensity |
| $J$ | current density |
| $J_0$ | saturation current density |
| $J_{0,\text{non-rad}}$ | non-radiative saturation current density |
| $J_{0,\text{rad}}$ | radiative saturation current density |
| $J_{0,\text{SQ}}$ | saturation current density in SQ limit |
| $J_{\text{extr}}$ | electrically extracted current density |
| $J_{\text{gen}}$ | photogenerated current density |
| $J_{\text{mpp}}$ | current density at MPP |
| $J_{\text{non-rad}}$ | non-radiative current density |
| $J_{\text{rad}}$ | radiative current density |
| $J_{\text{sc}}$ | short-circuit current density |
| $J_{\text{sc,SQ}}$ | short-circuit current density in SQ limit |
| $k$ | Boltzmann constant |
| $k_{\text{rad}}$ | radiative recombination coefficient |
| $n$ | electron concentration |
| $n_0$ | equilibrium electron concentration |
| $n_1$ | electron detrapping parameter |
| $N_{\text{C}}$ | effective density of states in the conduction band |
| $n_{\text{i}}$ | intrinsic charge carrier concentration |
| $n_{\text{id}}$ | ideality factor |
| $n_{\text{r}}$ | refractive index |
| $N_{\text{T}}$ | trap density |
| $N_{\text{V}}$ | effective density of states in the valence band |
| $p$ | hole concentration |
| $p_0$ | equilibrium hole concentration |
| $p_1$ | hole detrapping parameter |
| $p_{\text{a}}$ | parasitic absorption probability |
| $P_{\text{d}}$ | power density |
| $P_{\text{d,max}}$ | power density at MPP |
| $p_{\text{e}}$ | photon escape probability |
| $q$ | elementary charge |

| | | |
|---|---|---|
| $Q_e^{PL}$ | PLQY | external PL quantum yield |
| $Q_e^{PL}{}_{device}$ | | PLQY of the device |
| $Q_e^{PL}{}_{film}$ | | PLQY of the free standing perovskite film |
| $Q_E^{PV}$ | EQE | photovoltaic external quantum efficiency |
| $Q_I^{PV}$ | IQE | photovoltaic internal quantum efficiency |
| $R$ | | reflectance |
| $R^*$ | | exciton binding energy |
| $r_A$ | | ionic radius of ion A |
| $R_{auger}$ | | Auger recombination rate |
| $r_B$ | | ionic radius of ion B |
| $R_{rad}$ | | radiative recombination rate |
| $R_s$ | | series resistance |
| $R_{sh}$ | | shunt resistance |
| $R_{SRH}$ | | SRH recombination rate |
| $R_{surface}$ | | surface recombination rate |
| $R_{tot}$ | | total recombination rate |
| $r_X$ | | ionic radius of ion X |
| $S$ | | surface recombination velocity |
| $S_n$ | | electron surface recombination velocity |
| $S_p$ | | hole surface recombination velocity |
| $T$ | | temperature |
| $t$ | | time |
| $t_{int}$ | | integration time |
| $t_{tol}$ | | tolerance factor |
| $V$ | | voltage |
| $V_{mpp}$ | | voltage at MPP |
| $V_{oc}$ | | open-circuit voltage |
| $V_{oc,rad}$ | | radiative limit of the OC voltage |
| $V_{oc,SQ}$ | | open-circuit voltage in SQ limit |
| $x$ | | placeholder for one of the four *JV* parameters |
| $\alpha$ | | absorption coefficient |
| $\beta_n$ | | electron capture coefficient |
| $\beta_p$ | | hole capture coefficient |
| $\Delta E_F$ | QFLS | quasi-Fermi level splitting |

| | | |
|---|---|---|
| $\Delta n$ | | excess electron carrier concentration |
| $\Delta p$ | | excess hole carrier concentration |
| $\Delta V_{oc,non\text{-}rad}$ | | non-radiative OC voltage losses |
| $\delta x$ | | infinitesimal thickness |
| $\Delta E_{F,device}$ | | QFLS of the device |
| $\Delta E_{F,film}$ | | QFLS of the free standing perovskite film |
| $\Delta V_{oc,rad}$ | | radiative OC voltage losses |
| $\Delta V_{oc,sc}$ | | OC voltage losses due to a reduced SC current density |
| $\lambda$ | | wavelength |
| $\mu_n$ | | electron mobility |
| $\mu_p$ | | hole mobility |
| $\eta$ | PCE | power conversion efficiency |
| $\eta_{SQ}$ | | power conversion efficiency in SQ limit |
| $\tau_{bulk}$ | | bulk charge carrier lifetime |
| $\tau_{diff}$ | | differential decay time |
| $\tau_{eff}$ | | effective charge carrier lifetime |
| $\tau_{rad}$ | | radiative lifetime |
| $\tau_s$ | | surface lifetime |
| $\tau_{SRH}$ | | SRH lifetime |
| $\tau_{SRH,n}$ | | electron SRH lifetime |
| $\tau_{SRH,p}$ | | hole SRH lifetime |
| $\tau_{tot}$ | | total charge carrier lifetime |
| $\upsilon_{oc}$ | | normalised open-circuit voltage |
| $\phi_{abs}$ | | absorbed photon flux |
| $\phi_{BB}$ | | black-body radiation |
| $\phi_{oc}$ | | PL photon flux at OC |
| $\phi_{PL}$ | | PL photon flux |
| $\phi_{PL}^{E}$ | | spectral PL photon flux |
| $\phi_{sc}$ | | PL photon flux at SC |
| $\phi_{spec}$ | | counts of spectrometer |
| $\phi_{sun}$ | | AM1.5G sun spectrum |
| | ALD | atomic layer deposition |
| | BCP | bathocuproine |
| | CsPbIBr | $CsPbI_2Br$ |

| | |
|---|---|
| CTL | charge transport layer |
| EL | electroluminescence |
| ETL | electron transport layer |
| FA | formamidinium |
| FACsPbIBr | $FA_xCs_{1-x}Pb(I_yBr_{1-y})_3$ |
| FAMAPI | $FA_xMA_{1-x}PbI_3$ |
| FTO | fluorine-doped tin oxide |
| FTPS | Fourier-transform photocurrent spectroscopy |
| GUA | guanidinium |
| GUI | graphical user interface |
| HTL | hole transport layer |
| ITO | indium tin oxide |
| *JV* | current-voltage |
| LED | light-emitting diode |
| MA | methylammonium |
| MAPI | $MAPbI_3$ |
| MPP | maximum power point |
| OC | open-circuit |
| PDS | photothermal deflection spectroscopy |
| PL | photoluminescence |
| PLD | pulsed laser deposition |
| PV | photovoltaic |
| QCM | quartz crystal microbalance |
| SC | short-circuit |
| SEM | scanning electron microscopy |
| SQ | Shockley-Queisser |
| SRH | Shockley-Read-Hall |
| Suns-$V_{oc}$ | light intensity-dependent OC voltage measurements |
| Suns-$\Delta E_{F,film}$ | light intensity-dependent QFLS measurements of the free standing perovskite film |
| TaTm | (N,N,N′,N′-Tetra([1,1′-biphenyl]−4-yl) [1,1′:4′,1″-terphenyl]−4,4″-diamine |
| TCO | transparent conductive oxide |
| TPBi | 2,2′,2″-(1,3,5-benzinetriyl)- |

| | |
|---|---|
| | tris(1-phenyl-1-*H*-benzimidazole |
| TRPL | time-resolved PL |
| UV-Vis | ultraviolet-visible |
| XRD | X-ray diffraction |

# 12 List of Publications

1 A. Babaei, **C. Dreessen**, M. Sessolo and H. J. Bolink, High voltage vacuum-processed perovskite solar cells with organic semiconducting interlayers, *RSC Adv*, 2020, **10**, 6640–6646.

2 P. Sebastia-Luna, M. C. Gélvez-Rueda, **C. Dreessen**, M. Sessolo, F. C. Grozema, F. Palazon and H. J. Bolink, Potential and limitations of CsBi3I10as a photovoltaic material, *J Mater Chem A Mater*, 2020, **8**, 15670–15674.

3 W. Soltanpoor, **C. Dreessen**, M. C. Sahiner, I. Susic, A. Z. Afshord, V. S. Chirvony, P. P. Boix, G. Gunbas, S. Yerci and H. J. Bolink, Hybrid Vapor-Solution Sequentially Deposited Mixed-Halide Perovskite Solar Cells, *ACS Appl Energy Mater*, 2020, **3**, 8257–8265.

4 **C. Dreessen**, D. Pérez-del-Rey, P. P. Boix and H. J. Bolink, Radiative and non-radiative losses by voltage-dependent in-situ photoluminescence in perovskite solar cell current-voltage curves, *J Lumin*, 2020, **222**, 117106.

5 L. Gil-Escrig, **C. Dreessen**, I. C. Kaya, B. S. Kim, F. Palazon, M. Sessolo and H. J. Bolink, Efficient vacuum-deposited perovskite solar cells with stable cubic FA1- xMAxPbI3, *ACS Energy Lett*, 2020, **5**, 3053–3061.

6 A. M. Igual-Muñoz, J. Navarro-Alapont, **C. Dreessen**, F. Palazon, M. Sessolo and H. J. Bolink, Room-Temperature Vacuum Deposition of CsPbI2Br Perovskite Films from Multiple Sources and Mixed Halide Precursors, *Chemistry of Materials*, 2020, **32**, 8641–8652.

7 D. Pérez-del-Rey, **C. Dreessen**, A. M. Igual-Muñoz, L. van den Hengel, M. C. Gélvez-Rueda, T. J. Savenije, F. C. Grozema, C. Zimmermann and H. J. Bolink, Perovskite Solar Cells: Stable under Space Conditions, *Solar RRL*, 2020, **4**, 2000447.

8 L. Gil-Escrig, **C. Dreessen**, F. Palazon, Z. Hawash, E. Moons, S. Albrecht, M. Sessolo and H. J. Bolink, Efficient Wide-Bandgap Mixed-Cation and Mixed-Halide Perovskite Solar Cells by Vacuum Deposition, *ACS Energy Lett*, 2021, **6**, 827–836.

9 L. Mardegan, **C. Dreessen**, M. Sessolo, D. Tordera and H. J. Bolink, Stable Light-Emitting Electrochemical Cells Using Hyperbranched Polymer Electrolyte, *Adv Funct Mater*, 2021, **31**, 2104249.

10 A. Paliwal, **C. Dreessen**, K. P. S. Zanoni, B. Dänekamp, B.-S. Kim, M. Sessolo, K. Vandewal and H. J. Bolink, Vacuum-Deposited Microcavity Perovskite Photovoltaic Devices, *ACS Photonics*, 2021, **8**, 2067–2073.

11 B.-S. Kim, D. Pérez-del-Rey, A. Paliwal, **C. Dreessen**, M. Sessolo and H. J. Bolink, Simple approach for an electron extraction layer in an all-vacuum processed n-i-p perovskite solar cell, *Energy Advances*, 2022, **1**, 252–257.

12 I. Susic, A. Kama, L. Gil-Escrig, **C. Dreessen**, F. Palazon, D. Cahen, M. Sessolo and H. J. Bolink, Combinatorial Vacuum-Deposition of Wide Bandgap Perovskite Films and Solar Cells, *Adv Mater Interfaces*, 2023, **10**, 202202271.

13 K. P. S. Zanoni, L. Martínez-Goyeneche, **C. Dreessen**, M. Sessolo and H. J. Bolink, Photovoltaic Devices Using Sublimed Methylammonium Lead Iodide Perovskites: Long-Term Reproducible Processing, *Solar RRL*, 2023, **7**, 2201073.

14 K. P. S. Zanoni, D. Pérez-del-Rey, **C. Dreessen**, N. Rodkey, M. Sessolo, W. Soltanpoor, M. Morales-Masis and H. J. Bolink, Tin(IV) Oxide Electron Transport Layer via Industrial-Scale Pulsed Laser Deposition for Planar Perovskite Solar Cells, *ACS Appl Mater Interfaces*, 2023, **15**, 32621–32628.

15 **C. Dreessen**, K. P. S. Zanoni, L. Gil-Escrig, N. Rodkey, J. I. Khan, F. Laquai, M. Sessolo, C. Roldán-Carmona and H. J. Bolink, When JV Curves Conceal Material Improvements: The Relevance of Photoluminescence Measurements in the Optimization of Perovskite Solar Cells, *Adv Opt Mater*, 2024, **12**, 202301019.

16 N. Rodkey, K. P. S. Zanoni, M. Piot, **C. Dreessen**, R. Grote, P. Carroy, J. E. Sebastian Alonso, A. Paliwal, D. Muñoz and H. J. Bolink, Efficient Micrometer Thick Bifacial Perovskite Solar Cells, *Adv Energy Mater*, 2024, **14**, 202400